2007

Boundary element method in anisotropic media with grain sliding and dislocation dynamics

Dun Leng
Iowa State University

Boundary element method in anisotropic media with grain sliding and dislocation dynamics

by

Dun Leng

A dissertation submitted to the graduate faculty

in partial fulfillment of the requirements for the degree of

DOCTOR OF PHILOSOPHY

Major: Engineering Mechanics

Program of Study Committee:
Ambar K. Mitra, Major Professor
S.Bulent Biner
Thomas J. Rudolphi
Abhijit Chandra
Srinivas Aluru

Iowa State University

Ames, Iowa

2007

TABLE OF CONTENTS

ACKNOWLEDGMENTS

I would like to express my sincere gratitude to my major professor, Dr Ambar Mitra, for his guidance, patience and support for my Ph.D study. It is his enthusiasm, excellent teaching and deep knowledge that attracted me into the area of boundary element method. It is my great pleasure to learn from him and do research with him for the past several years.

Also I want to thank Iowa State University and the Department of Aerospace Engineering for the financial support and the opportunity given to me to teach during my Ph.D study.

Most importantly, I want to thank my family, my wife Yibin Xu, and my daughter Angelina Leng. They are always there to support me and they are my true motivation to finish this work.

ABSTRACT

Boundary element method (BEM) is an effective numerical technique to solve complex engineering problems. The fundamental solutions for both isotropic and anisotropic boundary element method are studied as the basis to develop elastostatic boundary integral equations.

The numerical implementation of BEM is described in detail. Multi-zone BEM is introduced to calculate polycrystal grains structure. The connectivity between grains is modeled with a stiffness spring system. The sliding effect at grain boundaries is simulated by a non linear sliding model.

After anisotropy and grain sliding are implemented with BEM, the information on the grain boundaries can be calculated effectively. Inside the grains, the dislocation theory is discussed. For multiple dislocations, two calculation methods are introduced: discrete dislocation method and dislocation density tensor method. For the dislocation density tensor method, the domain integrals are transformed into boundary integral to save computing time and to make the computing compatible with the BEM formulation. To control the total error and save time, a combination of discrete and density tensor methods is developed to calculate the stress field due to multiple dislocations. The new mixed method reduce the run time from the order $O(n^2)$ to $O(n)$ and keep the error within 2%.

The dislocation dynamics is studied to explore the effect of grain size on yielding and the results match the Hall-Petch law. The results with grain sliding and anisotropy are also shown and analyzed.

CHAPTER ONE: INTRODUCTION

Boundary element method (BEM) also known as the Boundary Integral Equation (BIE) method is a technique for engineering analysis. The fundamentals of BEM can be traced back to classical mathematical formulations by Fredholm[1] and Mikhilin[2] in potential theory and Betti[3], Somigliana[4] and Kupradze[5] for elasticity applications. Jaswon[6], Hess and Smith[7], Massonnet[8], Rizzo[9] and Cruse[10] made further developments in the formulation of the boundary integral equations. The early work of Lachat[11], Lachat and Watson[12] made BEM an effective numerical technique. They demonstrated that problems with complex configurations can be solved efficiently by using isoparametric formulation. Around the same time, the first international symposium[13] attracted the attentions of the engineering community and made BEM the official name for this numerical method.

The advantage of BEM can be attributed to the reduction in the dimensionality of the problem; for two dimensional problems, only the one dimensional line-boundary of the domain needs to be discretized into elements and for three dimensional problems only the two dimensional surface of the problem need to be discretized. This reduction in dimensionality in modeling gives BEM a huge advantage compared to finite-element method (FEM) and other domain type analysis techniques. Furthermore, as the quantities such as displacements and tractions are determined only on the discretized boundary, a much smaller system of equations is obtained. Although the matrices in BEM are fully populated, the FEM matrices are sparse.

Another important feature of BEM is that it provides a continuous modeling for the interior calculation and lead to a high resolution of interior stress and displacements. The quantities at internal points are calculated as a post processing after the boundary unknowns are calculated. The density, distribution and location of the internal points have no bearing on the boundary mesh.

The application of BEM requires the determination of the so-called "fundamental solutions'. A fundamental solution is the solution of the governing equations due to unit forces. Lauricella[14], Fredholm[15], Sokolnikoff[16], Banerjee and Butterfield[17] showed the determination of the fundamental solution for isotropic media. The anisotropic fundamental solutions are solved thru the works of Lekhnitskii[18], Tomlin and Butterfield[19], Snyder and Cruse[20]. The numerical implementation of the two dimensional BEM is described in Chapters two and three.

The application of BEM in this thesis is mainly focused on crystal structured grains. Since each grain has its own elastic property, multi-zone BEM is introduced to analyze the multi-grain problem. Although the modeling of multi zone BME looks very similar to FEM, it still has its advantage by not having interior meshing of the grains.

To simulate the interaction between grains, two dimensional springs are modeled on all grain interfaces. The spring stiffness on normal and shear direction can be prescribed independently. For continuous grain structures, normal and shear spring stiffnesses are assigned a relatively large magnitude compared with the elastic property. In that situation, the grains do not separate due to the high spring stiffness. For viscous grain boundaries, the grain sliding models are studied by Crossman and Ashby[21], Ghahremani[22, 23], Tvergaard[24, 25], Fotiu, Heuer and Ziegler[26], and Biner[27].

The shear spring stiffness are set to zero in the multi zone BEM model and the relaxation process is modeled with a non linear relationship between the grain boundary shear tractions and the shear displacements.

After anisotropy and grain sliding are modeled with BEM, the dislocation dynamics[28-34] is included and modeled in the BEM. Dislocation plays an important role in plastic deformation in crystalline solids. The generation and motion of dislocations and the interaction among dislocations are the key factors in dislocation dynamics. For the study of these factors, one needs the interior stress and dislocation stress field. BEM is the perfect tool for the interior stress calculation. Mura[28] gave the details of dislocation stress field calculations and Eshelby[35] showed how to incorporate that field with the elastic finite body. The core of the dislocation stress field calculation is a Green function that is very similar to the BEM fundamental solutions. This similarity makes the dislocation stress calculation highly compatible with BEM formulation.

For multiple dislocations, the discrete method by Amodeo and Ghoneim[36, 37], Kubin[38], Van der Giessen and Needleman[39], Zbib[40] and Schwarz[41] is to calculate the effect of each dislocation and use superposition for their combined effect. As there are thousands or even millions of dislocations inside crystal grains, this method is time-consuming. To accelerate this calculation, a new method is developed to homogenize the dislocations inside some specific zones. The homogenization process employs the dislocation density tensor method[42-47] to calculate the stress field of all the dislocations inside that zone. The definition of those zones is carefully designed in order to control the error caused by the homogenization within a tolerance level.

The dislocation density method required domain integration for that zone. To save runtime and more important, to be compatible with BEM, that domain integral can be transferred into boundary only integral (by Gao [48-51]) because of the special structure associated with the Green function. With this transformation, the dislocation calculation with BEM is truly a boundary only method. This newly developed method can reduce the runtime by the discrete dislocation method from $O(n^2)$ to $O(n)$.

After the stress field is calculated, dislocation dynamics[39, 47, 52-55] can be performed with the generation and motion of dislocations. The slip lines, periodic boundaries, grain sliding, and anisotropy are modeled into the dislocation dynamics. For different grain sizes, "Hall-Petch law"[56, 57] is compared with the isotropic non sliding BEM numerical results. Hall and Petch correlated the yielding strength of the grain with the inverse square root of the size of the grain. In this thesis, the slope between $\log(\tau)$ and $\log(1/d)$ where τ is the yielding strength and d is the size of the grain are plotted, and the sloped number are calculated. The slop number for isotropic non sliding grains is very close to 0.5 and consistent with the Hall-Petch law.

Next, the effect of grain sliding and anisotropy are showed on the yielding stress curves. The grain sliding lowers the curve with reduction in grain size. Anisotropy either raises the slope when the anisotropy ratio is smaller than one and lowers the slope when the anisotropy ratio is larger than one. The reasons behind such variation are explained in Chapter four.

References:

1. Fredholm, I., *Sur une classe d'equations fonctionelles.* Acta mathematica, 1903. **27**: p. 365-390.
2. Mikhlin, S.G., *Integral equations*. 1957: Pergamon Press New York.
3. Betti, E., *Teori dell elasticita.* II Nuovo Cimento, 1872: p. 7-10.
4. Somigliana, C., *Sopra l'equilibrio di un corpo elastico isotropo.* II Nuovo Cimento, 1886. **20**: p. 181-185.
5. Kupradze, V.D., *Potential methods in the theory of elasticity. Translated from the Russian by H. Gutfreund. Translation edited by I.* 1965, Israel Program for Scientific Translations, Jerusalem.
6. Jaswon, M.A., *Integral Equation Methods in Potential Theory. I.* 1963, JSTOR. p. 23-32.
7. Hess, J.L. and A.M.O. Smith, *Calculation of potential flow about arbitrary*. 1967. p. 1-138.
8. Massonnet, C.E., *Numerical use of integral procedures*, in *Stress Analysis*. 1965, Wiley: London. p. 198-235.
9. Rizzo, F.J., *An integral equation approach to boundary value problems of classical elastostatics, Q.* Quarterly Journal of Applied mathematics, 1967. **25**: p. 83-95.
10. Cruse, T., *Numerical solutions in three-dimensional elastostatics.* International Journal of Solids and Structures, 1969. **5**: p. 1259-1274.
11. Lachat, J.C., *A Further Development of the Boundary Integral Technique for Elastostatics*. 1975, Ph. D. Thesis, University of Southampton.

12. Lachat, J.C. and J.O. Watson, *Effective numerical treatment of boundary integral equations: a formulation for three-dimensional elastostatics.* International Journal for Numerical Methods in Engineering, 1976. **10**: p. 991-1005.

13. Cruse, T.A., F.J. Rizzo, and D. American Society of Mechanical Engineers Applied Mechanics, *Boundary-integral Equation Method: Computational Applications in Applied Mechanics: Presented at 1975 Applied Mechanics Conference, the Rensselaer Polytechnic Institute, Troy, New York, June 23-25, 1975*. 1975: American Society of Mechanical Engineers.

14. Lauricella, G., *Sull'integrazione delle equazioni dell'equilibrio dei corpi elastici isotropi*. 1905, Springer. p. 269-283.

15. Fredholm, I., *Solution d 'un problem fundamental de la theorie de 1' elastioite.* Arkiv for Matematik. Astronomic och Fvslk, 1905. **2**: p. 1-8.

16. Sokolnikoff, I.S., *Mathematical theory of elasticity*. 1956: New York.

17. Banerjee, P.K. and R. Butterfield, *Boundary Element Methods in Engineering Science*. 1981: London.

18. Lekhnitskii, S.G., *Theory of elasticity of an anisotropic elastic body*. 1963: Holden-Day San Francisco.

19. Tomlin, G.R. and R. Butterfield, *Elastic Analysis of Zoned Orthotropic Continua.* Proceedings of ASCE, 1974. **EM3**: p. 511-529.

20. Snyder, M.D. and T.A. Cruse, *Boundary-integral analysis of anisotropic cracked plates.* International Journal of Fracture, 1975. **11**: p. 315–328.

21. Crossman, F.W. and M.F. Ashby, *The Nonuniform Flow of Polycrystals by Grain-Boundary Sliding Accomodated by Power-Law Creep.* Acta Met, 1975. **23**(4): p. 425-440.

22. Ghahremani, F., *Effect of grain boundary sliding on anelasticity of polycrystals.* International Journal of Solids and Structures, 1980. **16**(9): p. 825-845.

23. Ghahremani, F., *Effect of grain boundary sliding on steady creep of polycrystals.* International Journal of Solids and Structures, 1980. **16**(9): p. 847-862.

24. Tvergaard, V., *Influence of grain boundary sliding on material failure in the tertiary creep range.* International Journal of Solids and Structures, 1985. **21**(3): p. 279-293.

25. Tvergaard, V., *Effect of grain boundary sliding on creep constrained diffusive cavitation.* Journal of the Mechanics and Physics of Solids, 1985. **33**(5): p. 447-469.

26. Fotiu, P.A., R. Heuer, and F. Ziegler, *BEM analysis of grain boundary sliding in polycrystals.* Engineering Analysis with Boundary Elements, 1995. **15**(4): p. 349-358.

27. Biner, S.B., *The role of grain boundary sliding and reinforcement morphology on the creep deformation behaviour of discontinuously reinforced composites.* Journal of Materials Science, 1996. **31**(13): p. 3459-3467.

28. Mura, T., *Micromechanics of Defects in Solids*. 1987: Springer.

29. Hull, D. and D.J. Bacon, *Introduction to Dislocations. International Series on Materials Science and Technology, Vol. 37*. 1965, Oxford: Pergamon Press.

30. Hirth, J.P. and J. Lothe, *Theory of Dislocations*. 1982. 857.

31. Mura, T., *Continuous distribution of moving dislocations.* Phil. Mag, 1963. **8**: p. 843-857.

32. Jr, W.J.W., *Elementary Dislocation Theory*. 1964: The Macmillan Co., London, England.

33. Nabarro, F.R.N., *Theory of Crystal Dislocations*. 1967: Clarendon Press.

34. Huang, H. and G.A. Kardomateus, *Dislocation-based boundary-element method for crack problems in anisotropic half-planes.* AIAA Journal, 2004. **42**(3): p. 650-657.

35. Eshelby, J.D., *Boundary Problems\ for Dislocations*, in *Dislocations in Solids*. 1979. p. 167-221.

36. Amodeo, R.J. and N.M. Ghoniem, *Dislocation dynamics. I. A proposed methodology for deformation micromechanics.* Physical Review B, 1990. **41**(10): p. 6958-6967.

37. Amodeo, R.J. and N.M. Ghoniem, *Dislocation dynamics. II. Applications to the formation of persistent slip bands, planar arrays, and dislocation cells.* Physical Review B, 1990. **41**(10): p. 6968-6976.

38. Kubin, L.P., et al., *Dislocation microstructures and plastic flow: a 3D simulation.* Solid State Phenomena, 1992. **23**(24): p. 455–472.

39. Van der Giessen, E. and A. Needleman, *Discrete dislocation plasticity: a simple planar model.* Model. Simul. Mater. Sci. Eng, 1995. **3**: p. 689–735.

40. Zbib, H.M., M. Rhee, and J.P. Hirth, *On plastic deformation and the dynamics of 3D dislocations.* International Journal of Mechanical Sciences, 1998. **40**(2): p. 113-127.

41. Schwarz, K.W., *Simulation of dislocations on the mesoscopic scale. I. Methods and examples.* Journal of Applied Physics, 1999. **85**(1): p. 108.

42. Roy, A. and A. Acharya, *Finite element approximation of field dislocation mechanics.* Journal of the Mechanics and Physics of Solids, 2005. **53**(1): p. 143-170.

43. Acharya, A., *A model of crystal plasticity based on the theory of continuously distributed dislocations.* Journal of the Mechanics and Physics of Solids, 2001. **49**(4): p. 761-784.

44. Acharya, A., *Driving forces and boundary conditions in continuum dislocation mechanics.* Proceedings: Mathematical, Physical and Engineering Sciences, 2003. **459**(2034): p. 1343-1363.

45. Acharya, A. and A. Roy, *Size effects and idealized dislocation microstructure at small scales: Predictions of a Phenomenological model of Mesoscopic Field Dislocation Mechanics: Part I.* Journal of the Mechanics and Physics of Solids, 2006. **54**(8): p. 1687-1710.

46. Roy, A. and A. Acharya, *Size effects and idealized dislocation microstructure at small scales: Predictions of a Phenomenological model of Mesoscopic Field Dislocation Mechanics: Part II.* Journal of the Mechanics and Physics of Solids, 2006. **54**(8): p. 1711-1743.

47. Acharya, A., *Constitutive analysis of finite deformation field dislocation mechanics.* Journal of the Mechanics and Physics of Solids, 2004. **52**(2): p. 301-316.

48. Gao, X.W., *The radial integration method for evaluation of domain integrals with boundary-only discretization.* Engineering Analysis with Boundary Elements, 2002. **26**(10): p. 905-916.

49. Gao, X.W., *A Boundary Element Method Without Internal Cells for Two-Dimensional and Three-Dimensional Elastoplastic Problems.* Journal of Applied Mechanics, 2002. **69**: p. 154.

50. Gao, X.W., *Evaluation of regular and singular domain integrals with boundary-only discretization—theory and Fortran code.* Journal of Computational and Applied Mathematics, 2005. **175**(2): p. 265-290.

51. Gao, X.W. and T.G. Davies, *An effective boundary element algorithm for 2D and 3D elastoplastic problems.* International Journal of Solids and Structures, 2000. **37**(36): p. 4987-5008.

52. Biner, S.B. and J.R. Morris, *A two-dimensional discrete dislocation simulation of the effect of grain size on strengthening behaviour*. 2002. p. 617-635.

53. Biner, S.B. and J.R. Morris, *The effects of grain size and dislocation source density on the strengthening behaviour of polycrystals: a two-dimensional discrete dislocation simulation*. 2003, Taylor & Francis. p. 3677-3690.

54. Zbib, H.M., et al., *3D dislocation dynamics: stress–strain behavior and hardening mechanisms in fcc and bcc metals.* Journal of Nuclear Materials, 2000. **276**(1-3): p. 154-165.

55. Foreman, A.J.E., *Junction reaction hardening by dislocation loops.* PHIL MAG, 1968. **17**(146): p. 353-364.

56. Hall, E.O., *The Deformation and Ageing of Mild Steel: III Discussion of Results.* Proceedings of the Physical Society Section B, 1951. **64**(9): p. 747-753.

57. Petch, N.J., *The cleavage strength of polycrystals.* Iron and Steel Institution of London Journal, 1953. **174**: p. 25–28.

CHAPTER TWO: BOUNDARY INTEGRAL EQUATION FORMULATION FOR 2D ISOTROPIC AND ANISOTROPIC ELASTOSTATICS

The boundary integral equations for plane elastostatics are derived by using a two step process: a) Determine the fundamental solutions for tractions and displacement and b) apply the Betti-Rayleigh Reciprocal Work Theorem. With the appropriate fundamental solutions, the derivations and the resulting equations are general enough to apply on both isotropic media and anisotropic media. In the following derivation, the index notion is used and the summation over repeated indices is implied.

2.1 Betti-Rayleigh Reciprocal Work Theorem

The Betti-Rayleigh reciprocal work theorem[1] relates two distinct and arbitrary loading conditions on the same elastic domain. For the domain Ω with piecewise smooth boundary Γ, the two states of equilibrium have strain, stress and displacement represented as $\varepsilon_{ij}, \sigma_{ij}, u_i$ in state (a) and $\varepsilon^*_{ij}, \sigma^*_{ij}, u^*_i$ in state (b). The relationship of stress, strain and displacement are:

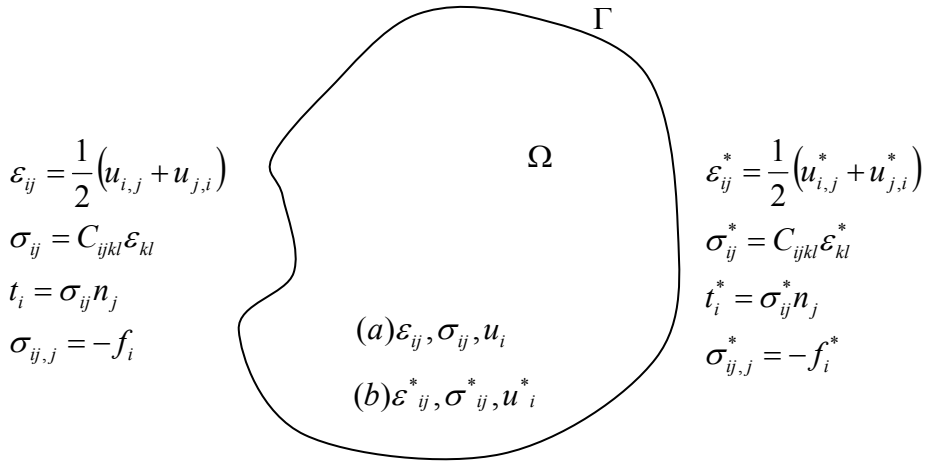

Figure 2.1 Elastic domain

For state (a)

$$\varepsilon_{i,j} = \frac{1}{2}\left(u_{i,j} + u_{j,i}\right) \text{ and } \sigma_{ij} = C_{ijkl}\varepsilon_{kl} \tag{2.1}$$

and for state (b)

$$\varepsilon^*_{i,j} = \frac{1}{2}\left(u^*_{i,j} + u^*_{j,i}\right) \text{ and } \sigma^*_{ij} = C_{ijkl}\varepsilon^*_{kl} \tag{2.2}$$

where C_{ijkl} is the material modulus matrix, and the subscript *(,n)* represents partial derivative with respect to the n^{th} coordinate's direction. For the elastic material, energy symmetry requires

$$C_{ijkl} = C_{klij} \tag{2.3}$$

From eqs. (2.1) to (2.3), it can be shown that,

$$\sigma_{ij}\varepsilon^*_{ij} = \sigma^*_{ij}\varepsilon_{ij} \tag{2.4}$$

Replacing strain terms with displacements terms in eqs. (2.1) and (2.2), eq. (2.4) becomes

$$\left(\sigma_{ij}u^*_i\right)_{,j} - \sigma_{ij,j}u^*_i = (\sigma^*_{ij}u_i)_{,j} - \sigma^*_{ij,j}u_i \tag{2.5}$$

The equilibrium equations of the two states are:

$\sigma_{ij,j} = -f_i$ for state (a) (2.6)

and

$\sigma^*_{ij,j} = -f^*_i$ for state (b) (2.7)

where f_i and f^*_i are the body force components. By replacing the stress derivative terms with body force terms in eqs. (2.6) and (2.7), eq. (2.5) can be written as

$$\left(\sigma_{ij}u^*_i\right),_j + f_i u^*_i = (\sigma^*_{ij}u_i),_j + f^*_i u_i \tag{2.8}$$

Furthermore, the tractions at a point on Γ are

$t_i = \sigma_{ij}n_j$ for state (a) (2.9)

and

$t^*_i = \sigma^*_{ij}n_j$ for state (b) (2.10)

where n_j are the components of the outward normal of boundary Γ. By integrating eq. (2.8) over the domain Ω and applying the divergence theorem, the remaining stress terms in eq. (2.8) are replaced by tractions terms in eqs. (2.9) and (2.10), and eq. (2.8) becomes

$$\int_\Gamma t_i u^*_i d\Gamma + \int_\Omega f_i u^*_i d\Omega = \int_\Gamma t^*_i u_i d\Gamma + \int_\Omega f^*_i u_i d\Omega \tag{2.11}$$

The above equation can be interpreted as the equality of the work done by the forces in state (a) acting through displacements in state (b), and the work done by the forces in state (b) acting through displacements in state (a). This is known as the Betti-Rayleigh reciprocal work theorem.

The Betti-Rayleigh reciprocal work theorem can be used for the solution of the equilibrium equations for state (a) by choosing the variables $\sigma^*_{ij}, u^*_i, f^*_i$ for state (b). The

chosen expressions of $\sigma^*_{ij}, u^*_i, f^*_i$ are called the fundamental solutions. The fundament solutions can be determined by implementing simple loading conditions on state (a). Brief derivation for both isotropic media and anisotropic media fundamental solutions is presented next.

2.2 Isotropic Fundamental Solution

For isotropic material, the strain is defined as

$$\varepsilon_{i,j} = \frac{1}{2}\left(u_{i,j} + u_{j,i}\right) \tag{2.12}$$

and the isotropic stress strain relationship is

$$\sigma_{ij} = \frac{2G\nu}{1-2\nu}\sigma_{ij}\varepsilon_{mm} + 2G\varepsilon_{ij} \tag{2.13}$$

where G is the shear modulus and ν is the Poisson's ratio. The equilibrium equation is expressed as

$$\sigma_{ij,j} = -f_i \tag{2.14}$$

By combining eqs. (2.12), (2.13), and (2.14), the Navier's equations for plane-elastostatics are obtained as:

$$\frac{1}{1-2\nu}\left\{\frac{\partial^2 u_1}{\partial x_1^2} + \frac{\partial^2 u_2}{\partial x_1 \partial x_2}\right\} + \frac{\partial^2 u_1}{\partial x_1^2} + \frac{\partial^2 u_1}{\partial x_2^2} + f_1/G = 0 \tag{2.15}$$

$$\frac{1}{1-2\nu}\left\{\frac{\partial^2 u_1}{\partial x_1 \partial x_2} + \frac{\partial^2 u_2}{\partial x_2^2}\right\} + \frac{\partial^2 u_2}{\partial x_1^2} + \frac{\partial^2 u_2}{\partial x_2^2} + f_2/G = 0 \tag{2.16}$$

where x_1 and x_2 are the Cartesian co-ordinates and

$$u_1 = u_1(x_1, x_2); f_1 = f_1(x_1, x_2) \tag{2.17}$$

$$u_2 = u_2(x_1, x_2); f_2 = f_2(x_1, x_2) \tag{2.18}$$

while $u_3 = 0$ for plane strain and $f_3 = 0$ for plane stress.

To solve Navier's eqs. (2.15) and (2.16), two simple loading conditions are defined as unit point force on orthogonal directions acting at the same source point.

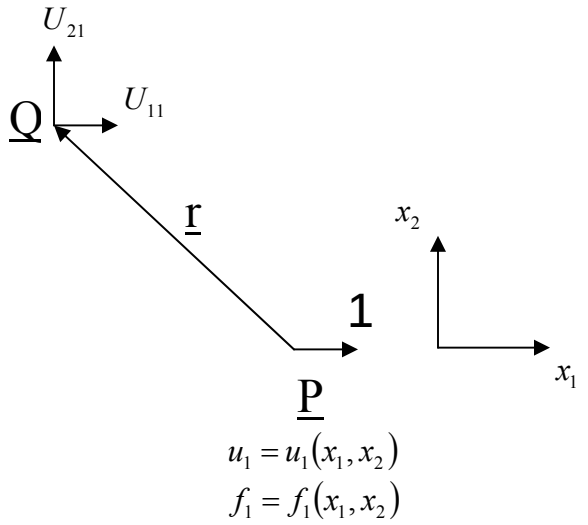

Figure 2.2 loading case one

Loading case one is due to a point force of unit magnitude at the source point P in the x_1 direction as shown in Figure 2.2. By applying this unit force along x_1 direction at P

$$\underline{f}^{(1)} = \delta(\underline{q} - \underline{p})\underline{e}_1 \tag{2.19}$$

the displacement at point Q is

$$\underline{u}^{(1)} = U_{11}\underline{e}_1 + U_{21}\underline{e}_2 \tag{2.20}$$

where $\underline{e}_1$ and $\underline{e}_2$ are the unit vectors in the x_1 and x_2 directions respectively.

Loading case two is due to a point force of unit magnitude at the same source point P in the x_2 direction as shown in Figure 2.3. Again by applying this unit force along x_2 direction at P

$$\underline{f}^{(2)} = \delta(\underline{q} - \underline{p})\underline{e}_2 \tag{2.21}$$

the displacement at point Q is

$$\underline{u}^{(2)} = U_{12}\underline{e}_1 + U_{22}\underline{e}_2 \tag{2.22}$$

In general, eqs. (2.19) – (2.22) can be expressed as

$$\underline{f}^{(k)} = \delta_{ik}\delta(\underline{q} - \underline{p})\underline{e}_i \tag{2.23}$$

$$\underline{u}^{(k)} = U_{ik}\underline{e}_i \tag{2.24}$$

where U_{ik} is the displacement at Q in the ith direction due to a unit load at P in the kth direction.

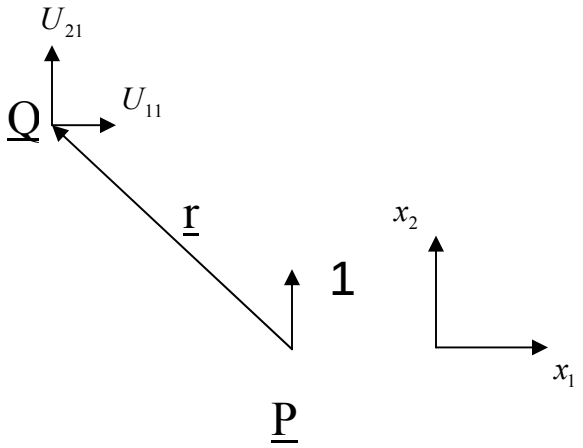

$$u_2 = u_2(x_1, x_2)$$
$$f_2 = f_2(x_1, x_2)$$

Figure 2.3 loading case two

For the first loading case, Navier's eqs (2.15) and (2.16) become

$$\frac{1}{1-2\nu}\left\{\frac{\partial^2 U_{11}}{\partial x_1^2}+\frac{\partial^2 U_{21}}{\partial x_1 \partial x_2}\right\}+\frac{\partial^2 U_{11}}{\partial x_1^2}+\frac{\partial^2 U_{11}}{\partial x_2^2}+\frac{\delta(\underline{q}-\underline{p})}{G}=0 \tag{2.25}$$

$$\frac{1}{1-2\nu}\left\{\frac{\partial^2 U_{11}}{\partial x_1 \partial x_2}+\frac{\partial^2 U_{21}}{\partial x_2^2}\right\}+\frac{\partial^2 U_{21}}{\partial x_1^2}+\frac{\partial \partial^2 U_{21}}{\partial x_2^2}+0=0 \tag{2.26}$$

And for the second loading case, Navier's eqs (2.15) and (2.16) become

$$\frac{1}{1-2\nu}\left\{\frac{\partial^2 U_{12}}{\partial x_1^2}+\frac{\partial^2 U_{22}}{\partial x_1 \partial x_2}\right\}+\frac{\partial^2 U_{12}}{\partial x_1^2}+\frac{\partial^2 U_{12}}{\partial x_2^2}+0=0 \tag{2.27}$$

$$\frac{1}{1-2\nu}\left\{\frac{\partial^2 U_{12}}{\partial x_1 \partial x_2}+\frac{\partial^2 U_{22}}{\partial x_1^2}\right\}+\frac{\partial^2 U_{22}}{\partial x_1^2}+\frac{\partial^2 U_{22}}{\partial x_2^2}+\frac{\delta(\underline{q}-\underline{p})}{G}=0 \tag{2.28}$$

These four partial differential equations (2.25) to (2.28) can be solved by using Fourier transform to yield

$$U_{ij} = \frac{1}{8\pi(1-\nu)G}\left\{(3-4\nu)\delta_{ij}\log r + \frac{y_i y_j}{r^2}\right\} \tag{2.29}$$

for plane stain, where

$$y_i = (q_i - p_i)$$
$$y_j = (q_j - p_j)$$
$$r^2 = y_m y_m = (q_1 - p_1)^2 + (q_2 - p_2)^2$$

Where G is the shear modulus, ν is the Poisson's ratio. For plane stress, ν is replaced by $\nu/(1+\nu)$ in eq. (2.29).

For a general case of unit load in the k[th] direction at point P, the corresponding displacements, stresses, strains and tractions are defined by dropping the superscript (k) from (2.23) and (2.24)

$u_i = U_{ik}$, displacement at the point Q in the i[th] direction

$\varepsilon_{ij} = B_{ijk}$, strain at the point Q

$\sigma_{ij} = T_{ijk}$, stress at the point Q

$t_i = T_{ik}$, traction at the point Q in the i[th] direction

To obtain strains thru eq. (2.12), the derivative $U_{ik,j}$ is needed. Here subscript j denotes $\partial/\partial q_j$ which is the derivative taken at point Q along the co-ordinate direction j. Using the relationship $\frac{\partial r}{\partial q_j} = y_j / r$, $U_{ik,j}$ is obtained as

$$U_{ik,j} = \frac{-1}{8\pi(1-\nu)G}\left\{(3-4\nu)\delta_{ik}y_j/r^2 - \delta_{jk}y_i/r^2 - \delta_{kj}y_i/r^2 + 2y_i y_j y_k/r^4\right\} \tag{2.30}$$

By using eqs. (2.12) and (2.13), strain and stress at Q can be expressed as

$$B_{ijk} = \frac{-1}{8\pi(1-\nu)Gr^2}\left\{(1-2\nu)(\delta_{ik}y_j + \delta_{jk}y_i) - \delta_{ij}y_k + 2y_iy_jy_k/r^2\right\} \tag{2.31}$$

$$T_{ijk} = \frac{-1}{4\pi(1-\nu)r^2}\left\{(1-2\nu)(\delta_{ik}y_j + \delta_{jk}y_i - \delta_{ij}y_k) + 2y_iy_jy_k/r^2\right\} \tag{2.32}$$

By using the definition of traction

$$t_i = \sigma_{ij}n_j \tag{2.33}$$

the traction at Q is obtained as

$$T_{ik} = T_{ijk}n_j = \frac{-1}{4\pi(1-\nu)r^2}\left[(1-2\nu)(y_in_k - y_kn_i) + \left\{(1-2\nu)\sigma_{ik} + 2y_iy_k/r^2\right\}y_jn_j\right] \tag{2.34}$$

Thus, eq. (2.29) is the displacement fundamental solution and eq. (2.34) is the traction fundamental solution for isotropic media[2-4].

2.3 Boundary Integral Equation

In the Betti-Rayleigh work theorem, state (a) corresponds to the actual equilibrium problem on the domain Ω with surface Γ. Either the traction $\underline{t}$ or the displacement $\underline{u}$ is specified on surface Γ as boundary condition. The body force $\underline{f}$ over domain Ω should also be specified. The state (b) is that of a unit point load in an infinite elastic medium with the same material property as state (a) where the isotropic displacement fundamental solution eq. (2.29) and the traction fundamental solution eq. (2.34) are derived in the previous section.

The unit components of the point force $\underline{f}^*$ at the load point Q are taken as

$$f_i^* = \delta_{ik}\delta(\underline{q} - \underline{p}) \tag{2.35}$$

By inserting eq. (2.35) into the second integral on the left-hand-side of the Betti-Rayleigh work theorem eq. (2.11), one can obtain

$$\int_\Omega f_i^* u_i d\Omega = \int_\Omega \delta_{ik}\delta(\underline{q}-\underline{p})u_i(\underline{q})d\Omega = \delta_{ik}u_i(\underline{p}) = u_k(\underline{p}) \tag{2.36}$$

By inserting $U_{ik}(\underline{p},\underline{q}), T_{ik}(\underline{p},\underline{q})$ as u* and t*, eq. (2.11) can be rewritten as[2, 5-7]

$$u_k(\underline{p}) = \int_\Gamma \left[t_i(\underline{q})U_{ik}(\underline{p},\underline{q}) - u_i(\underline{q})T_{ik}(\underline{p},\underline{q})\right]d\Gamma(\underline{q}) + \int_\Omega f_i(\underline{q})U_{ik}(\underline{p},\underline{q})d\Omega(\underline{q}) \tag{2.37}$$

where k=1,2. Equation (2.37) can be used to calculate the displacement at any given interior point with known displacements and tractions on the boundary as a post processing.

By moving the interior point $\underline{p}$ to the boundary, the expression relating the displacements at a point on the boundary with the displacements and tractions on the rest of the boundary and the body force over the domain, can be obtained. This is done by limiting $\underline{p}$ to the boundary point $\underline{p_0}$. The singularity at the boundary point $\underline{p_0}$ is removed by distorting the boundary to bypass $\underline{p_0}$. The final form of the boundary integral equation is

$$C_{ik}(\underline{p})u_k(\underline{p}) = \int_\Gamma \left[t_i(\underline{q})U_{ik}(\underline{p},\underline{q}) - u_i(\underline{q})T_{ik}(\underline{p},\underline{q})\right]d\Gamma(\underline{q}) + \int_\Omega f_i(\underline{q})U_{ik}(\underline{p},\underline{q})d\Omega(\underline{q}) \tag{2.38}$$

with $\underline{p}$ located on the boundary.

The value of $C_{ik}(\underline{p})$ can be calculated indirectly by the rigid body motion requirement. For a traction free rigid body motion, $t_i(\underline{q}) = 0$ and $f_i(\underline{q}) = 0$. Denoting the displacement in such a situation by the superscript R, eq.(2.38) becomes

$$C_{ik}(\underline{p})u^R{}_k(\underline{p}) = -\int_\Gamma u^R{}_i(\underline{q})T_{ik}(\underline{p},\underline{q})d\Gamma(\underline{q}) \tag{2.39}$$

For rigid body motion,

$$u^R{}_k(\underline{p}) = u^R{}_k(\underline{q}) \tag{2.40}$$

Since eq. (2.39) must hold for all none zero displacement, therefore, by combining eq. (2.40) and eq. (2.39), one can obtain

$$C_{ik}(\underline{p}) = -\int_\Gamma T_{ik}(\underline{p},\underline{q})d\Gamma(\underline{q}) \tag{2.41}$$

For plane elastostatics problems without body force, the boundary integral equations are

$$C_{ik}(\underline{p})u_k(\underline{p}) = \int_\Gamma \left[t_i(\underline{q})U_{ik}(\underline{p},\underline{q}) - u_i(\underline{q})T_{ik}(\underline{p},\underline{q})\right]d\Gamma(\underline{q}) \tag{2.42}$$

In matrix notation, eq. (2.42) becomes

$$\begin{bmatrix} C_{11} & C_{12} \\ C_{21} & C_{22} \end{bmatrix}^T \begin{Bmatrix} u_1 \\ u_2 \end{Bmatrix} = \int \begin{bmatrix} U_{11} & U_{12} \\ U_{21} & U_{22} \end{bmatrix}^T \begin{Bmatrix} t_1 \\ t_2 \end{Bmatrix} - \begin{bmatrix} T_{11} & T_{12} \\ T_{21} & T_{22} \end{bmatrix}^T \begin{Bmatrix} u_1 \\ u_2 \end{Bmatrix} d\Gamma \tag{2.43}$$

The above is a system of equations involving four variables (u_1, u_2, t_1, t_2). Two of them must be specified as prescribed boundary conditions and the other two are obtained by solving the system of eq. (2.43). Since a close form solution of the BIE is generally impossible, except for very simple geometry and prescribed boundary conditions, a numerical solution is generally attempted. A detailed description of the numerical solution will be described in chapter 3.

2.4 Calculation of the Internal Stresses

The stresses in the interior of the domain Ω are determined after the surface tractions and displacements are obtained from eq. (2.43). Appling eq. (2.38) without body force term and with the strain displacement relationship, the strain at any given interior point is obtained as

$$\varepsilon_{ij}(\underline{p}) = \int_{\Gamma}\left[t_k(\underline{q})D_{ijk}(\underline{p},\underline{q}) - u_k(\underline{q})C_{ijk}(\underline{p},\underline{q})\right]d\Gamma(\underline{q}) \tag{2.44}$$

where

$$D_{ijk}(\underline{p},\underline{q}) = 1/2\left(\frac{\partial U_{ik}}{\partial p_j} + \frac{\partial U_{jk}}{\partial p_i}\right) \tag{2.45}$$

$$C_{ijk}(\underline{p},\underline{q}) = 1/2\left(\frac{\partial T_{ik}}{\partial p_j} + \frac{\partial T_{jk}}{\partial p_i}\right) \tag{2.46}$$

The internal stress are obtained by applying the stress strain relationship as

$$\sigma_{ij}(\underline{p}) = \int_{\Gamma}\left[t_k(\underline{q})F_{ijk}(\underline{p},\underline{q}) - u_k(\underline{q})E_{ijk}(\underline{p},\underline{q})\right]d\Gamma(\underline{q}) \tag{2.47}$$

For isotropic material,

$$F_{ijk}(\underline{p},\underline{q}) = \left[\frac{2G\nu}{1-2\nu}\delta_{ij}\frac{\partial U_{mk}}{\partial p_m} + G\left(\frac{\partial U_{ik}}{\partial p_j} + \frac{\partial U_{jk}}{\partial p_i}\right)\right] \tag{2.48}$$

$$E_{ijk}(\underline{p},\underline{q}) = \left[\frac{2G\nu}{1-2\nu}\delta_{jk}\frac{\partial T_{mk}}{\partial p_m} + G\left(\frac{\partial T_{ik}}{\partial p_j} + \frac{\partial T_{jk}}{\partial p_i}\right)\right] \tag{2.49}$$

After simplification,

$$F_{ijk}(\underline{p},\underline{q}) = a_1/r\left[a_1/r(\delta_{ik}y_j + \delta_{jk}y_i - \delta_{ij}y_k) + \frac{2y_i y_j y_k}{r^3}\right] \tag{2.50}$$

$$\begin{aligned} E_{ijk}(\underline{p},\underline{q}) = \frac{a_3}{r^3}\Bigg[&\frac{n_l y_l}{r^2}\left\{2a_2\delta_{ij}y_k + 2\nu(\delta_{ik}y_j + \delta_{jk}y_i) - \frac{8y_i y_j y_k}{r^2}\right\} \\ &+ n_i\left(2\nu\frac{y_j y_k}{r^2} + a_2\delta_{jk}\right) + n_j\left(2\nu\frac{y_i y_k}{r^2} + a_2\delta_{ik}\right) + n_k\left(2a_2\frac{y_i y_j}{r^2} - a_4\delta_{ij}\right)\Bigg] \end{aligned} \tag{2.51}$$

where

$$
\begin{aligned}
a_1 &= \frac{1}{4\pi(1-\nu)} \\
a_2 &= 1-2\nu \\
a_1 &= \frac{G}{2\pi(1-\nu)} \\
a_2 &= 1-a\,\nu \\
y_i &= q_i - p_i
\end{aligned}
\tag{2.52}
$$

2.5 Anisotropic Fundamental Solution

The anisotropic fundamental solution is derived in terms of Airy functions and complex variables[8-17]. The two dimensional stress-strain relationships for homogeneous generally anisotropic elastic body in a plane in a matrix form is[18]

$$
\begin{bmatrix} \varepsilon_{11} \\ \varepsilon_{22} \\ 2\varepsilon_{12} \end{bmatrix} = \begin{bmatrix} a_{11} & a_{12} & a_{16} \\ a_{12} & a_{22} & a_{26} \\ a_{16} & a_{26} & a_{66} \end{bmatrix} \begin{bmatrix} \sigma_{11} \\ \sigma_{22} \\ \sigma_{12} \end{bmatrix}
\tag{2.53}
$$

where σ_{ij} and ε_{ij} (i,j=1,2), are the stresses and strains, and a_{mn} are the elastic compliances of the material. In terms of engineering constants, these compliances can be expressed as

$$
\begin{aligned}
&a_{11} = 1/E_1\,; a_{22} = 1/E_2 \\
&a_{66} = 1/G_{12}\,; a_{12} = -\upsilon_{12}/E_1 = -\upsilon_{21}/E_2 \\
&a_{16} = \eta_{12,1}/E_1 = \eta_{1,12}/G_{12} \\
&a_{26} = \eta_{12,3}/E_2 = \eta_{2,12}/G_{12}
\end{aligned}
\tag{2.54}
$$

where E_k is the young's modulus in the x_k direction, G_{12} is the shear modulus in the x_1-x_2 plane, and υ_{ij} is the Poisson's ratio. The quantities $\eta_{ij,k}$ and $\eta_{k,ij}$ are coefficients of mutual influence of the first and second kind. They are zero for orthotropic materials.

In the case of plane strain problems, eq. (2.54) remains applicable, provided that a_{jk} is replaced by b_{jk} where

$$b_{jk} = a_{jk} - a_{j3}a_{k3}/a_{33}; j,k = 1,2 \tag{2.55}$$

and

$$\begin{aligned} a_{j3} &= -\upsilon_{j3}/E_j = -\upsilon_3/E_3 ; a_{33} = 1/E_3 \\ a_{63} &= \eta_{12,3}/E_3 = \eta_{3,12}/G_{12} \end{aligned} \tag{2.56}$$

where the index 3 refers to the x_3 direction.

If the Airy's stress function, ϕ, is introduced as

$$\sigma_{11} = \partial^2 \phi/\partial x_2^2 ; \sigma_{22} = \partial^2 \phi/\partial x_1^2 ; \sigma_{12} = -\partial^2 \phi/\partial x_1 \partial x_2 ; \tag{2.57}$$

the equations of equilibrium for plane problems are satisfied. Using the equations of compatibility of strains,

$$\frac{\partial^2 \varepsilon_{11}}{\partial x_2^2} + \frac{\partial^2 \varepsilon_{22}}{\partial x_1^2} = \frac{\partial^2 \varepsilon_{12}}{\partial x_1 \partial x_2} \tag{2.58}$$

and the stress strain relationship eq. (2.53), the governing equation for the two dimensional anisotropic elasticity problems can be obtained as

$$a_{22}\frac{\partial^4 \phi}{\partial x_1^4} - 2a_{26}\frac{\partial^4 \phi}{\partial x_1^3 \partial x_2} + (2a_{12} + a_{66})\frac{\partial^4 \phi}{\partial x_1^2 \partial x_2^2} - 2a_{16}\frac{\partial \phi^4}{\partial x_1 \partial x_2^3} + a_{66}\frac{\partial^4 \phi}{\partial x_2^4} = 0 \tag{2.59}$$

The solution of eq. (2.59) can be defined in terms of a complex coordinate as

$$z = x_1 + \mu x_2 \tag{2.60}$$

where

$$\mu = \alpha + i\beta \tag{2.61}$$

Substituting eq. (2.60) into eq. (2.59), the characteristic equation for μ is obtained as

$$a_{11}\mu^4 - 2\mu a_{16} + (2a_{12} + a_{66})\mu^2 - 2a_{26}\mu + a_{22} = 0 \tag{2.62}$$

For an anisotropic material, the four roots of eq.(2.60) are distinct and must be either purely imaginary or complex, so they can be denoted as

$$\mu_1 = \alpha_1 + i\beta_{1;}\mu_2 = \alpha_2 + i\beta_2; \mu_3 = \overline{\mu_1}; \mu_4 = \overline{\mu_2} \tag{2.63}$$

The characteristic directions may thus be denoted as

$$z_j = x_1 + \mu_j x_2 \tag{2.64}$$

To calculate the anisotropic fundamental solutions, the Airy function is rewritten in term of z as

$$F\left(z_{1,}z_2\right) = F_1(z_1) + F_2(z_2) + \overline{F_1(z_1)} + \overline{F_2(z_2)} = 2\,\mathrm{Re}\left[F_1(z_1) + F_2(z_2)\right] \tag{2.65}$$

The stresses are expressed as

$$\sigma_{11} = 2\,\mathrm{Re}\left[\mu_1^2 \frac{d^2F_1}{dz_1^2} + \mu_2^2 \frac{d^2F_2}{dz_2^2}\right], \tag{2.66}$$

$$\sigma_{22} = 2\,\mathrm{Re}\left[\frac{d^2F_1}{dz_1^2} + \frac{d^2F_2}{dz_2^2}\right], \tag{2.67}$$

$$\sigma_{12} = -2\,\mathrm{Re}\left[\mu_1^2 \frac{d^2F_1}{dz_1^2} + \mu_2^2 \frac{d^2F_2}{dz_2^2}\right] \tag{2.68}$$

To get the displacement expression, the first step is to insert the Hook's law eq. (2.53) into stress function eqs. (2.66) to (2.68) to replace stress with strain, then replace strain with displacement by eq. (2.12). The next step is to integrate both left hand side and right hand side of the equations by one dimension to get rid of the displacement derivatives. Thus one can obtain

$$\begin{aligned} u(x,y) &= 2\,\mathrm{Re}\left[p_1\phi_1 + p_2\phi_2\right] \\ v(x,y) &= 2\,\mathrm{Re}\left[q_1\phi_1 + q_2\phi_2\right] \end{aligned} \tag{2.69}$$

where

$$p_k = a_{11}\mu_k^2 + a_{12} - a_{16}\mu_k$$
$$q_k = a_{22}/\mu_k + a_{12}\mu_k - a_{26} \tag{2.70}$$

and

$$\phi_i = dF_i / dz_i \tag{2.71}$$

Similar to isotropic fundamental derivation, special loading cases are applied to eqs. (2.69). For the unit magnitude net force, P_x=1 for case-one and P_y=1 for case-two, applied at the same source point with orthogonal directions, one obtains

$$P_x = \sum_{k=1}^{2} [\![\mu_k \phi_k + \overline{\mu}_k \overline{\phi}_k]\!] = 1$$
$$P_y = -\sum_{k=1}^{2} [\![\phi_k + \overline{\phi}_k]\!] = 1 \tag{2.72}$$

Since single value displacement is required at the same point, two more restrictions can be applied

$$\left[\left[\mathrm{Re}(\sum_{k=1}^{2} p_k \phi_k) \right]\right] \equiv 0$$
$$\left[\left[\mathrm{Re}(\sum_{k=1}^{2} q_k \phi_k) \right]\right] \equiv 0 \tag{2.73}$$

The fundamental solution is assumed to have the form

$$\phi_{ik} = A_{ik} \log(z_k) \tag{2.74}$$

By inserting this form into the special conditions eqs. (2.72) and (2.73), the fundamental solutions can be expressed in term of constants A as

$$\sum_{k=1}^{2} (A_{jk} - \overline{A}_{jk}) = \delta_{j2}/2\pi i$$
$$-\sum_{k=1}^{2} (\mu_k A_{jk} - \overline{\mu}_k \overline{A}_{jk}) = \delta_{j1}/2\pi i \tag{2.75}$$

$$\sum_{k=1}^{2}(p_k A_{jk} - \overline{p}_k \overline{A}_{jk}) = 0$$
$$-\sum_{k=1}^{2}(q_k A_{jk} - \overline{q}_k \overline{A}_{jk}) = 0 \tag{2.76}$$

The constants A are determined by solving eqs. (2.75) and (2.76). After the constants A are solved, it can be plugged into eq. (2.69) to obtain the displacement fundamental solution. Then from eqs. (2.12), (2.13) and (2.33), strain, stress and traction fundamental solutions are derived in terms of A. The final form for the anisotropic displacement and traction fundamental solutions are given below[19, 20]

$$U_{jk} = 2\,\mathrm{Re}\left[r_{k1} A_{j1} \ln(z_1) + r_{k2} A_{j2} \ln(z_2)\right] \tag{2.77}$$

$$T_{j1} = 2n_1\,\mathrm{Re}\left[\mu_1^2\, A_{j1}/z_1 + \mu_2^2\, A_{j2}/z_2\right] - 2n_2\,\mathrm{Re}\left[\mu_1\, A_{j1}/z_1 + \mu_2\, A_{j2}/z_2\right] \tag{2.78}$$

$$T_{j2} = -2n_1\,\mathrm{Re}\left[\mu_1\, A_{j1}/z_1 + \mu_2\, A_{j2}/z_2\right] + 2n_2\,\mathrm{Re}\left[A_{j1}/z_1 + A_{j2}/z_2\right] \tag{2.79}$$

In eqs. (2.77) to (2.79), n_j is the unit outward normal component at Q.

where

$$r_{1j} = a_{11}\mu_j^2 + a_{12} - a_{16}\mu_j$$
$$r_{2j} = a_{12}\mu_j + a_{22}/\mu_j - a_{26} \tag{2.80}$$

and A_{jk} are complex constants which can be obtained by solving the following system of equations expressed in matrix form

$$\left[\mathrm{Im}\{B_1\}\mathrm{Re}\{B_1\}\mathrm{Im}\{B_2\}\mathrm{Re}\{B_2\}\right] * \begin{bmatrix} \mathrm{Im}\{A_{j1}\} \\ \mathrm{Re}\{A_{j1}\} \\ \mathrm{Im}\{A_{j2}\} \\ \mathrm{Re}\{A_{j2}\} \end{bmatrix} = \begin{bmatrix} -\frac{1}{4\pi}\delta_{j2} \\ \frac{1}{4\pi}\delta_{j1} \\ 0 \\ 0 \end{bmatrix} \tag{2.81}$$

where

$$\{B_k\} = \{i\mu_k r_{1k} r_{2k}\}^T ; k = 1,2 \tag{2.82}$$

To summarize the anisotropic fundamental solution derivation, a quartic equation (2.62) is first solved to get the solution for two conjugate pair of μ, and then two roots of μ from different conjugate pairs are inserted in system of eqs. (2.81) and (2.82) to determine the constants A. All the parameters in the fundamental solutions can be represented by A and μ. Furthermore, all those constants A, r, and μ depends on the value of a_{mn}, the elastic compliances of the material.

After the fundamental solution is derived, the boundary integral formulation for anisotropic materials is exactly the same as isotropic materials given by eqs. (2.38) to (2.43).

For the internal stress calculation without body force, the anisotropic expression similar to eq. (2.44) is derived as

$$\varepsilon_{jl}(p) = \frac{1}{2}\left[\oint_s u_i \widetilde{T}_{jli}(p,Q)dS - \oint_s t_i \widetilde{U}_{jli}(p,Q)dS\right] \tag{2.83}$$

where $\widetilde{T}_{jil}(p,Q)$ and $\widetilde{U}_{jil}(p,Q)$ are given by

$$\widetilde{T}_{jil}(p,Q) = \frac{\partial T_{ji}(p,Q)}{\partial x_l} + \frac{\partial T_{li}(p,Q)}{\partial x_j} = 2\,\mathrm{Re}\left(\frac{\hat{\mu}_{i1}(n_2 - \mu_1 n_1)G_{jl1}}{z_1^2} + \frac{\hat{\mu}_{i2}(n_2 - \mu_2 n_1)G_{jl2}}{z_2^2}\right) \tag{2.84}$$

and

$$\widetilde{U}_{jil}(p,Q) = \frac{\partial U_{ji}(p,Q)}{\partial x_l} + \frac{\partial U_{li}(p,Q)}{\partial x_j} = 2\,\mathrm{Re}\left(\frac{r_{i1}G_{jl1}}{z_1} + \frac{r_{i2}G_{jl2}}{z_2}\right) \tag{2.85}$$

The following coefficients

$$\hat{\mu}_{mn} = \begin{bmatrix} \mu_1 & \mu_2 \\ -1 & -1 \end{bmatrix}, \hat{\mu}_{mn} = \begin{bmatrix} 1 & 1 \\ \mu_1 & \mu_2 \end{bmatrix} \tag{2.86}$$

are inserted in eq. (2.84) and (2.85) to obtain

$$G_{jl1} = A_{j1}\widetilde{\mu}_{l1} + A_{l1}\widetilde{\mu}_{j1}, G_{jl2} = A_{j2}\widetilde{\mu}_{l2} + A_{l2}\widetilde{\mu}_{j2} \tag{2.87}$$

Once the interior strain is obtained by using eq. (2.83), the stress at p can be calculated from the stress strain relationship equations which are the inverse form of eq. (2.53).

References:

1. Betti, E., *Teori dell elasticita.* II Nuovo Cimento, 1872: p. 7-10.
2. Banerjee, P.K. and R. Butterfield, *Boundary Element Methods in Engineering Science*. 1981: London.
3. Brebbia, C.A. and J. Dominguez, *Boundary elements: an introductory course*. 1992: Computational Mechanics Publications.
4. Brebbia, C.A., J.C.F. Telles, and L.C. Wrobel, *Boundary element techniques: Theory and applications in engineering*. 1984.
5. Beer, G., *Programming the Boundary Element Method*. 2000: John Wiley & Sons, Inc. New York, NY, USA.
6. Beer, G. and J.O. Watson, *Introduction to Finite and Boundary Element Methods for Engineers*. 1992: Wiley.
7. Gao, X.W. and T.G. Davies, *Boundary Element Programming in Mechanics*. 2002: Cambridge University Press.
8. Shiah, Y.C. and C.L. Tan, *Determination of interior point stresses in two dimensional BEM thermoelastic analysis of anisotropic bodies.* International Journal of Solids and Structures, 2000. **37**(5): p. 809-829.

9. Zhang, J.J., C.L. Tan, and F.F. Afagh, *Treatment of body-force volume integrals in BEM by exact transformation for 2-D anisotropic elasticity.* International Journal for Numerical Methods in Engineering, 1997. **40**(1): p. 89-109.

10. Tan, C.L., Y.L. Gao, and F.F. Afagh, *Anisotropic stress analysis of inclusion problems using the boundary integral equation method.* Journal of Strain Analysis for Engineering Design, 1992. **27**(2): p. 67-76.

11. Shiah, Y.C. and C.L. Tan, *Calculation of interior point stresses in two-dimensional boundary element analysis of anisotropic bodies with body forces.* The Journal of Strain Analysis for Engineering Design, 1999. **34**(2): p. 117-128.

12. Garci´a, F., A. Sáez, and J. Domi´nguez, *Traction boundary elements for cracks in anisotropic solids.* Engineering Analysis with Boundary Elements, 2004. **28**(6): p. 667-676.

13. Chen, H.B., et al., *An effective method for finding values on and near boundaries in the elastic BEM.* Computers and Structures, 1998. **69**(4): p. 421-431.

14. Albuquerque, E.L., P. Sollero, and M.H. Aliabadi, *The boundary element method applied to time dependent problems in anisotropic materials.* International Journal of Solids and Structures, 2002. **39**(5): p. 1405-1422.

15. Tafreshi, A., *Shape design sensitivity analysis of 2D anisotropic structures using the boundary element method.* Engineering Analysis with Boundary Elements, 2002. **26**(3): p. 237-251.

16. Schclar, N.A., *Anisotropic Analysis Using Boundary Elements*. 1994: Computational Mechanics Publications.

17. Rizzo, F.J. and D.J. Shippy, *A Method for Stress Determination in Plane Anisotropic Elastic Bodies.* Journal of Composite Materials, 1970. **4**(1): p. 36.

18. Lekhnitskii, S.G., *Theory of elasticity of an anisotropic elastic body*. 1963: Holden-Day San Francisco.

19. Cruse, T.A., *Boundary Element Analysis in Computational Fracture Mechanics*. 1988: Springer.

20. Snyder, M.D. and T.A. Cruse, *Boundary-integral analysis of anisotropic cracked plates.* International Journal of Fracture, 1975. **11**: p. 315–328.

CHAPTER THREE: NUMERICAL IMPLEMENTATION FOR BOUNDARY ELEMENT METHOD AND GRAIN SLIDING

3.1 Introduction

The discretization and collocation of the boundary integral equations is a three-step process[1-5].

1. The boundary is broken up into elements.
2. The variables, such as displacement and traction, are expressed in terms of nodal values and polynomial shape functions.
3. The product of the shape function and the kernel functions are integrated over each boundary element.

The boundary is broken up into straight elements as shown in Figure 2.1. On each element the variation of any quantity is assumed to be linear. Thus, all variables are expressed as a linear combination of two linear interpolating functions and two nodal values. Each element contains two nodes at the two ends of the element.

Gauss quadrature is introduced to integrate the product of the shape functions and the fundamental solutions over the element. Various orders of Gauss quadrature is implemented depending on the accuracy requirement.

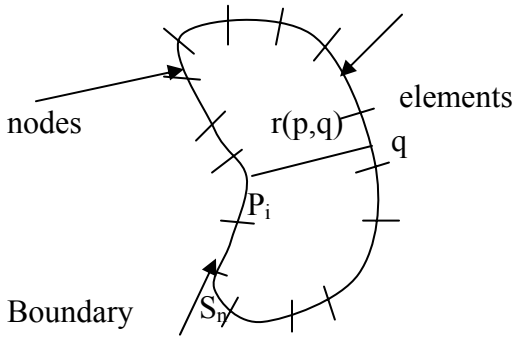

Figure 3.1: Elements and nodes on boundary

3.2 Numerical Discretization and Isoparametric Formulation

In the first step, boundary S is divided into N_e elements, so the boundary integral equation

$$C_{ik}(\underline{p})u_k(\underline{p}) = \int_\Gamma \left[t_i(\underline{q})U_{ik}(\underline{p},\underline{q}) - u_i(\underline{q})T_{ik}(\underline{p},\underline{q})\right]d\Gamma(\underline{q}) \tag{2.42}$$

turns into

$$C_{ij}(x')u_j(x') + \sum_{n=1}^{N_e}\int_{S_n} T_{ij}(x',x)u_j(x)dS = \sum_{n=1}^{N_e}\int_{S_n} U_{ij}(x',x)t_j(x)dS \tag{3.1}$$

where $S = \sum_{n=1}^{N} S_n$

In the second step, the boundary element the global coordinates (x_1 , x_2), the displacement filed $u_j(x)$ and traction field $t_j(x)$ are approximated by the interpolation

$$\begin{aligned} x_j &= \sum_{\alpha=1}^{m} N_\alpha(\eta)x_j^\alpha \\ u_j &= \sum_{\alpha=1}^{m} N_\alpha(\eta)u_j^\alpha \\ t_j &= \sum_{\alpha=1}^{m} N_\alpha(\eta)t_j^\alpha \end{aligned} \tag{3.2}$$

N_α are the shape functions that are polynomials of degree m-1, and have the property that $N_\alpha = 1$ at node α and $N_\alpha = 0$ at all the other nodes. x_j^α, u_j^α and t_j^α are the nodal values of the quantities at node α. These shape functions are defined in term of non-dimensional coordinates η $(-1 \le \eta \le 1)$.

$$N_\alpha(\eta) = \prod_{i=0, i\neq\alpha}^{m} \frac{\eta - \eta_i}{\eta_\alpha - \eta_i} \tag{3.3}$$

For linear elements m=2,

$$N_1 = \frac{1}{2}(1-\eta) \qquad N_2 = \frac{1}{2}(1+\eta) \tag{3.4}$$

For quadratic elements m=3.

$$N_1 = \frac{1}{2}\eta(\eta-1) \quad N_2 = 1-\eta^2 \quad N_3 = \frac{1}{2}\eta(1+\eta) \tag{3.5}$$

When the same shape functions are used for approximation of both geometry and functions, the formulation is referred to as isoparametric.[6]

A discretized boundary element formulation can be obtained by substituting eqs. (3.2) into integral eqs. (3.1)

$$C_{ij}(x')u_j(x') + \sum_{n=1}^{N_e}\sum_{\alpha=1}^{m} P_{ij}^{n\alpha} u_j^{n\alpha} = \sum_{n=1}^{N_e}\sum_{\alpha=1}^{m} Q_{ij}^{n\alpha} t_j^{n\alpha} \quad i,j = 1,2 \tag{3.6}$$

where

$$\begin{aligned} P_{ij}^{n\alpha} &= \int_{-1}^{1} N_\alpha(\eta) T_{ij}[x', x(\eta)] J^n(\eta) d\eta \\ Q_{ij}^{n\alpha} &= \int_{-1}^{1} N_\alpha(\eta) U_{ij}[x', x(\eta)] J^n(\eta) d\eta \end{aligned} \tag{3.7}$$

and $dS_n(x)$ becomes $J^n(\eta)d\eta$.

In general, $J(\eta)$, the Jacobean of transformation, is given by

$$J(\eta)=\sqrt{\left(\frac{dx_1}{d\eta}\right)^2+\left(\frac{dx_2}{d\eta}\right)^2} \tag{3.8}$$

and

$$J^n(\eta)=\sqrt{\left(\sum_{\alpha=1}^{m}\frac{dN_\alpha}{d\eta}x_1^{n\alpha}\right)^2+\left(\sum_{\alpha=1}^{m}\frac{dN_\alpha}{d\eta}x_2^{n\alpha}\right)^2} \tag{3.9}$$

3.3 Gauss Quadrature Integration

To evaluate the integral in eqs. (3.7), Gauss quadrature[7-10] is employed. For an integral $I=\int_a^b f(x)dx$ a variable transformation is introduced as

$x=c+mt$, where $c=\frac{1}{2}(b+a)$ and $m=\frac{1}{2}(b-a)$. (3.10)

The integral becomes

$$I=m\int_{-1}^{1} f(c+mt)dt=m\sum_{i=1}^{n} w_i f(c+mt_i) \tag{3.11}$$

where w_i is the Gauss weight and t_i is the Gauss point's abscissa .

The following table lists the abscissas and weights for Gauss quadrature of various orders. For Gauss order larger than 10, the FORTRAN code supplied in [11] has been used.

n	*t*	*w*
2	(+/-)0.57735027	1.0
3	0.0 (+/-)0.77459667	0.88888889 0.55555555
4	(+/-)0.33998104 (+/-)0.86113631	0.65214515 0.34785485
5	0.0 (+/-)0.53846931 (+/-)0.90617985	0.56888889 0.47862867 0.23692689
6	(+/-)0.23861919 (+/-)0.66120939 (+/-)0.93246951	0.46791393 0.36076157 0.17132449
7	0.0 (+/-)0.40584515 (+/-)0.74153119 (+/-)0.94910791	0.41795918 0.38183005 0.27970539 0.12948497
8	(+/-)0.18343464 (+/-)0.52553241 (+/-)0.79666648 (+/-)0.96028986	0.36268378 0.31370665 0.22238103 0.10122854
9	0.0 (+/-)0.32425342 (+/-)0.61337143 (+/-)0.83603111 (+/-)0.96816024	0.33023936 0.31234708 0.26061070 0.18064816 0.08127439
10	(+/-)0.14887434 (+/-)0.43339539 (+/-)0.67940957 (+/-)0.86506337 (+/-)0.97390653	0.29552422 0.26926672 0.21908636 0.14945135 0.06667134

Table 3.1 Gauss abscissas and weights

3.4 Collocation and Assembly of Matrix

In the point collocation method, eqs. (3.6) is written for each node on the boundary $\{x^c;\ c=1,M\}$ to yield

$$C_{ij}\left(x^c\right)u_j\left(x^c\right)+\sum_{n=1}^{N_e}\sum_{\alpha=1}^{m}P_{ij}^{n\alpha}\left(x^c\right)u_j^{n\alpha}=\sum_{n=1}^{N_e}\sum_{\alpha=1}^{m}Q_{ij}^{n\alpha}\left(x^c\right)t_j^{n\alpha}\quad c=1,M \tag{3.12}$$

where M is the total number of nodes.

The collocation eqs. (3.12) can be written in matrix notation as

$$C_{ij}\left(x^c\right)u_j\left(x^c\right)+\sum_{\gamma=1}^{M}\overline{H}_{ij}^{c\gamma}u_j^{\gamma}=\sum_{\gamma=1}^{M}G_{ij}^{c\gamma}t_j^{\gamma}\ ,\ c=1,M \tag{3.13}$$

The left-hand-side of eq. (3.13) is condensed to obtain

$$\sum_{\gamma=1}^{M}H_{ij}^{c\gamma}u_j^{\gamma}=\sum_{\gamma=1}^{M}G_{ij}^{c\gamma}t_j^{\gamma} \tag{3.14}$$

where $H_{ij}^{c\gamma}=C_{ij}(x^c)\delta_{c\gamma}+\overline{H}_{ij}^{c\gamma}$ and $\delta_{c\gamma}$ is the Kronecker delta function. The discretized boundary element equations may now be rewritten in matrix forms as[12, 13]

$$Hu=Gt \tag{3.15}$$

where H and G are both *2M by2M* matrices containing known integral of the product of the shape functions, the Jacobian, and the fundamental solutions of U_{ij} and T_{ij}. The vector u and t both have M components, and contains unknown and prescribed boundary conditions.

The diagonal terms in H equal $C_{ij}(x^c)$ and are determined by a special treatment without doing any Gauss quadrature integration. By using eq. (2.41), one can show

$$C_{ij}\left(x^c\right)=-\sum_{\gamma=1}^{M}\overline{H}_{ij}^{c\gamma} \tag{3.16}$$

Also, eqs. (3.16) can be rewritten as

$$C_{ij}\left(x^c\right)u_j + \overline{H}_{ij}^{cc} = -\sum_{\gamma=1,c\neq\gamma}^{M} \overline{H}_{ij}^{c\gamma} \tag{3.17}$$

Hence, the diagonal terms in $H_{ij}^{c\gamma}$ can be evaluated without any integration as

$$H_{ij}^{cc} = -\sum_{\gamma=1,c\neq\gamma}^{M} \overline{H}_{ij}^{c\gamma} \tag{3.18}$$

After inserting the boundary conditions and re-arranging the eq. (3.15) becomes

$$[A]\{X\} = [B]\{Y\} = \{F\} \tag{3.19}$$

The vector *X* contains all the unknown displacements and tractions; vector *Y* contains the prescribed boundary conditions. Matrices *A* and *B* are non symmetric and fully populated.

3.5 Discontinuity at Corners and Boundary Conditions

While applying the boundary conditions, special care has to be taken at points of discontinuities. The discontinuity can occur due to two reasons – at corner nodes where the normal to the boundary abruptly changes direction, and on smooth boundary where the boundary condition changes type. The change in boundary condition can again be of two kinds—displacement boundary condition changing to traction boundary condition or where the traction itself has a jump discontinuity. The discontinuous boundary conditions are schematically shown in Figure 3.2.

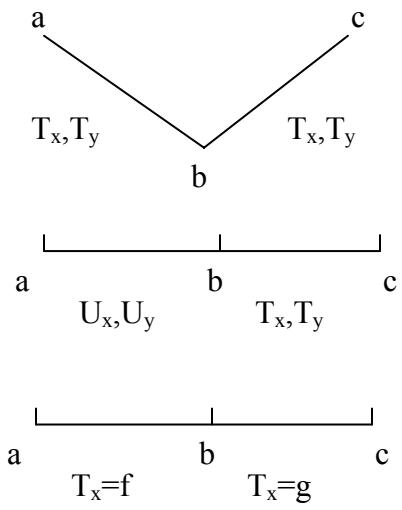

Figure 3.2: Examples of corner nodes and discontinuous boundary condition.

The discontinuity in the boundary condition causes a shortage of equations. In other words, there are more than one unknown at that node, but only one equation is available.

The scheme to solve this problem is to generate additional equations[14, 15]. The additional equations can be derived from other laws[5], theorem, differentiations and finite differencing. There is also the method of adding collocation point outside the region,[16, 17] but the condition number for the coefficient matrix is always very large and this affects the accuracy.

The method[18] used here derives the extra equations from within the framework of the collocation. Double functional nodes are introduced at the same geometric location. That is at the junction of the two elements where the discontinuity is present.

The two elements meeting at the discontinuity are denoted by ‘+’ and ‘-‘. The ‘-‘ element is right before the discontinuity and the ‘+’ element is right after the discontinuity.

Among the double functional nodes, one belongs to the ‘-‘ element and the other belongs to the ‘+’ element. The collocation scheme employed at the ‘-‘ and the ‘+’ nodes depends on the nature of the boundary condition specified on the ‘-‘ and ‘+’ elements.

Four variables, two displacements and two tractions, are associated with each node. Thus, eight variables are associated with the double functional node. Out of these eight variables, four variables are prescribed as boundary conditions. Thus, one needs four equations to obtain the four unknowns at the double functional node. The scheme for obtaining these four equations is shown in Table 3.2.

		BC on +					
		T_x,T_y	T_x,U_x	T_x,U_y	T_y,U_x	T_y,U_y	U_x,U_y
BC On –	T_x,T_y	Fc-(x,y) F±(x) F±(y)	Fc-(x,y) F+(x) F±(y)	Fc-(x,y) F±(x) F+(y)	Fc-(x,y) F+(x) F±(y)	Fc-(x,y) F±(x) F+(y)	Fc-(x,y) F+(x) F+(y)
	T_x,U_x	Fc-(x,y) F-(x) F±(y)	Fc-(x,y) Fc+(x) F±(y)	Fc-(x,y) F-(x) F+(y)	Fc-(x,y) Fc+(x) F±(y)	Fc-(x,y) F-(x) F+(y)	Fc-(x,y) Fc+(x) F±(y)
	T_x,U_y	Fc-(x,y) F±(x) F-(y)	Fc-(x,y) F+(x) F-(y)	Fc-(x,y) F±(x) Fc+(y)	Fc-(x,y) F+(x) F-(y)	Fc-(x,y) F±(x) Fc+(y)	Fc-(x,y) F+(x) Fc+(y)
	T_y,U_x	Fc-(x,y) F-(x) F±(y)	Fc-(x,y) Fc+(x) F±(y)	Fc-(x,y) F-(x) F+(y)	Fc-(x,y) Fc+(x) F±(y)	Fc-(x,y) F-(x) F+(y)	Fc-(x,y) Fc+(x) F±(y)
	T_y,U_y	Fc-(x,y) F±(x) F-(y)	Fc-(x,y) F+(x) F-(y)	Fc-(x,y) F±(x) Fc+(y)	Fc-(x,y) F+(x) F-(y)	Fc-(x,y) F±(x) Fc+(y)	Fc-(x,y) F+(x) Fc+(y)
	U_x,U_y	Fc-(x,y) F-(x) F-(y)	Fc-(x,y) Fc+(x) F-(y)	Fc-(x,y) F-(x), Fc+(y)	Fc-(x,y) Fc+(x) F-(y)	Fc-(x,y) F-(x) Fc+(y)	Fc-(x,y) Fc+(x,y)

Notes:

Fc+(I,j): Collocation at an off-functional node on + (the next element).
Fc- (I,j): Collocation at the functional node on – (the previous element).
3- (i): Use $U^+=U^-$, where U^- is known.
F+ (i): Use $U^-=U^+$, where U^+ is known.
F± (i): Use $U^- - U^+ =0$ where U^- and U^+ both are unknown.

Table 3.2: Collocation scheme for discontinuity

3.6 Examples and BEM Results

To test the BEM code, a pure shear anisotropy model is chosen as an example. The pure shear model is chosen for its importance in the study of dislocation dynamics.

The unit square one zone model is shown in Figure 3.3. The boundary conditions are assigned as pure shear on all sides of the square and the point on the left bottom corner is pinned. Each side of the model is discretized into 4 elements with 5 nodes per side. At the four corners, double nodes are used at the same geometry point, but the double nodes are assigned to the two different sides of the corner. On each boundary element, eight Gauss point are taken to evaluate the boundary integrals on each element.

For isotropic case, the Poisson's ratio and Young's modules are set to be .3 and 1. The anisotropy is defined by the ratio of *E1* and *E2* where *E1* is the Young's modules on the *x* direction and *E2* is the Young's modules on the *y* direction. For the anisotropic case, *E1* is set to 1, and various values of *E2* are chosen. The Poisson's ratio is 0.3 for all anisotropic cases. Shear modulus is determined by *E1*, *E2* and the Poisson's ratio. The coefficients of mutual influence of the first and second kind are all set to zero. All the examples are modeled as plane strain problems.

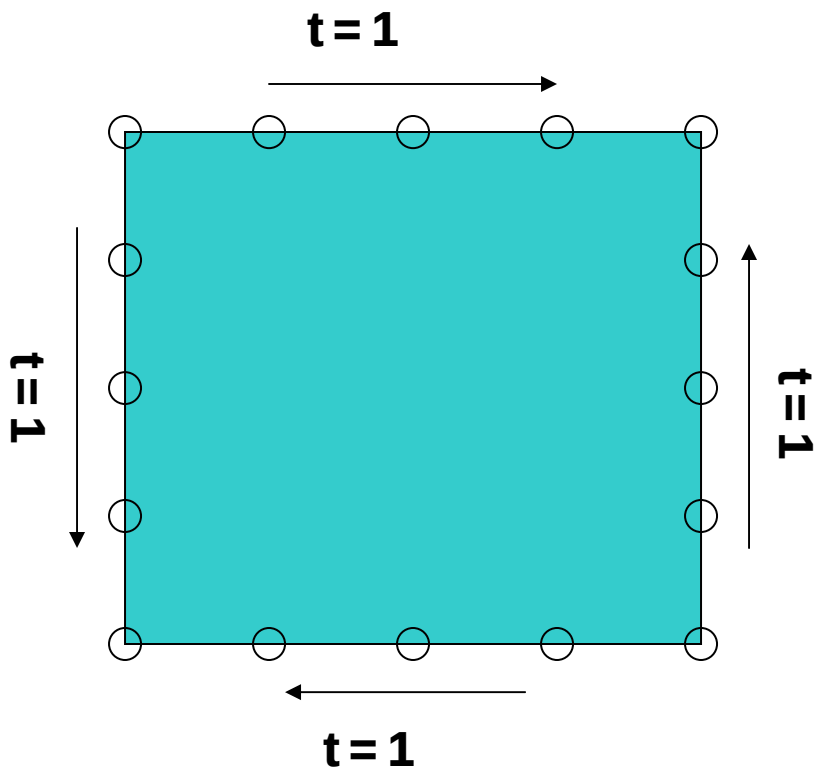

Notes:

5 nodes on every side and 8 Gauss points on every element

Plane strain problem

Boundary Conditions:

Top side: $t_x=1$, $t_y=0$

Bottom side: $t_x=-1$, $t_y=0$

Left side: $t_x=0$ $t_y=-1$

Right side: $t_x=0$ $t_y=1$

Left bottom corner: u_x and u_y pinned.

Figure 3.3 Unit Square one zone pure shear model

With different anisotropy ratios, the interior shear stress distribution is calculated by using the BEM code and is compared with the theoretical solution. The error in the BEM result is shown in percentage of the shear stress. The results of the error distributions are displayed in Figure 3.4 thru Figure 3.14 for different anisotropy ratios: 5, 4, 3, 2.5, 2, 1, 0.5, 0.4, 0.33, 0.25, and 0.2.

The figures for different anisotropy ratios show one common feature: the internal shear stresses calculated by BME code with five nodes pre side and eight Gauss points per element is only accurate when the interior position is one element length away from the boundary of the domain.

The high error near the boundary can be explained by the singularity terms in the fundamental solutions and inaccuracies introduced through Gauss quadrature.

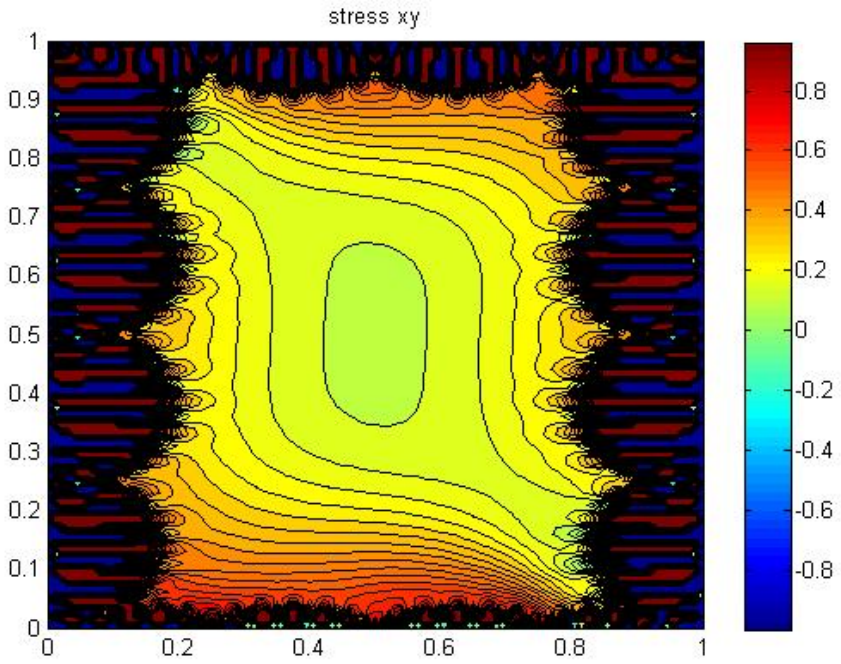

Figure 3.4 Interior shear stress error percentage distributions for anisotropy ratio 5

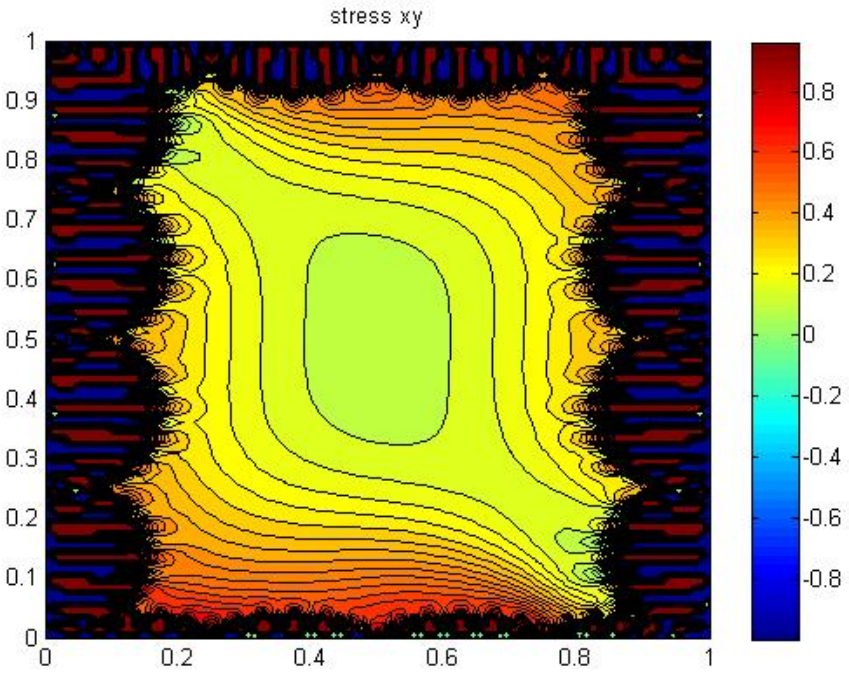

Figure 3.5 Interior shear stress error percentage distributions for anisotropy ratio 4

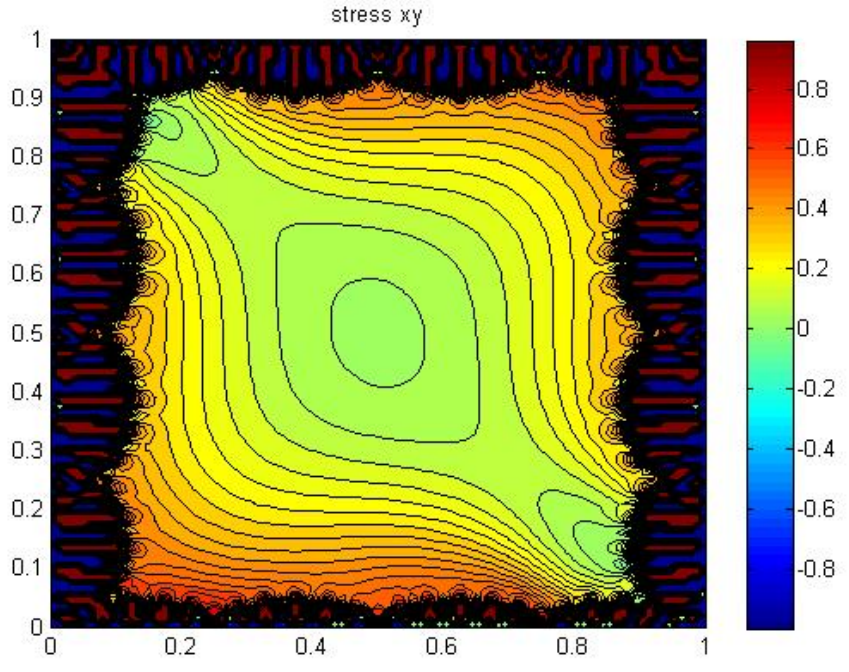

Figure 3.6 Interior shear stress error percentage distributions for anisotropy ratio 3

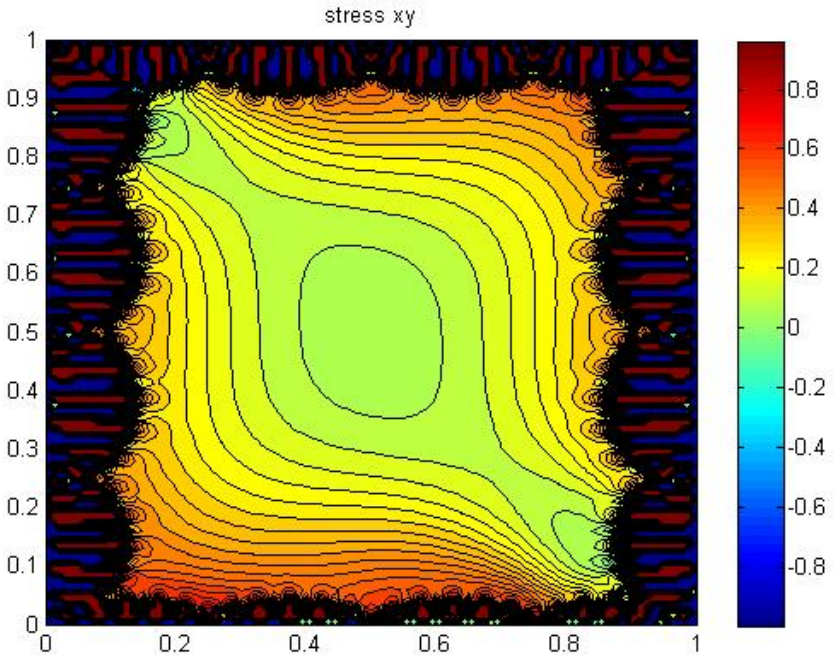

Figure 3.7 Interior shear stress error percentage distributions for anisotropy ratio 2.5

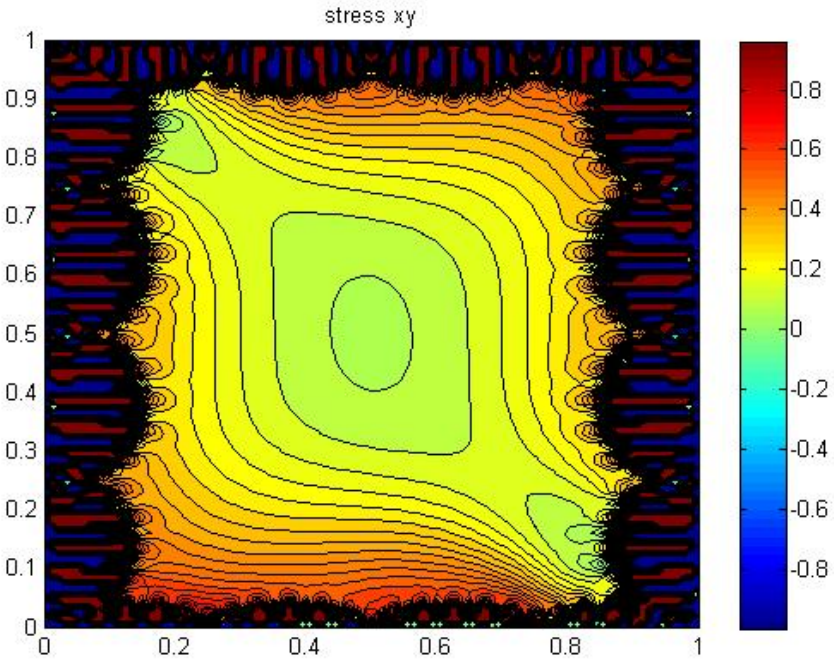

Figure 3.8 Interior shear stress error percentage distributions for anisotropy ratio 2

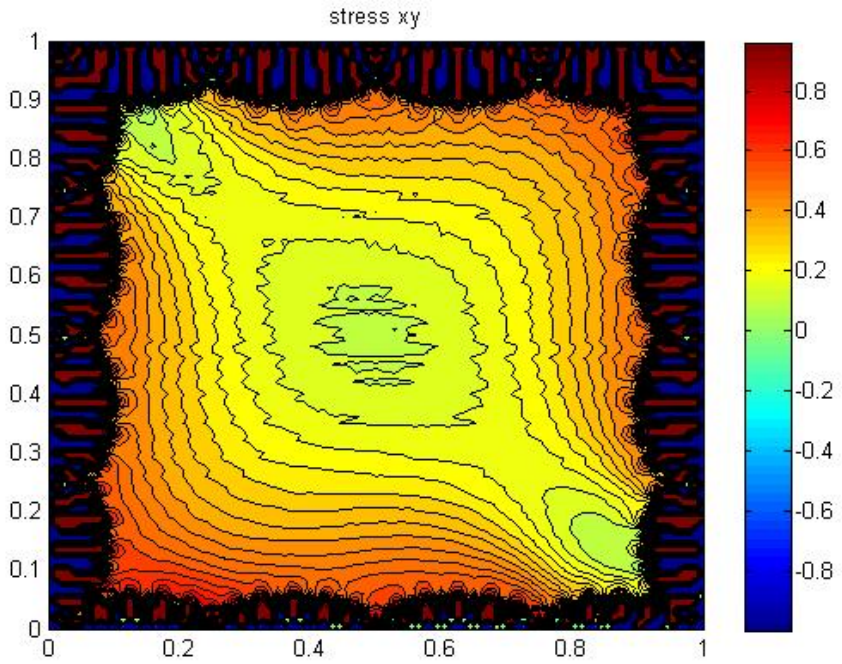

Figure 3.9 Interior shear stress error percentage distributions for anisotropy ratio 1

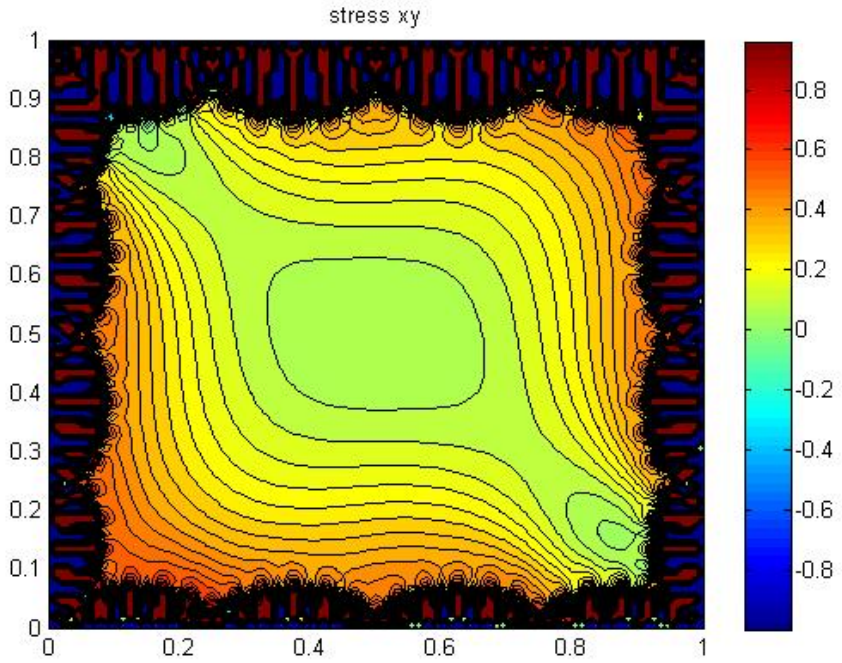

Figure 3.10 Interior shear stress error percentage distributions for anisotropy ratio 0.5

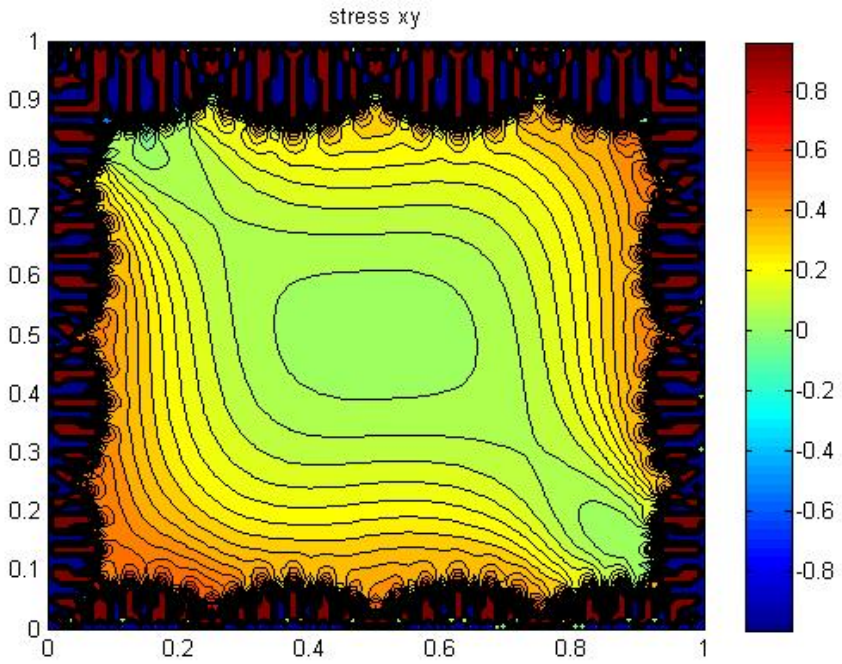

Figure 3.11 Interior shear stress error percentage distributions for anisotropy ratio 0.4

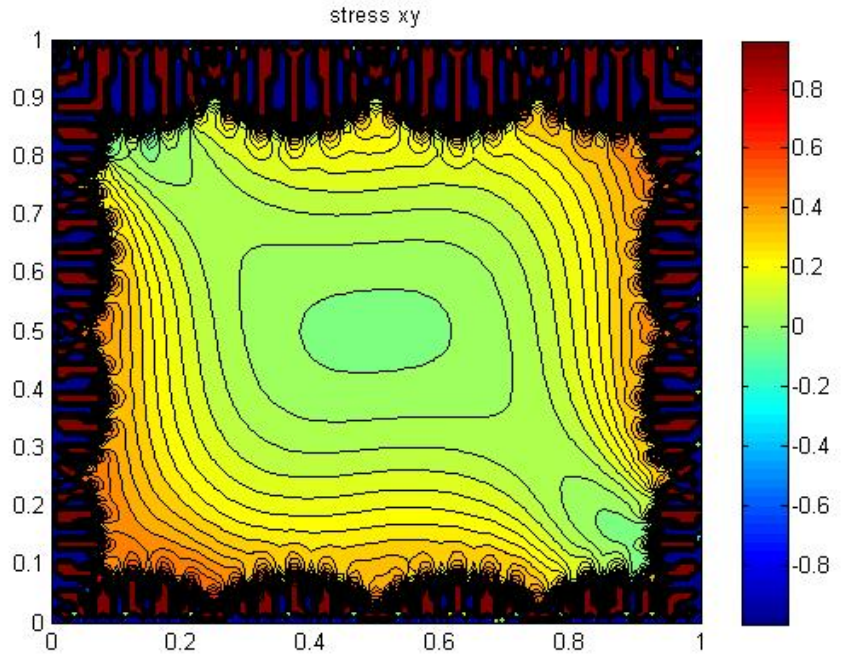

Figure 3.12 Interior shear stress error percentage distributions for anisotropy ratio 0.33

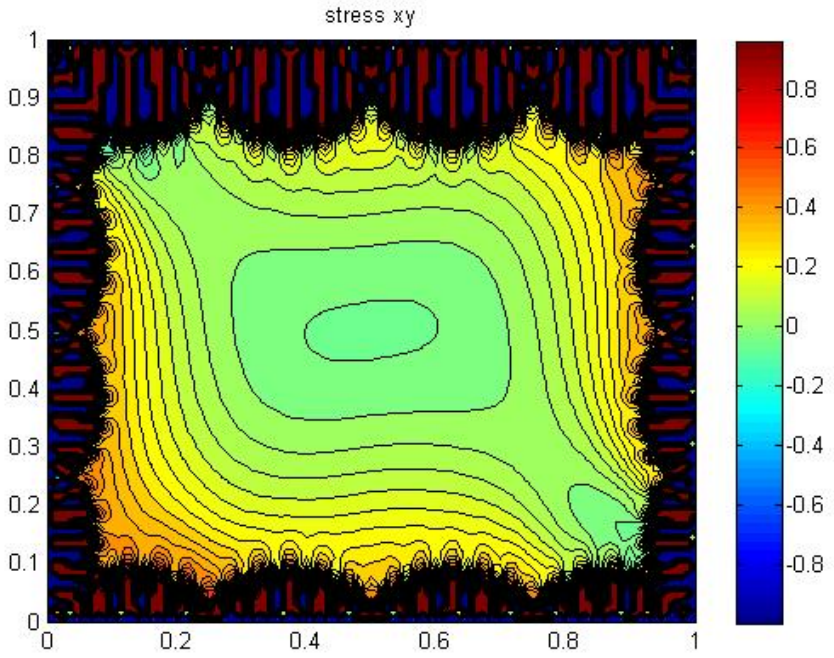

Figure 3.13 Interior shear stress error percentage distributions for anisotropy ratio 0.25

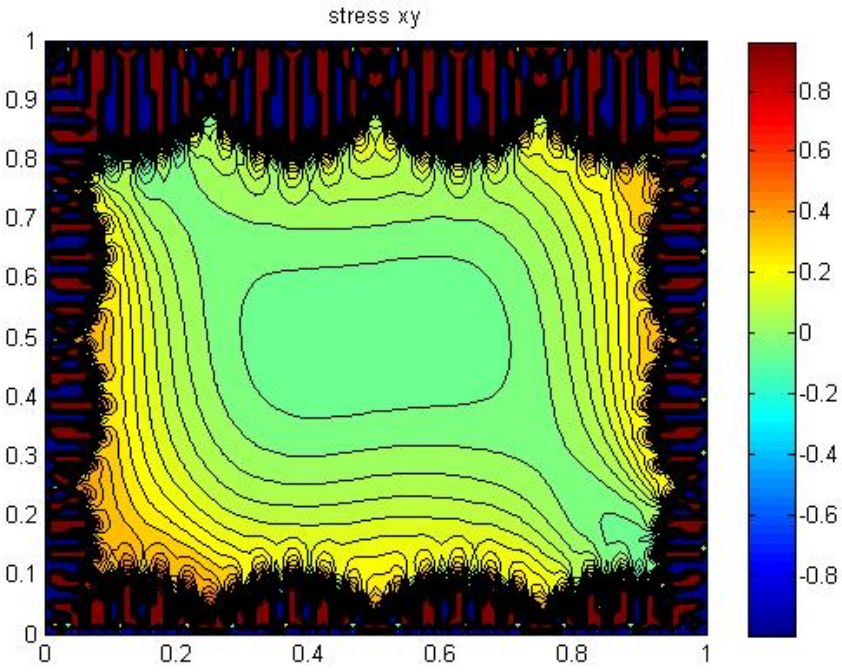

Figure 3.14 Interior shear stress error percentage distributions for anisotropy ratio 0.2

For the dislocation dynamics calculations, the dislocations move along slip lines and finally pile up on the slip line near the boundary. To simulate this effect, the dislocations are pinned when they are within a cutoff distance from the boundary. For a good simulation, this cutoff distance has to be small. Therefore, one needs accurate stress calculation very close to the boundary. To improve the accuracy of stress values near the boundary more Gauss points are.

The effect of increasing Gauss points is shown in Figure 3.15 to Figure 3.18. There are five collocation nodes per side and the results are shown for an anisotropy ratio of 0.2. In five test cases, numbers of Gauss points per element are taken as 8, 16, 32, 48, and 64. The results show that the accuracy in shear stress improves with increased Gauss points.

The major advantage of this approach is that no re-meshing is needed to improve the accuracy. Only care one has to take is – the number of Gauss points has to be increased when the stress values close to the boundary are needed.

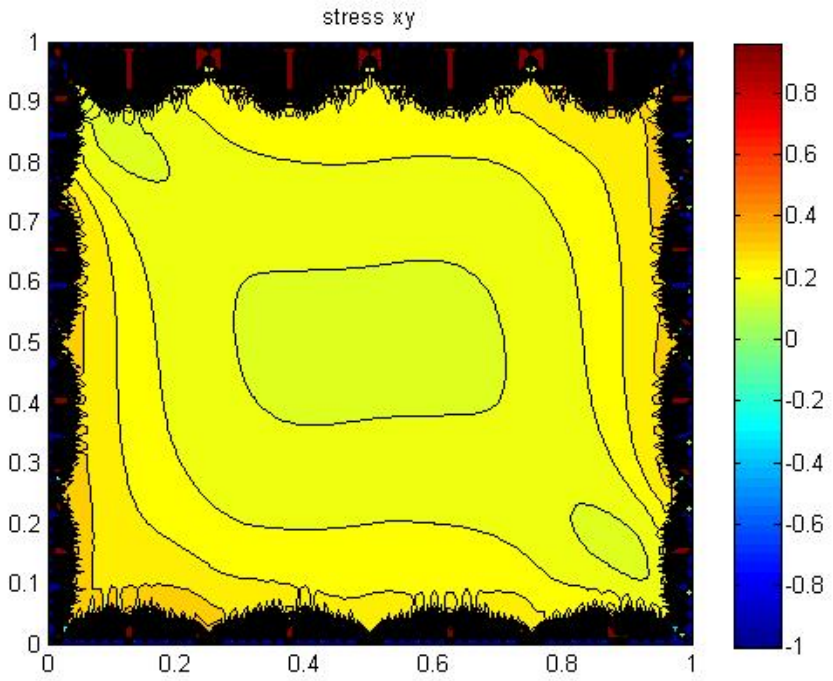

Figure 3.15 Interior shear stress error distributions for 16 Gauss points per element

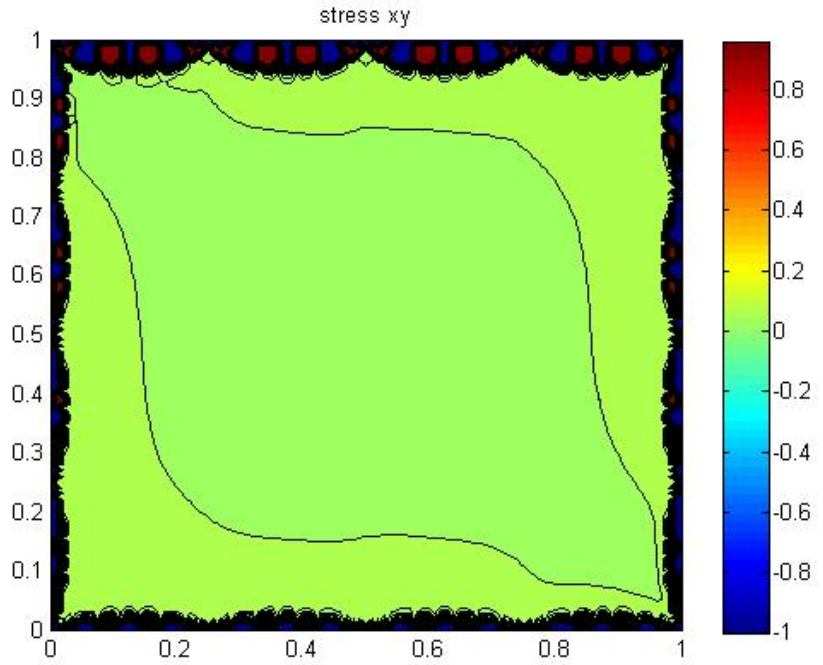

Figure 3.16 Interior shear stress error distributions for 32 Gauss points per element

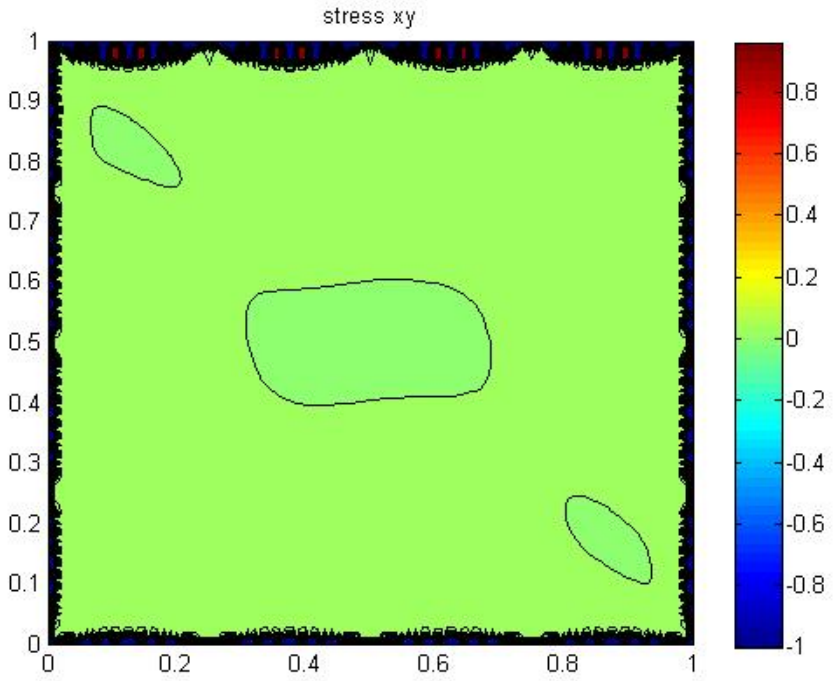

Figure 3.17 Interior shear stress error distributions for 48 Gauss points per element

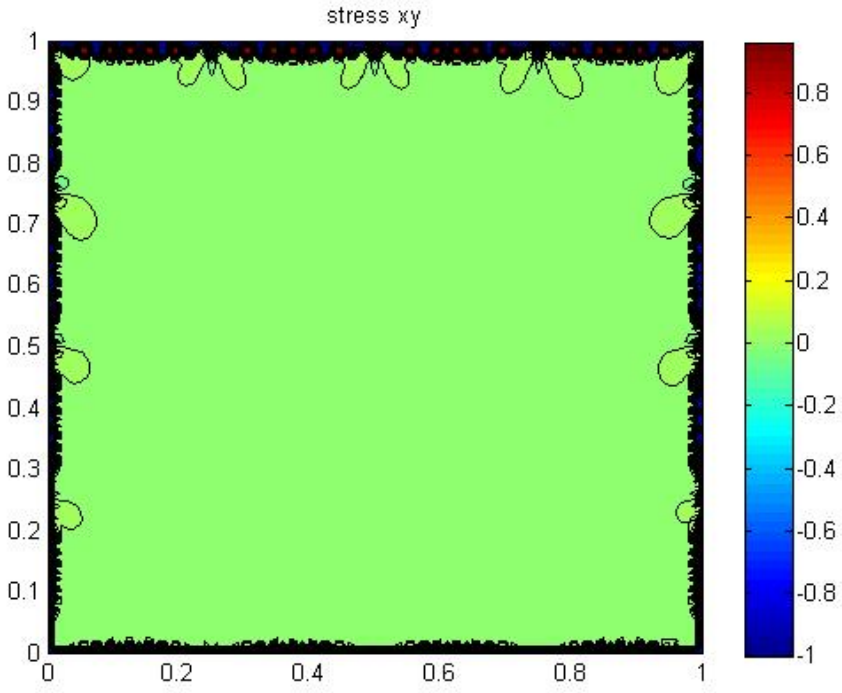

Figure 3.18 Interior shear stress error distributions for 64 Gauss points per element

The disadvantage of only increasing the number Gauss points is that the accuracy is limited by the information contained in the interpolating polynomials. The second approach is to add more collocation nodes but keep the Gauss points per element the same. The results are shown from Figure 3.19 to Figure 3.22. The collocation nodes are increased from 5 nodes per side to 10, 20, 30, and 40 nodes per side. The second approach not only provides an improved internal stress values, but also provides more accurate information on the boundary. For the multi zone grain sliding problems, the sliding depends on boundary tractions. Therefore, better description on the boundary will be essential to generate an accurate sliding model.

The disadvantage of adding boundary nodes is that re-meshing and re-modeling of the domain is required and also increases the size of the system of equation and consequently increases the computing time.

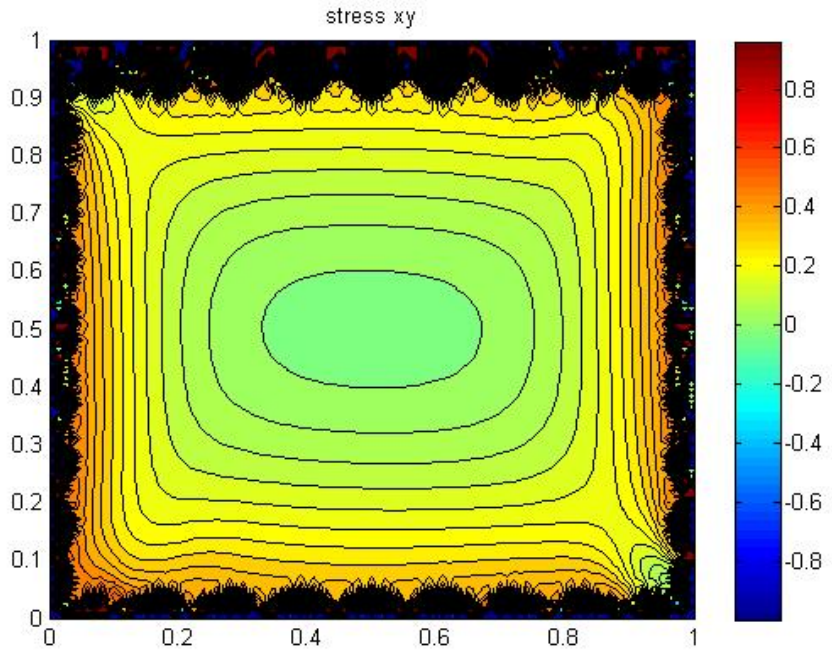

Figure 3.19 Interior shear stress error distributions for 10 collocation nodes per side

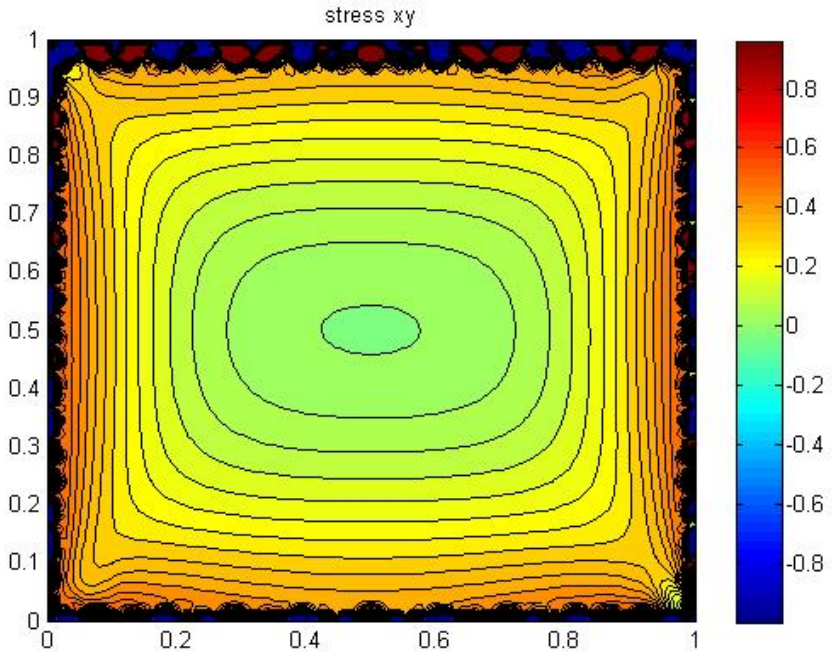

Figure 3.20 Interior shear stress error distributions for 20 collocation nodes per side

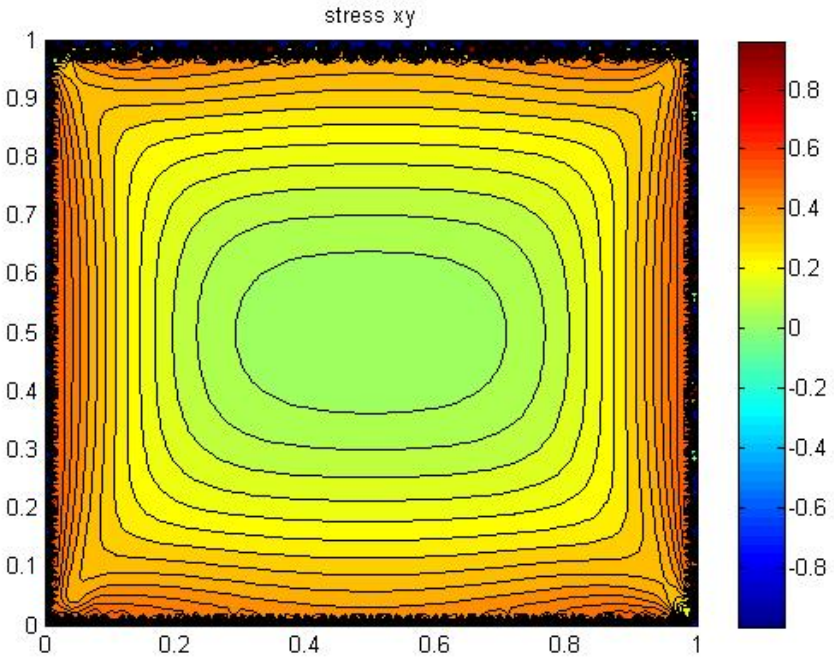

Figure 3.21 Interior shear stress error distributions for 30 collocation nodes per side

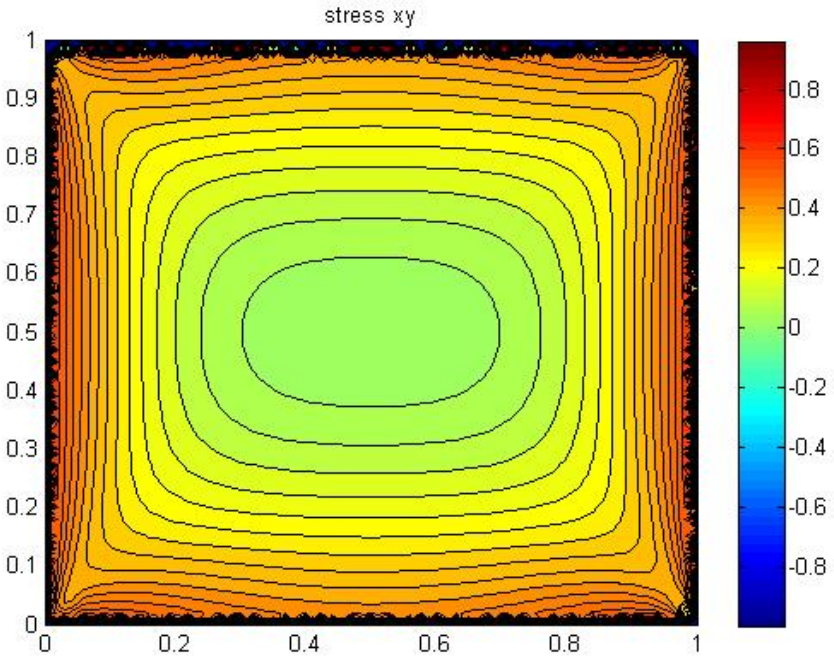

Figure 3.22 Interior shear stress error distributions for 40 collocation nodes per side

3.7 Multi Zone Formulation and Sliding

For multi-zone problems, the BEM model leads to block banded matrix systems with one block for each zone and overlaps between blocks where the zones have a common interface.

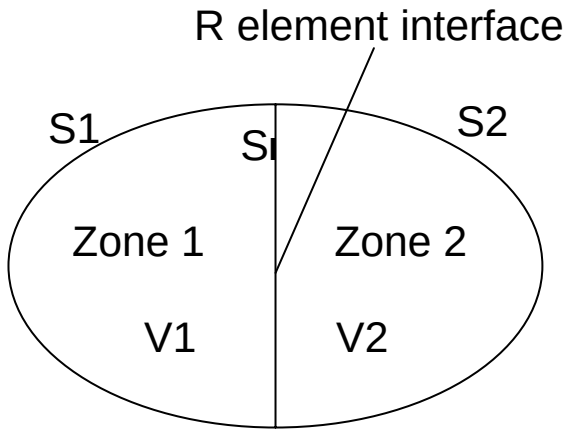

Figure 3.23 Multi zone assemble demonstration

Consider the example in Figure 3.23 with two zones V_1 and V_2, and two outer boundaries S_1 and S_2, and one interface S_I. On zone V_1, U^1 and T^1 are displacements and tractions at the external boundary S_1, U^1_I and T^1_I are displacements and tractions at the interface S^1. Similarly, on V_2, U^2 and T^2 are displacements and tractions at the external boundary S^2, U^2_I and T^2_I are displacements and tractions at the interface S^1.

The system of equations for V^1 and V^2 can be written as

$$\begin{bmatrix} H^1 & H^1_I \end{bmatrix} \begin{Bmatrix} U^1 \\ U^1_I \end{Bmatrix} = \begin{bmatrix} G^1 & G^1_I \end{bmatrix} \begin{Bmatrix} T^1 \\ T^1_I \end{Bmatrix} \tag{3.20}$$

$$\begin{bmatrix} H^2 & H_I^2 \end{bmatrix} \begin{Bmatrix} U^2 \\ U_I^2 \end{Bmatrix} = \begin{bmatrix} G^2 & G_I^2 \end{bmatrix} \begin{Bmatrix} T^2 \\ T_I^2 \end{Bmatrix} \tag{3.21}$$

The compatibility and equilibrium conditions at the interface S_I are

$$U_I^1 = +U_I^2 \equiv U_I \tag{3.22}$$

$$T_I^1 = -T_I^2 \equiv T_I \tag{3.23}$$

The complete system of equations is now assembled as[19]

$$\begin{bmatrix} H^1 & H_I^1 & 0 & 0 \\ 0 & 0 & H^2 & H_I^2 \\ 0 & 1 & 0 & -1 \\ 0 & 0 & 0 & 0 \end{bmatrix} \begin{Bmatrix} U^1 \\ U_I^1 \\ U^2 \\ U_I^2 \end{Bmatrix} = \begin{bmatrix} G^1 & G_I^1 & 0 & 0 \\ 0 & 0 & G^2 & G_I^2 \\ 0 & 0 & 0 & 0 \\ 0 & 1 & 0 & 1 \end{bmatrix} \begin{Bmatrix} T^1 \\ T_I^1 \\ T^2 \\ T_I^2 \end{Bmatrix} \tag{3.25}$$

Combining all the interface terms into U_I and T_I and rearranging them to the left-hand-side, eqs. (3.25) turn to[20]

$$\begin{bmatrix} H^1 & H_I^1 & -G_I^1 & 0 \\ 0 & H_I^2 & -G_I^2 & H^2 \end{bmatrix} \begin{Bmatrix} U^1 \\ U_I \\ T_I \\ U^2 \end{Bmatrix} = \begin{bmatrix} G^1 & 0 \\ 0 & G^2 \end{bmatrix} \begin{Bmatrix} T^1 \\ T^2 \end{Bmatrix} \tag{3.26}$$

U^1, U^2, T^1, T^2 in eqs. (3.26) are rearranged depending on whether they are unknown or prescribed external boundary conditions. With the substitution of the prescribed external boundary conditions, the final system of equations can be written as

$$\begin{bmatrix} A^1 & H_I^1 & -G_I^1 & 0 \\ 0 & -H_I^2 & -G_I^2 & A^2 \end{bmatrix} \begin{Bmatrix} X^1 \\ U_I \\ T_I \\ X^2 \end{Bmatrix} = \begin{bmatrix} R^1 & 0 \\ 0 & R^2 \end{bmatrix} \begin{Bmatrix} Y^1 \\ Y^2 \end{Bmatrix} \tag{3.27}$$

where X^1,and X^2 are the unknowns and Y^1 and Y^2 are the prescribed external boundary displacement and traction conditions on region 1 and 2. The coefficient matrices are

block-banded with one block for each region and overlaps between blocks on the common interface.

To implement sliding which will be discussed in the next section, displacement continuity eqs. (3.22) and (3.23) can be replaced by spring equations

$$\begin{aligned} K(U_I^1 - U_I^2) &\equiv T_I^1 \\ K(U_I^2 - U_I^1) &\equiv T_I^2 \end{aligned} \tag{3.28}$$

where the equilibrium still holds and the spring stiffness K allows possible movement between zones.

For a two dimensional spring, shear direction spring stiffness K_S and normal direction spring stiffness K_N are introduced in eqs. (3.28)

$$\begin{aligned} K_S(U_{IS}^1 - U_{IS}^2) &\equiv T_{IS}^1 \\ K_N(U_{IN}^2 - U_{IN}^1) &\equiv T_{IN}^2 \end{aligned} \tag{3.29}$$

where U_S and T_S are the tangential components and U_N and T_N are the normal components.

According to this formulation, the opening between zones depends on the sign and the magnitude of the spring stiffness on that orientation. For continuous displacement at interface, high magnitude of spring stiffness is used for K_S and K_N. In that way the displacement discontinuity calculated from eqs. (3.29) will be very small, and those zones will be tightly connected. When only the K_S is softened, the shear direction displacement discontinuity becomes bigger; while the displacement discontinuity on the normal direction remains small. In this way, shear direction movement can be controlled by the sign and magnitude of K_S, and sliding effects between zones can be simulated. For an extreme case of free sliding, K_S is zero.

When the spring eqs. (3.29) are combined with eqs. (3.20) and (3.21), one obtains[21]

$$\begin{bmatrix} H^1 & H_I^1 & 0 & 0 \\ 0 & 0 & H^2 & H_I^2 \end{bmatrix} \begin{Bmatrix} U^1 \\ U_I^1 \\ U^2 \\ U_I^2 \end{Bmatrix} = \begin{bmatrix} G^1 & G_I^1 & 0 & 0 \\ 0 & 0 & G^2 & G_I^2 \end{bmatrix} \begin{Bmatrix} T^1 \\ T_I^1 \\ T^2 \\ T_I^2 \end{Bmatrix} \tag{3.30}$$

$$\begin{bmatrix} 0 & K & 0 & -K \\ 0 & -K & 0 & K \end{bmatrix} \begin{Bmatrix} U^1 \\ U_I^1 \\ U^2 \\ U_I^2 \end{Bmatrix} = \begin{bmatrix} 0 & 1 & 0 & 0 \\ 0 & 0 & 0 & 1 \end{bmatrix} \begin{Bmatrix} T^1 \\ T_I^1 \\ T^2 \\ T_I^2 \end{Bmatrix} \tag{3.31}$$

To combine eq. (3.30) and (3.31), we multiply both sides of eqs. (3.31) by the coefficient matrix on the right-hand-side of eqs. (3.30)

$$\begin{bmatrix} 0 & KG_I^1 & 0 & -KG_I^1 \\ 0 & -KG_I^2 & 0 & KG_I^2 \end{bmatrix} \begin{Bmatrix} U^1 \\ U_I^1 \\ U^2 \\ U_I^2 \end{Bmatrix} = \begin{bmatrix} 0 & G_I^1 & 0 & 0 \\ 0 & 0 & 0 & G_I^2 \end{bmatrix} \begin{Bmatrix} T^1 \\ T_I^1 \\ T^2 \\ T_I^2 \end{Bmatrix} \tag{3.32}$$

By subtracting eqs. (3.32) from eqs. (3.30), we find the final assembled system as

$$\begin{bmatrix} H^1 & H_I^1 - KG_I^1 & 0 & KG_I^1 \\ 0 & KG_I^2 & H^2 & H_I^2 - KG_I^2 \end{bmatrix} \begin{Bmatrix} U^1 \\ U_I^1 \\ U^2 \\ U_I^2 \end{Bmatrix} = \begin{bmatrix} G^1 & 0 & 0 & 0 \\ 0 & 0 & G^2 & 0 \end{bmatrix} \begin{Bmatrix} T^1 \\ T_I^1 \\ T^2 \\ T_I^2 \end{Bmatrix} \tag{3.33}$$

The unknown T_I cannot be solved from these equations, because the coefficients in the matrix corresponding to T_I are 0. Instead, T_I will be treated as a prescribed boundary condition with $T_I = 0$. Any value assigned for T_I does not affect the final solution of eqs. (3.33). The quantity U_I is determined at the interface and this U_I is inserted into the spring eqs. (3.29) to determine T_I.

3.8 Grain Sliding with BEM Formulation

To study grain boundary sliding, the polycrystal is modeled by hexagonal array (see Figure 3.24) of grains[22-28]. Due to periodic boundary condition, it suffices to consider only two trapezoidal fractions OABC and EBAD of the cell structures (Figure 3.25). The grain boundary is modeled as a viscous sliding interface with zero thickness. This is appropriate, because grain boundaries are usually only a few lattice spacing wide which is negligible compared to the grain dimensions.

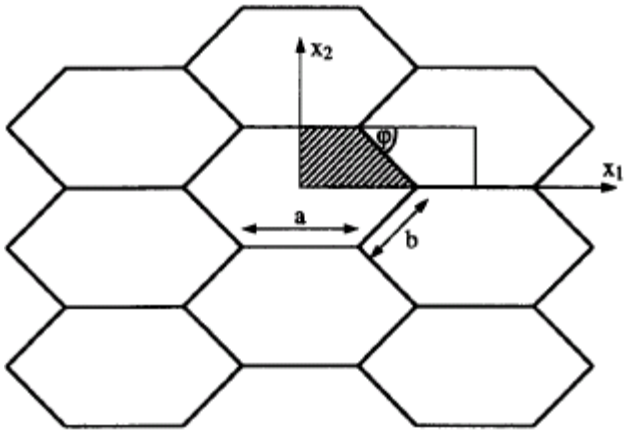

Figure 3.24 Plane hexagonal grain arrangements

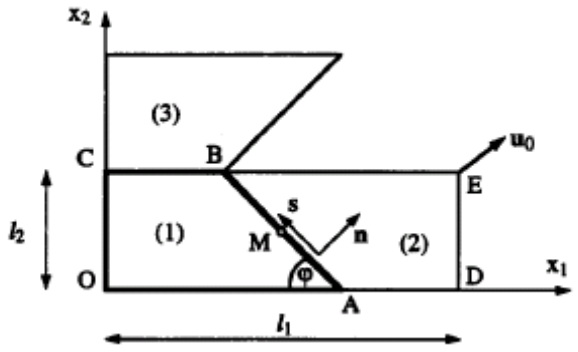

Figure 3.25 Representative cells of the periodic structure

The boundary conditions for the trapezoid OABC under normal strain are specified as follows. The origin *O* is fixed in space while the rectangular faces DE and EC will move with the constant velocities $du_1=e_{11}l_1$ and $du_2=e_{22}l_2$ respectively. This yields the boundary conditions on the outer faces as

OA, AD:	$u_2=0,$	$t_1=0$
OC:	$u_1=0,$	$t_2=0$
BC, BE:	$u_2=e_{22}l_2,$	$t_1=0$
ED:	$u_1=e_{11}l_1,$	$t_2=0$

On interface AB, a non-linear viscous sliding relationship between shear tractions and shear displacements discontinuity is introduced:

$$\Delta u_s = v_0 \Delta t \left(\frac{\left| t_{sa} + \Delta t_s \right|}{s_0} \right)^{1/m} \operatorname{sgn}\left(t_{sa} + \Delta t_s \right) \tag{3.34}$$

where Δt is the time step, V_0 is the reference velocity, S_0 and $0 < m < 1$ are the material parameters, and sgn() is the sign function, t_s is the shear traction along the grain boundary, u_s is the displacements discontinuity at zone interface along the shear

direction of the grain boundary. The subscript $(.)_a$ denotes the variable at the beginning of the time step $t = t_a$.

The value of V_0 is defined as the relative velocity of a viscous grain boundary loaded by a shear strain of amount S_0. The limit $S_0 \rightarrow 0$ corresponds to free sliding $|t_s| = 0$. Equation (3.34) gives time dependant implementation of grain sliding.

The combination of BEM with the time dependant non-linear sliding can be broken into the following steps:

1. At time $t=0$, the spring stiffnesses K_N and K_S are taken as large and t_{sa} is calculated.
2. At the interface AB, the shear spring stiffness K_S is relaxed to its actual value and eq.(3.34) is used to initiate the sliding process. New u_s and t_s are calculated for a given time step Δt.
3. Step 2 is repeated to update u_s and t_s for the next time step.

The result for the two zone model is shown in Figure 3.26. The macroscopic stress is the average of all the nodal values of t_1 along the left side of the model. The result shows the change of the t_1 with the time. The calculations were performed for various values of m. The parameters V_0 and S_0 are taken as one for this simulation. In this numerical experiment, the BEM model is for isotropic plane strain with Young modulus and Poisson's ratio as 1 and 0.3, respectively.

The curves in Figure 3.26 show the trend of relaxation during sliding. By controlling the value of m, various levels of relaxation can be simulated. When the simulation runs for a sufficiently long time, all the curves approach the same horizontal asymptote. This asymptote represents the fully relaxed level for the sliding model. At that

status, a new equilibrium established. In Figure 3.26, only the curve for *m=1* reach that status. Larger value of *m* results in a faster approach to the asymptote.

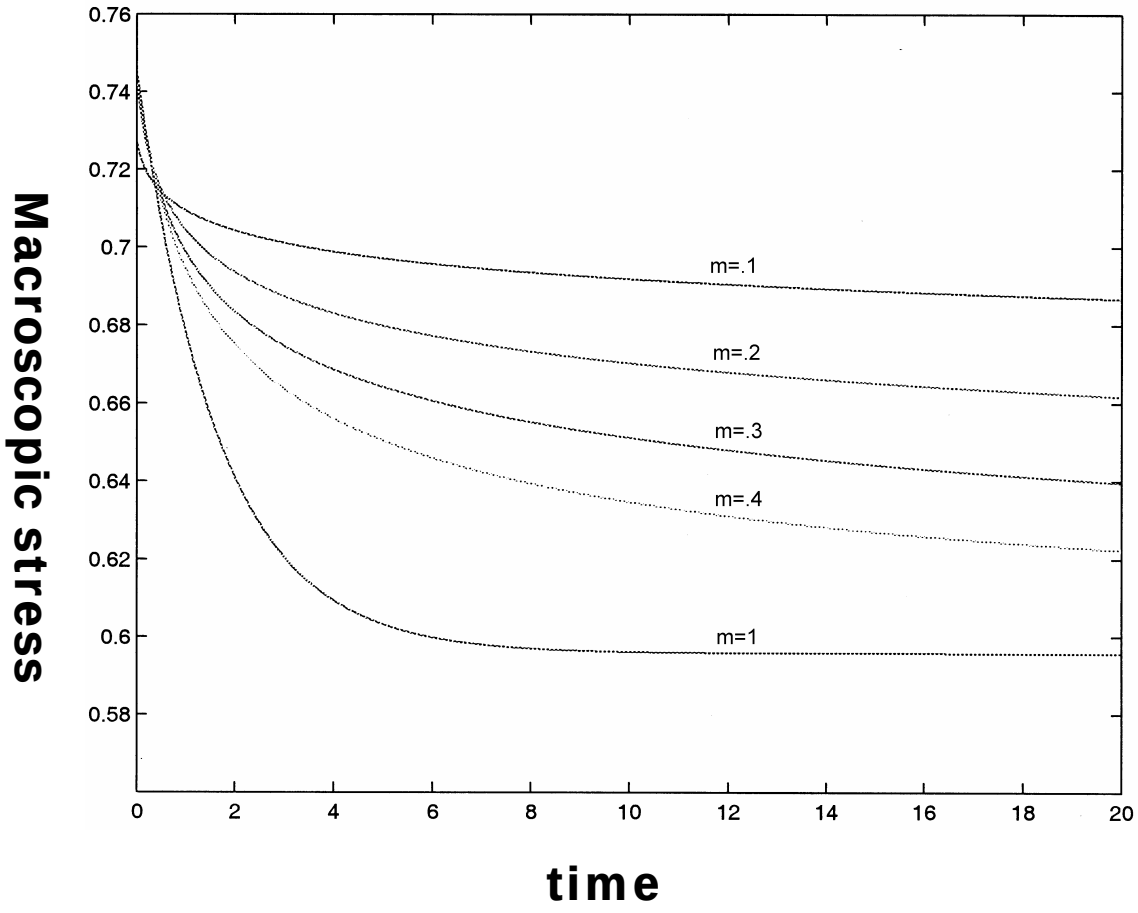

Figure 3.26 Macroscopic stresses for 2 zone sliding with different m

In the two zone model, there is only one interface. To demonstrate that the multi-zone BEM model is implemented correctly for multiple interfaces, variuos zone models are now considered.

The two zone model is only a square piece cutoff from the polycrystal hexagon grains in Figure 3.24. The two zone model is called the 1H model because the size of the

square is set to be 1H. The other multi zone models are squares with size of 2H, 4H, and 8H. All the models with different size are shown in Figure 3.26. They are all squares cutoff from Figure 3.24 and have the same periodical boundary conditions.

As all the models come from the same hexagonal arrangement of grains, the sliding effect should be the same for all models when all the boundary conditions and the values of the sliding parameters are same. The sliding problem does not have any length scale associated with it, therefore the 1H, 2H, 4H, and 8H models represent the same big model and the same grain arrangement.

In Figure 3.27, the sliding of the 1H, 2H, 4H, and 8H models are shown for m=0.4. As expected, we find that the time relaxation curves for all the four models collapse into one curve. From this result, we are confident that the multi-zone BEM and the sliding model are correct.

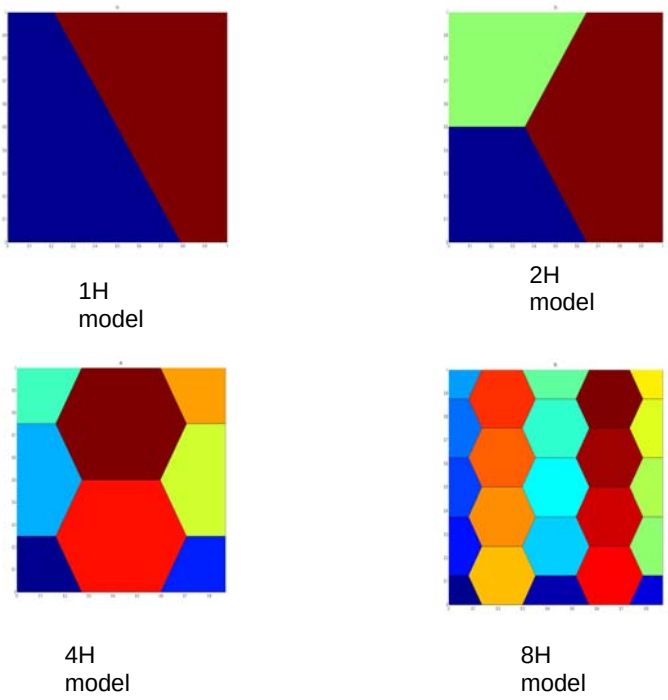

Figure3.26 Different Models for the grain sliding

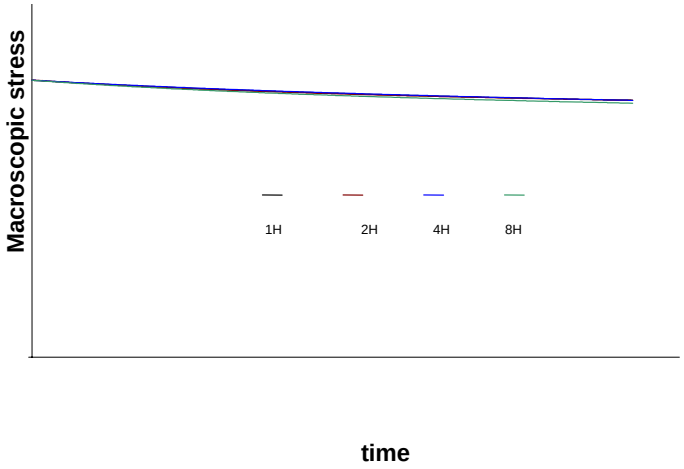

Figure 3.27 Macroscopic stress for m=0.4 with different models

References:

1. Banerjee, P.K. and R. Butterfield, *Boundary Element Methods in Engineering Science*. 1981: London.
2. Aliabadi, M.H., *The boundary element method: Applications in Solids and Structures*. 2002: Wiley.
3. Beer, G., *Programming the Boundary Element Method*. 2000: John Wiley & Sons, Inc. New York, NY, USA.
4. Beer, G. and J.O. Watson, *Introduction to Finite and Boundary Element Methods for Engineers*. 1992: Wiley.
5. Gao, X.W. and T.G. Davies, *Boundary Element Programming in Mechanics*. 2002: Cambridge University Press.
6. Lachat, J.C. and J.O. Watson, *Effective numerical treatment of boundary integral equations: a formulation for three-dimensional elastostatics.* International Journal for Numerical Methods in Engineering, 1976. **10**: p. 991-1005.
7. Stroud, A.H. and D. Secrest, *Gaussian Quadrature Formulas*. 1966: Prentice-Hall.
8. Crow, J.A., *Quadrature of Integrands with a Logarithmic Singularity.* Mathematics of Computation, 1993. **60**(201): p. 297-301.
9. Smith, R.N.L., *Direct Gauss quadrature formulae for logarithmic singularities on isoparametric elements.* Engineering Analysis with Boundary Elements, 2000. **24**(2): p. 161-167.

10. Pham, H.H. and A. Nathan, *Generating Gauss quadratures for Green's function/r: a randomized algorithm*, in *Electrical and Computer Engineering, 1998. IEEE Canadian*. 1998.

11. Press, W.H., et al., *Numerical recipes in Fortran 77: the art of scientific computing*. 2001: Cambridge University Press.

12. Brebbia, C.A., J.C.F. Telles, and L.C. Wrobel, *Boundary element techniques: Theory and applications in engineering*. 1984.

13. Chen, H.B., et al., *An effective method for finding values on and near boundaries in the elastic BEM.* Computers and Structures, 1998. **69**(4): p. 421-431.

14. Mitra, A.K. and M.S. Ingber, *Resolving Difficulties in the BIEM Caused by Geometric Corners and Discontinuous Boundary Conditions*, in *Boundary Elements IX*. 1987.

15. Chati, M.K. and A.K. Mitra, *Prediction of elastic properties of fiber-reinforced unidirectional composites.* Engineering Analysis with Boundary Elements, 1998. **21**(3): p. 235-244.

16. Bonnet, M., *Boundary Integral Equation Methods for Solids and Fluids*. Vol. 34. 1999: Springer. 301-302.

17. Patterson, C. and M. Sheikh, *A. Interelement continuity in boundary element method.* , in *CA Brebbia. Topics in Boundary Element Research Vol.1*. 1984, Berlin: Springer-Verlag.

18. Mitra, A. and M. Ingber, *A multiple-node method to resolve the difficulties in the boundary integral equation method caused by corners and discontinuous*

boundary conditions. International Journal for Numerical Methods in Engineering, 1993. **36**(10): p. 1735-1746.

19. Butterfield, R. and G.R. Tomlin, *Integral techniques for solving zoned anisotropic continuum problems*, in *Proc. International Conference on Variational Methods in Engineering*. 1971. p. 9.

20. Albuquerque, E.L., P. Sollero, and M.H. Aliabadi, *The boundary element method applied to time dependent problems in anisotropic materials*. International Journal of Solids and Structures, 2002. **39**(5): p. 1405-1422.

21. Beer, G., *An efficient numerical method for modelling initiation and propagation of cracks along material interfaces.* International journal for numerical methods in engineering, 1993. **36**(21): p. 3579-3594.

22. Crossman, F.W. and M.F. Ashby, *The Nonuniform Flow of Polycrystals by Grain-Boundary Sliding Accomodated by Power-Law Creep.* Acta Met, 1975. **23**(4): p. 425-440.

23. Ghahremani, F., *Effect of grain boundary sliding on anelasticity of polycrystals.* International Journal of Solids and Structures, 1980. **16**(9): p. 825-845.

24. Ghahremani, F., *Effect of grain boundary sliding on steady creep of polycrystals.* International Journal of Solids and Structures, 1980. **16**(9): p. 847-862.

25. Tvergaard, V., *Influence of grain boundary sliding on material failure in the tertiary creep range.* International Journal of Solids and Structures, 1985. **21**(3): p. 279-293.

26. Tvergaard, V., *Effect of grain boundary sliding on creep constrained diffusive cavitation.* Journal of the Mechanics and Physics of Solids, 1985. **33**(5): p. 447-469.

27. Biner, S.B., *The role of grain boundary sliding and reinforcement morphology on the creep deformation behaviour of discontinuously reinforced composites.* Journal of Materials Science, 1996. **31**(13): p. 3459-3467.

28. Fotiu, P.A., R. Heuer, and F. Ziegler, *BEM analysis of grain boundary sliding in polycrystals.* Engineering Analysis with Boundary Elements, 1995. **15**(4): p. 349-358.

CHAPTER FOUR: DISLOCATION STRESS FIELD CALCULATION AND DISLOCATION DYNAMICS

4.1 Introduction

Why metals could be plastically deformed and why the plastic deformation properties could be changed to a very large degree without changing the chemical composition, the answer to these questions lie in dislocation dynamics. Dislocations can be perceived easily from structural pictures on an atomic scale. They are usually introduced and thought of as extra lattice planes inserted into the crystal that do not extend through all of the crystal, but end on the dislocation line.

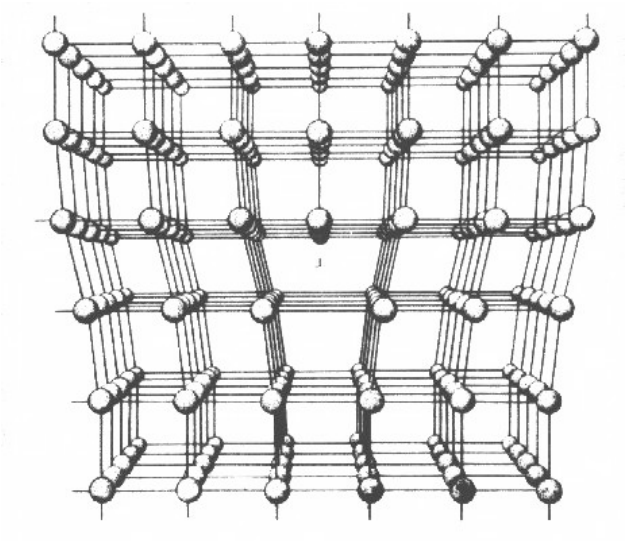

Figure 4.1 3D view of dislocations

However, crystal structure shown in Figure 4.1 does not occur in nature. All real lattices are much more complicated. Edge dislocations are just one extreme form of the possible dislocation structures. Most of the real crystals could be split into "partial" dislocations and become very complicated.

4.1.1 Single Dislocation

The generation and movement of the dislocation can be illustrated in Figure 4.2.1 thru Figure 4.2.3. It also shows the connection between the dislocation movement and the plastic deformation. After a dislocation has completely passed through a crystal, the lattice is completely restored, and no trace of the dislocation is left in that lattice. Parts of the crystal are now shifted in the plane toward the movement of the dislocation. Plastic deformation of metals proceeds by the generation and movement of dislocations through this shifting.

A dislocation is one-dimensional defect because the lattice is only disturbed along the dislocation line. The dislocation line thus can be described at any point by a line vector $t(x,y,z)$. Dislocations move under the influence of external forces which cause internal stresses in a crystal. The area swept by the movement of dislocations defines the glide plane, which always contains the dislocation line vectors. The movement of dislocations shifts the whole crystal from one side of the glide plane toward the other side.

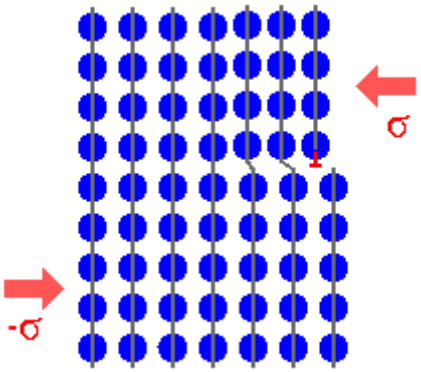

Figure 4.2.1 Generation of an edge dislocation by a shear stress

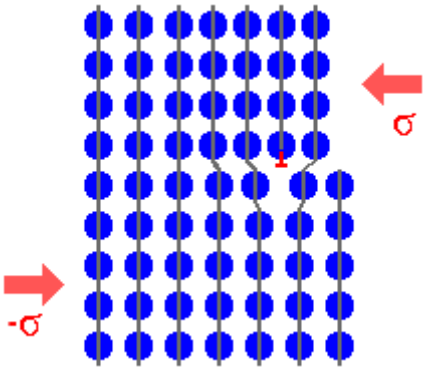

Figure 4.2.2 Movement of the dislocation through the crystal

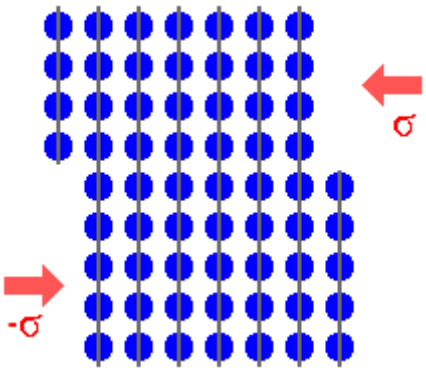

Figure 4.2.3 Shift of the upper half of the crystal after the dislocation emerged

Dislocations move in response to shear stress on the glide plane. When critical shear stress threshold is reached, a dislocation generates and moves. From that moment, the deformation is no longer elastic but plastic, because the dislocation will not move back when the stress is removed.

The example in Figure 4.2.1 is an idealized edge dislocation in a cubic lattice which does not exist in nature. The grey lines show the projection of the lattice planes, the dislocation line in red symbols is perpendicular to the screen and bounds the extra lattice plane.

The dislocation line moves on its glide plane and produces, upon leaving the crystal, an elementary step on the crystal surface. For macroscopic deformation in three dimensions, many dislocations have to move through the crystal. The elementary process shown above has to be repeated literally billions of times on many different planes of the lattice.

4.1.2 Burger's vector and Burger's circuit

The fundamental quantity defining an arbitrary dislocation is its Burgers vector $\underline{b}$. Its atomistic definition follows from a Burgers circuit around the dislocation in the real crystal, which is illustrated in Figure 4.3. On the left of Figure 4.3, one can make a closed circuit that encloses the dislocation from lattice point to lattice point. One could obtain a closed chain of the base vectors which define the lattice. On the right side, one can make exactly the same chain of base vectors in a perfect reference lattice, but the chain can not be closed. The special vector needed for closing the circuit in the reference crystal is by definition the Burgers vector $\underline{b}$.

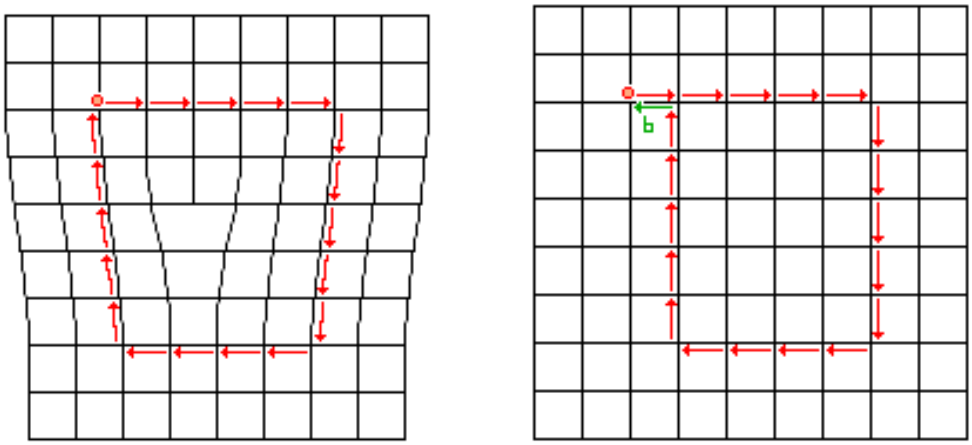

Figure 4.3 Burger's circuit

4.1.3 Screw dislocation and Edge dislocation

There are two basic types of simple dislocations: screw dislocation and edge dislocation. The edge dislocation showed in Figure 4.4 moves along the *x* axis which is perpendicular to the dislocation line along the *z* axis. The Burger's vector for edge dislocation is also perpendicular to the dislocation line. For screw dislocation, the Burger's vector is along the direction of dislocation line and the dislocation moves along that direction.

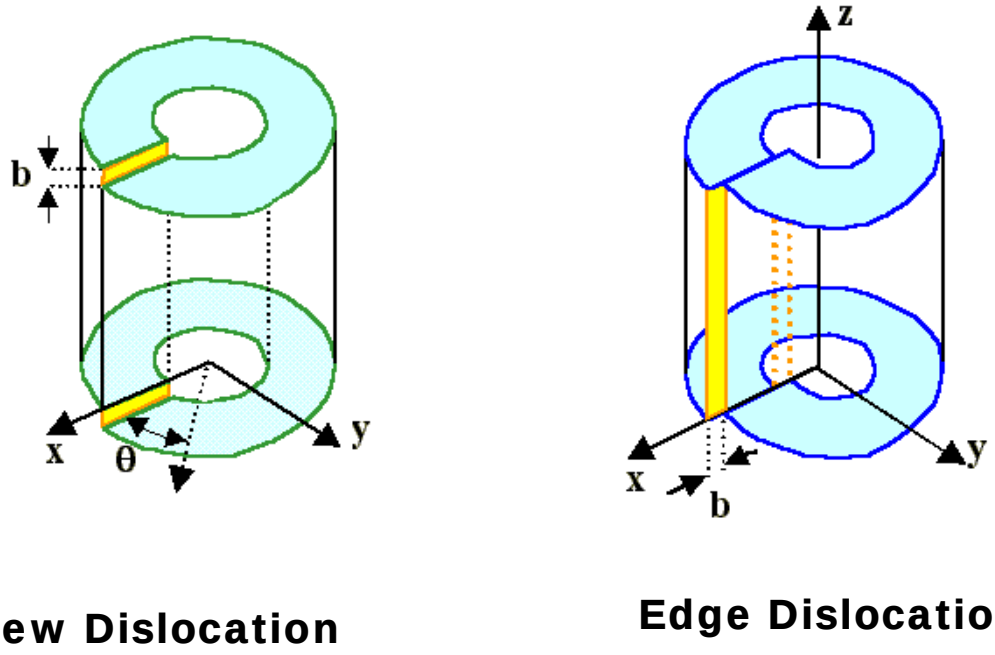

Screw Dislocation **Edge Dislocation**

Figure 4.4 Screw dislocation and Edge dislocation

The stress fields in isotropic media for screw and edge dislocation are listed in the following equations.

For screw dislocation,

$$\sigma_{xx} = \sigma_{yy} = \sigma_{zz} = \sigma_{xy} = \sigma_{yx} = 0$$

$$\sigma_{xz} = \sigma_{zx} = -\frac{G \cdot b}{2\pi} \cdot \frac{y}{x^2 + y^2} = -\frac{G \cdot b}{2\pi} \cdot \frac{\sin\theta}{r}$$

$$\sigma_{yz} = \sigma_{zy} = \frac{G \cdot b}{2\pi} \cdot \frac{x}{x^2 + y^2} = \frac{G \cdot b}{2\pi} \cdot \frac{\cos\theta}{r}$$

For edge dislocation,

$$\sigma_{xx} = -D \cdot y \frac{3x^2 + y^2}{(x^2 + y^2)^2}$$

$$\sigma_{yy} = D \cdot y \frac{x^2 - y^2}{(x^2 + y^2)^2}$$

$$\sigma_{xy} = \sigma_{yx} = D \cdot x \frac{x^2 - y^2}{(x^2 + y^2)^2}$$

$$\sigma_{zz} = \nu \cdot (\sigma_{xx} + \sigma_{yy})$$

$$\sigma_{zz} = \sigma_{zx} = \sigma_{yz} = \sigma_{zy} = 0$$

$$D = Gb / 2\pi (1 - \nu)$$

where G is the shear modulus, ν is the Poisson's ratio, b is the Burger's vector, and (x,y) are the coordinates of the field point. In Figure 4.5, the stress field around a single edge dislocation is shown.

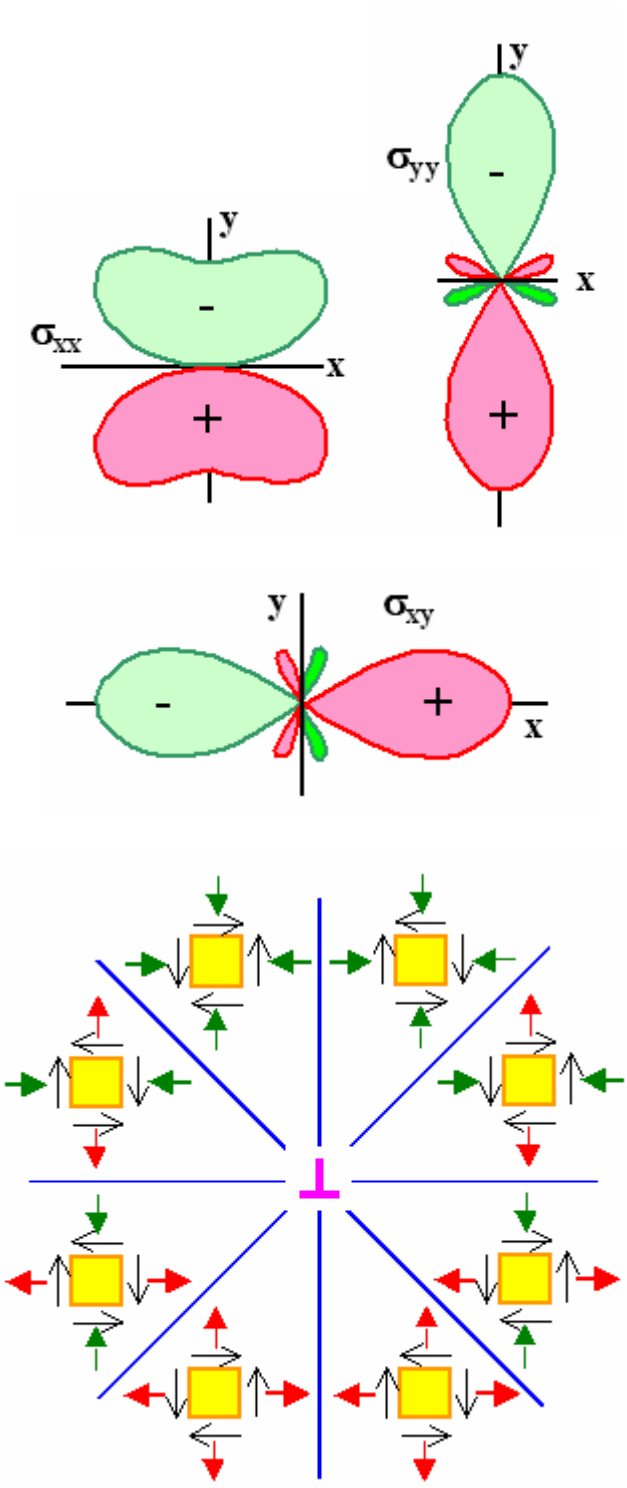

Figure 4.5 Single edge dislocation stress fields

For edge dislocation, the sign of the stress and strain components are reversed when the sign of the Burger's vector is reversed. A singularity exist at the core of the dislocation, so stress fields exclude the dislocation core and the cutoff core radius can be taken to be about 1*b* to 4*b*. In the case of a mixed dislocation, the solutions for the edge and screw component of the mixed dislocation are calculated separately and superimposed.

4.1.4 Forces on dislocations

Since the movement of a dislocation is only on its glide plane, only the shear stress on that plane needs to be considered for the forces acting on dislocations. The normal components of the stress acting on the glide plane are perpendicular to the glide plane and thus will not contribute to the movement of a dislocation. All shear stress components in the glide plane act on the dislocation, but it is only their combined effects in the direction of the Burger's vector is relevant. This is called the **r**esolved shear stress τ_{res}. The resolved shear stress points along the direction of the Burger's vector. However, the direction of the force component acting on the moving dislocation is always perpendicular to the dislocation line direction. The force component along the dislocation line direction does not contribute, because a dislocation cannot move along its own direction. As a special case in single edge dislocation, the effective force direction and resolved shear stress direction will be the same, because the Burger's vector's direction is perpendicular to the glide plane. All of these situations are shown in Figure 4.6.

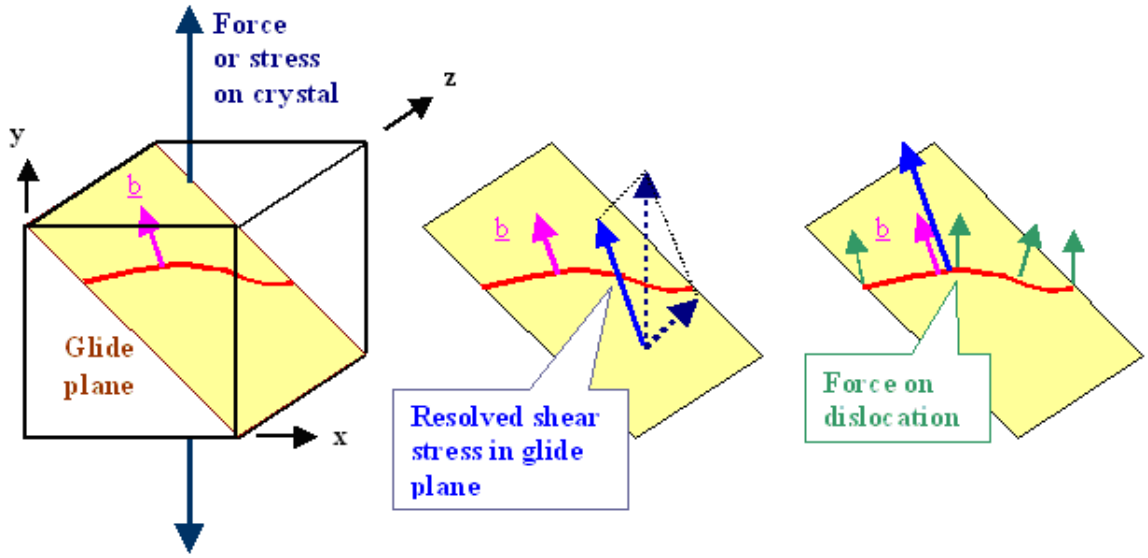

Figure 4.6 Directions of Resolved shear stress and force on dislocation

Under the influence of the force F the dislocation moves and work done in this motion is W = Force times distance. If the dislocation moves through the crystal on a glide plane with the total area A, the upper half of the crystal moves by $\underline{b}$ relative to the lower half which is the distance throug which work has been done. This only happens if a shear force acts on the crystal, and this force obviously does some work W. This work is done in increments by moving the dislocation through the crystal. The acting shear stress in this case is $\tau = F/A$. and the force F is the component of the external force that is contained or "resolved" in the glide plane as discussed above.

For the total work W done by moving half of the crystal a distance equal to the Burger's vector b, $W = A \cdot \tau \cdot b$, with $A \cdot \tau$ = Force, b = Burger's vector = distance. After dividing W into incremental steps dW, the incremental work is done on an incremental area that consists of an incremental piece dl of the dislocation moving for an incremental distance ds. The relation between the incremental work dW to the total work W then is

just the ratio between the incremental area to the total area, dW/W= ds · dl/A, then dW= $A \cdot \tau \cdot b \cdot \mathrm{d}l \cdot \mathrm{d}s/A = \tau \cdot b \cdot \mathrm{d}l \cdot \mathrm{d}s$.

An incremental piece of work dW can always be expressed as a force times an incremental distance ds; i.e. d$W = F \cdot \mathrm{d}s$. The force F acting on the incremental length dl of dislocation obviously is $F = t \cdot b \cdot dl$. After redefining the force on a dislocation in magnitude and referring it to the unit length dl, $|F| = F/\mathrm{d}l$, a very simple formula for the magnitude of the force acting on a unit length of a dislocation can be obtained.

$$|F| = \tau \cdot b$$

In that expression, τ is the component of the shear strain in the glide plane in the direction of $\underline{b}$. This is normally not a known quantity but must be calculated.

4.1.5 Interactions between Dislocations

By using the expressions for the stress and strain fields of edge and screw dislocations, one can calculate the resolved shear stress caused by one dislocation on the glide plane, and determine its effect on other dislocations.

The superposition of the stress fields of two dislocations that move toward each other can result in two possible situations: (a) the combined stress field is larger than that of a single dislocation and the dislocations repulse each other. That will happen if regions of compressive/tensile stress from one dislocation overlap with regions of compressive/tensile stress from the other dislocation. (b) The combined stress field is smaller than that of the single dislocation and dislocations attract each other. That will happen if regions of compressive stress from one dislocation overlap with regions of tensile stress from the other dislocation. Some simple cases are shown below.

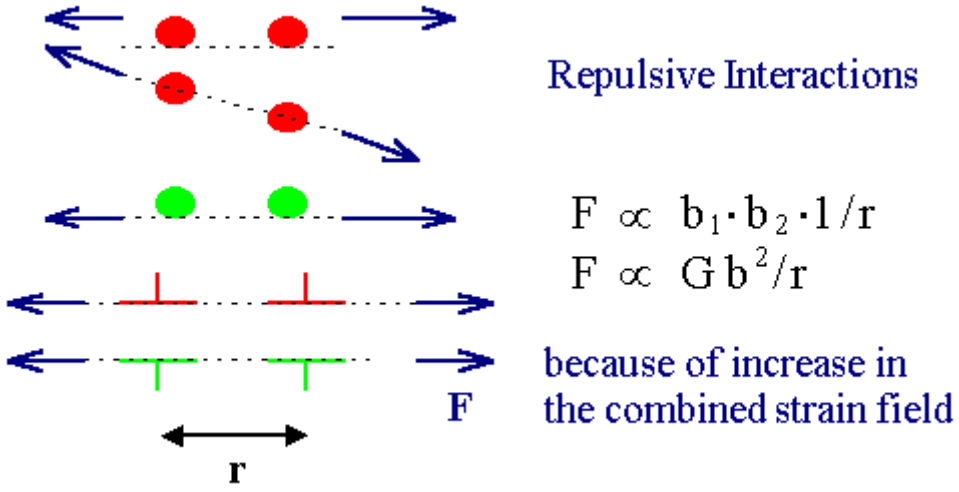

Figure 4.7 Dislocations with identical b on the same glide plane

Dislocations with identical *b* on the same glide plane always repel each other. In Figure 4.7, the blue arrows show the direction of the interaction force. In this diagram, the dot symbol stands for screw dislocations and half cross stands for edge dislocations.

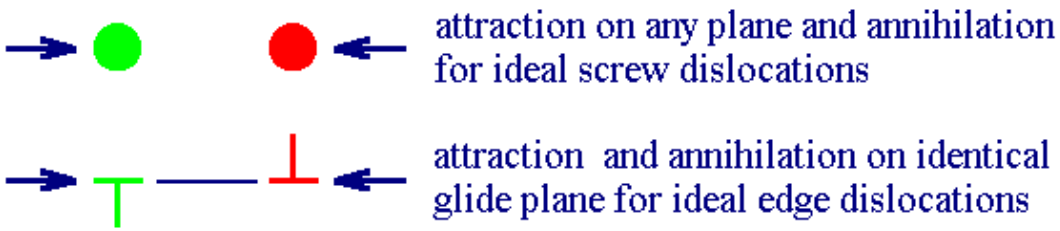

Figure 4.8 Dislocations with opposite b on the same glide plane

Dislocations with opposite *b* vectors on the same glide plane attract and annihilate each other. In Figure 4.8, the blue arrows show the direction of interaction force. The dot symbol stands for screw dislocations and half cross stands for edge dislocations.

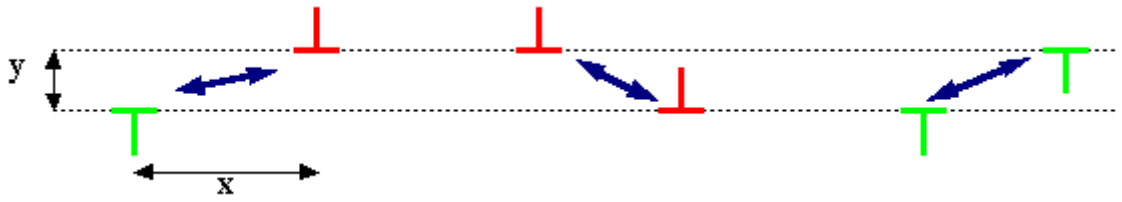

Figure 4.9 Edge dislocations with identical or opposite Burger's vector **b** on neighboring glide planes

Edge dislocations with identical or opposite Burger's vector $\underline{b}$ on neighboring glide planes may attract or repulse each other, depending on the precise geometry. The blue double arrows in the Figure 4.9 may signify repulsion or attraction, but the dislocations continues to travel along the glide planes as they can not jump from one glide plane to another.

The general formula for the forces between edge dislocations in the geometry shown above is

$$F_x = \frac{Gb^2}{2\pi(1-\nu)} \cdot \frac{x \cdot (x^2 - y^2)}{(x^2 + y^2)^2}$$

$$F_y = \frac{Gb^2}{2\pi(1-\nu)} \cdot \frac{y \cdot (3x^2 + y^2)}{(x^2 + y^2)^2}$$

The formula for F_y is given for the sake of completeness, because the dislocations can not move in y-direction to across glide planes. In the F_x expression, when two dislocations are on the same glide plane *($y = 0$)*, only a $1/x$ term survives in the expression signifying a $1/r$ dependence of the force on the distance r between the dislocations. For $y < 0$ or $y > 0$, the dislocations are on different glide planes and there are

zones of repulsion and attraction. At some specific positions the force is zero - this would be the equilibrium configurations, which are shown in Figure 4.10

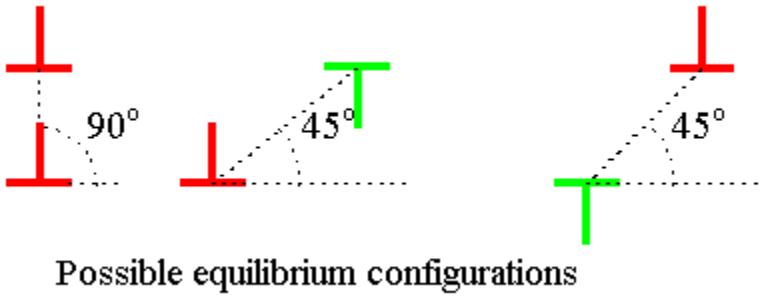

Figure 4.10 Dislocation equilibrium configurations

4.2 Dislocation stress field calculation

To calculate the stress field of dislocations, the effect of a dislocation effect is treated as an eigen-strain problem in the elastic theory. A Green function method is introduced to solve the elastic stress, strain and dislocations field caused by the given eigen-strain. For a single dislocation, the effect of a dislocation is transferred into the eigen-strain form with Burger's vector related to the stress field. Furthermore, the dislocation density tensor approach is introduced to simulate a distribution of dislocations.

4.2.1 Eigenstrain in elastic theory

The total strain ε_{ij} is the sum of elastic strain e_{ij} and eigen-strain ε_{ij}^{*}

$$\varepsilon_{ij} = e_{ij} + \varepsilon_{ij}^{*} \tag{4.1}$$

The compatibility equation relates the strain with the displacement as

$$\varepsilon_{ij} = \frac{1}{2}\left(u_{i,j} + u_{j,i}\right), \text{ where } u_{i,j} = \partial u_i / \partial x_j \tag{4.2}$$

Also the elastic strain is related to the elastic stress by Hook's law

$$\sigma_{ij} = C_{ijkl} e_{ij} = C_{ijkl}\left(\varepsilon_{kl} - \varepsilon^*_{kl}\right) \tag{4.3}$$

In terms of, the stress can be expressed as

$$\sigma_{ij} = C_{ijkl}\left(u_{k,l} - \varepsilon^*_{kl}\right) \tag{4.4}$$

where C_{ijkl} are the elastic constants and the summation convention for the repeated indices is applied.

When eigen-stress is calculated, the material is assumed to be free from external forces and surface constraints. When these conditions for the free body are not satisfied, the stress field can be constructed from the superposition of the eigen-stress of the free body and the solution of a proper boundary value problem. In our scheme, the boundary value problem will be solved by BEM with the calculation of fundamental solutions which includes Green function evaluation.

For a free body, the equilibrium equations are

$$\sigma_{ij,j} = 0 \quad (i = 1,2,3) \tag{4.5}$$

The free external boundary conditions satisfy the equations

$$\sigma_{ij} n_j = 0 \tag{4.6}$$

where *n* is the exterior unit vector which is normal to the boundary.

By substituting eq. (4.4) into eq.(4.5) and eq.(4.6), the relationship between eigen-strain and displacement are

$$C_{ijkl} u_{k,lj} = C_{ijkl} \varepsilon^*_{kl,j} \tag{4.7}$$

and

$$C_{ijkl}u_{k,l}n_j = C_{ijkl}\varepsilon^*_{kl}n_j \tag{4.8}$$

The contribution of eigen-strain to the equilibrium equations is very similar to the body force. The equilibrium equations under body force b_i are $C_{ijkl}u_{k,lj} = -b_i$ .Similarly, $C_{ijkl}\varepsilon^*_{kl}n$ behaves like a surface force on the boundary. Thus, it can be concluded that the elastic displacement field caused by ε^*_{ij} in a free body is equivalent to a body force $C_{ijkl}\varepsilon^*_{kl,j}$ and a surface force $C_{ijkl}\varepsilon^*_{kl}n$.

Next, the method to evaluate the associate elastic fields in displacements, stresses and strains will be developed for given distribution of eigen-strain ε^*_{ij}. Particularly, the problem with uniform ε^*_{ij} will be discussed since it will represent dislocation effects in latter studies.

4.2.2 Green Function Method

The fundamental equations to be solved for given eigen-strain ε^*_{ij} similar to a body force are eq.(4.7). The Green function $G_{ij}\left(x - x^{'}\right)$ is defined as the displacement component in the x_i direction at point x when a unit body force in the x_j direction is applied at point $x^{'}$ in the infinite domain. By this definition of Green function, the displacement in eq.(4.7) can be considered as a displacement caused by the body force $-C_{jlmn}\varepsilon^*_{mn,l}$ applied in the x_i direction. Since $G_{ij}\left(x - x^{'}\right)$ is the solution for the unit body force applied in the x_j direction, the solution for the present problem is the product of $G_{ij}\left(x - x^{'}\right)$ and the body force $-C_{jlmn}\varepsilon^*_{mn,l}$. Then eq.(4.7) can be expressed as

$$u_i(x) = -\int_{-\infty}^{\infty} G_{ij}(x - x') C_{jlmn} \varepsilon^*_{mn,l}(x') dx' \tag{4.9}$$

Integrating by parts and assuming that the boundary terms vanish, eq.(4.9) becomes

$$u_i(x) = \int_{-\infty}^{\infty} C_{jlmn} \varepsilon^*_{mn}(x') \frac{\partial}{\partial x_1'} G_{ij}(x - x') dx' \tag{4.10}$$

For an infinite body

$$(\partial / \partial x_l') G_{ij}(x - x') = -(\partial / \partial x_l) G_{ij}(x - x')$$

Therefore, eq. (4.10) becomes

$$u_i(x) = -\int_{-\infty}^{\infty} C_{jlmn} \varepsilon^*_{mn}(x') G_{ij,l}(x - x') dx' \tag{4.11}$$

where

$$G_{ij,l}(x - x') = \partial / \partial x_l G_{ij}(x - x') = -\partial / \partial x_l' G_{ij}(x - x')$$

The strain and stress can be obtained by combining eq.(4.11) and eqs (4.1) to (4.4) as

$$\varepsilon_{ij}(x) = -\tfrac{1}{2} \int_{-\infty}^{\infty} C_{klmn} \varepsilon^*_{mn}(x') \{ G_{ik,lj}(x - x') + G_{jk,li}(x - x') \} dx' \tag{4.12}$$

and

$$\sigma_{ij}(x) = -C_{ijkl} \left\{ \int_{-\infty}^{\infty} C_{pqmn} \varepsilon^*_{mn}(x') G_{kp,ql}(x - x') dx' + \varepsilon^*_{kl}(x) \right\} \tag{4.13}$$

To connect with the dislocation theory which will be discussed in latter sections, eq.(4.13) can be rewritten as

$$\sigma_{ij}(x) = C_{ijkl} \int_{-\infty}^{\infty} \varepsilon_{sth} \varepsilon_{\ln h} C_{pqmn} G_{kp,ql}(x - x') \varepsilon^*_{sm}(x') dx' \tag{4.14}$$

where ε_{sth} and $\varepsilon_{\ln h}$ are the permutation tensors.

Since $\varepsilon_{sth} \varepsilon_{\ln h} = \delta_{sl} \delta_{tn} - \delta_{sn} \delta_{tl}$, where δ_{ij} is the Kronecker delta, eq. (4.14) becomes

$$\sigma_{ij}(x) = C_{ijkl}\int_{-\infty}^{\infty} C_{pqmn}\left(G_{kp,qn}\varepsilon^{*}_{ml} - G_{kp,ql}\varepsilon^{*}_{mn}\right)dx' \tag{4.15}$$

Green's functions satisfy

$$C_{mnpq}G_{pk,qn}\left(x - x'\right) = -\delta_{mk}\delta\left(x - x'\right) \tag{4.16}$$

where $\delta\left(x - x'\right)$ is Dirac's delta function. It has the property

$$\int_{-\infty}^{\infty} \varepsilon^{*}_{ml}\left(x'\right)\delta\left(x - x'\right)dx' = \varepsilon^{*}_{ml}(x) \tag{4.17}$$

Therefore, eq.(4.15) is equivalent to eq.(4.13).

The Green's function for the two dimensional plane strain problem can be obtained by considering the elastic field due to a distributed line force along the x_3 axis,

$$G_{ij}\left(x_1 - x_1', x_2 - x_2'\right) = \int_{-\infty}^{\infty} G_{ij}\left(x - x'\right)dx_3' \tag{4.18}$$

For isotropic media,

$$G_{ij}\left(x_1 - x_1', x_2 - x_2'\right) = \left\{\bar{x}_i\,\bar{x}_j\Big/\bar{R}^2 - (3 - 4\nu)\delta_{ij}\log\bar{R}\right\}\Big/8\pi(1-\nu)\mu \tag{4.19}$$

where $\bar{R}^2 = \left(x_1 - x_1'\right)^2 + \left(x_2 - x_2'\right)^2$

Green's functions for the plane stress problem can be derived by replacing E with $E(1+2\nu)/(1+\nu)^2$ and ν with $\nu/(1+\nu)$ in the plane strain expressions, because in both cases these replacements give the same form of Hook's law.

The Green's function expression is identical to the fundamental solution of the BEM formulation of Chapter-2. For the simplicity in the programming, the fundamental solution subroutine and the Green function subroutine are shared. The anisotropic formulation for BEM is already shown in Chapter-2.

4.2.3 Dislocation Modeling

Before the dislocation theory can be derived, the definition of the dislocation line should be clarified. The dislocation line is a part of the boundary of a slip plane (glide plane), but the part of the boundary which is exposed on the surface of the material is not called the dislocation line. In screw dislocation and edge dislocation examples mentioned in section 4.1.1, the dislocation line is the *z* axis. To define the direction of a dislocation line in a more precise way, consider a slip plane *S* as shown in Figure 4.11. The upper plane, which is denoted by S+, is slipped by *b* relative to the lower plane, which is denoted by S-. To specify this configuration of the slip, the definition of the direction *v* of the dislocation line **L** follows the right handed cork-screw rule advancing related to the Burger's circuit **c**. For crystal, the Burger's vector is usually a lattice vector. Such a dislocation is also called a perfect dislocation.

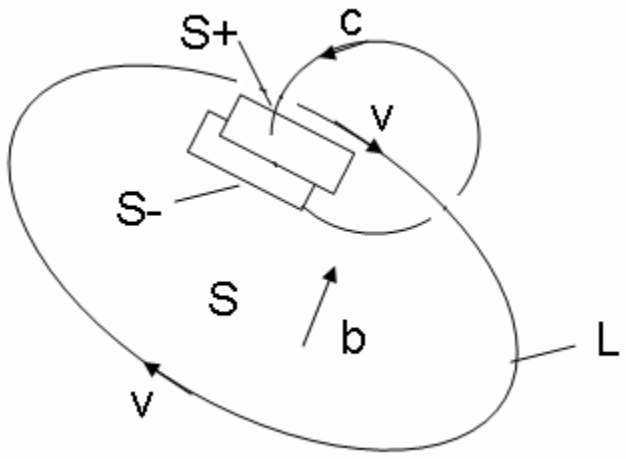

Figure 4.11 Dislocation Line **L** and the Burgers circuit **c**

The displacement gradient $u_{i,j}$ is also called the total distortion; it consists of elastic distortion β_{ij} and plastic distortion β^*_{ji}.

$$u_{i,j} = \beta_{ij} - \beta^*_{ji} \tag{4.20}$$

The total strain ε_{ij}, elastic strain e_{ij} and eigen-strain ε^*_{ij} defined in eq.(4.1) are

$$\varepsilon_{ij} = \tfrac{1}{2}\left(u_{i,j} + u_{j,i}\right) \tag{4.21}$$

$$e_{ij} = \tfrac{1}{2}\left(\beta_{ij} + \beta_{ji}\right) \tag{4.22}$$

$$\varepsilon^*_{ij} = \tfrac{1}{2}\left(\beta^*_{ij} + \beta^*_{ji}\right) \tag{4.23}$$

Since β^*_{ji} is caused by the slip b_i of plane S+, whose normal vector toward S- is n_j, β^*_{ji} can be expressed as

$$\beta^*_{ji}(x) = -b_i n_j \delta\left(S - x\right) \tag{4.24}$$

where $\delta\left(S - x\right)$ is the Dirac delta function in the normal direction of S.

Substituting eq. (4.24) into (4.23) we get

$$\varepsilon^*_{ji}(x) = -\tfrac{1}{2}\left(b_i n_j + b_j n_i\right)\delta\left(S - x\right) \tag{4.25}$$

By substituting eq.(4.25) into eq.(4.11) and using the relationship

$$\int_\Omega \delta\left(S - x'\right)dx' = \int_S dS \tag{4.26}$$

one can get

$$u_i(x) = \int_S C_{jlmn} b_m G_{ij,l}\left(x - x'\right) n_n dS(x') \tag{4.27}$$

After differentiation, eq.(4.27) becomes

$$u_{i,j}(x) = \int_S C_{klmn} b_m G_{ik,lj}\left(x - x'\right) n_n dS(x') \tag{4.28}$$

The elastic distortion can be obtained by substituting eq. (4.28) into eq.(4.20)

$$\beta_{ji}(x) = \int_S C_{klmn} b_m G_{ik,lj}\left(x - x'\right) n_n dS(x') + b_i n_j \delta(S - x) \tag{4.29}$$

By integrating eq.(4.29), we get

$$\beta_{ji}(x) = \int_L \varepsilon_{jnh} C_{pqmn} G_{ip,q}\left(x - x'\right) b_m v_h dl(x') \tag{4.30}$$

where *v* is the direction of the dislocation line **L** and *dl* is the dislocation line element.

The stress components are

$$\sigma_{ij} = C_{ijkl}\beta_{lk} \tag{4.31}$$

and using eq.(4.30)

$$\sigma_{ij}(x) = C_{ijkl}\int_L \varepsilon_{\ln h} C_{pqmn} G_{kp,q}\left(x - x'\right) b_m v_h dl(x') \tag{4.32}$$

Consider a dislocation loop **L** in Figure 4.11 where **L** is the boundary of the slip plane S. The slip ***b*** on S introduces a plastic distortion β_{ji}^{p}.

$$\beta_{ij}^{p} dx = -b_i n_j dS = -b_i dS_j \tag{4.33}$$

where $dx = dx_1\, dx_2\, dx_3$, *dS* is the surface element of S, and **n** is the unit normal vector of S. β_{ji}^{p} is called the dislocation loop density tensor α_{hi}.

The dislocation density tensor is defined by

$$\alpha_{hi} dx = b_i v_h dl = b_i dl_h \tag{4.34}$$

By combining integrated eq.(4.34) and differentiated eq.(4.33), the relationship between β_{ji}^{p} and α_{hi} is

$$\alpha_{hi} = -\varepsilon_{hlj}\beta_{ji,l}^{p} \tag{4.35}$$

where ε_{hlj} is the permutation tensor.

The result is not only valid for single dislocation loop, but also holds for the continuous distributed dislocations, where β_{ji}^{p} and α_{hi} are spatial functions. In that case,

$$\alpha_{hi}dx = \sum b_i v_h dl \tag{4.36}$$

where the summation is taken on all dislocation segments contained in the infinitesimal cube *dx*.

The dislocation density tensor α_{hi} expresses the x_i component of the total Burger's vector of dislocations threading the unit surface perpendicular to the x_h direction.

The stress field due to the continuous distribution of dislocations can be obtained from eq.(4.36) and eq.(4.32) as

$$\sigma_{ij}(x) = C_{ijkl}\int_L \varepsilon_{\ln h} C_{pqmn} G_{kp,q}\left(x - x'\right)\alpha_{hm}(x')dx' \tag{4.37}$$

The single dislocation line can be treated as a special case when the dislocation density tensor takes the form of Dirac's delta function. As examples in Figure 4.4, for the single screw dislocation, the dislocation density tensor are $\alpha_{33} = b_3\delta(x_1)\delta(x_2)$, and $\beta_{23}^{p} = b_3\delta(x_2)H(-x_1)$. For the single edge dislocation, $\alpha_{31} = b_1\delta(x_1)\delta(x_2)$ and $\beta_{21}^{p} = b_1\delta(x_2)H(-x_1)$.

For the continuous distributions of dislocations

$$u_{i,j} = \beta_{ji} + \beta_{ji}^{p} \tag{4.38}$$

where β_{ji} is the elastic distortion. The total distortion is the sum of elastic and plastic distortion. Since the plastic distortion is caused by slip, it does not produce any distortion among lattice points. The elastic distortion is originated in an elastic deformation of the lattices.

4.3. Multiple Dislocations Stress Field Calculation

The interaction between dislocations can be evaluated through stress field calculation. As there are thousands or even millions of dislocations exit in the grains, the combined stress field of dislocations can be calculated in two ways.

The first approach is called the discrete dislocation method[1-7], in that method stress field of each dislocation is calculated and added together to get the total stress field. This method is straightforward, but very time consuming, since the total number of single dislocation calculation can reach millions in one time step.

The second method is the dislocation density tensor method[8-13]. With the given distribution of dislocations over a region, the stress field caused by that region can be evaluated by integrating the dislocation stress fields over the domain. The domain integration can be transformed into a boundary integral because of the special form of the Green's function.

4.3.1. Discrete Dislocation Method

The stress field for discrete dislocation can be calculated from eq. (4.32) which is rewritten below.

$$\sigma_{ij}(x) = C_{ijkl}\int_L \varepsilon_{\ln h} C_{pqmn} G_{kp,q}(x-x')b_m v_h dl(x')$$

For edge dislocation m=1, h=3, v=1 along x_3, and Burger's vector is b along x_1. The expression for the stress field becomes

$$\sigma_{ij}(x) = C_{ijkl}\int_L \varepsilon_{\ln 3} C_{pq1n} G_{kp,q}(x-x')bdl(x') \tag{4.39}$$

With dislocation line as axis, *dl(x')* is x_3 from negative infinity to positive infinity and eq.(4.39) becomes

$$\sigma_{ij}(x) = C_{ijkl}\int_{-\infty}^{+\infty}\varepsilon_{\ln 3}C_{pq1n}G_{kp,q}(x-x')bdx_3 \tag{4.40}$$

According to eq.(4.18), the Green function in two-dimension can be expressed as

$$G_{ij}(x_1-x_1',x_2-x_2') = \int_{-\infty}^{+\infty}G_{ij}(x-x')bdx_3'$$

where G on the left-hand-side is the two-dimensional Green function, and the G on the right-hand-side is the general form for three-dimensions. In two-dimensional case, along x_3 axis, $x'=(0,0,x_3)$, then eq.(4.18) becomes

$$G_{ij}(x_1,x_2) = \int_{-\infty}^{+\infty}G_{ij}(x-x_3')dx_3' \tag{4.41}$$

and the derivative of Green function is

$$G_{ij,k}(x_1,x_2) = \int_{-\infty}^{+\infty}G_{ij,k}(x-x_3')dx_3' \tag{4.42}$$

By substituting eq.(4.42) into (4.40), one obtains

$$\sigma_{ij}(x) = C_{ijkl}\varepsilon_{\ln 3}C_{pq1n}G_{ij,k}(x_1,x_2)b \tag{4.43}$$

This expression of stress filed is for the two-dimensional single edge dislocation, and the evaluation of stress requires is no integration. In other words, the stress field can be expressed as a function of geometry alone and stress can be computed by simply substituting the location x_1, x_2 in eq. (4.43).

4.3.2. Dislocation Density Tensor Method

The dislocation density tensor method is based on eq.(4.37) as the general expression. As a special case for single edge dislocation, the dislocation density tensor is defined as: *b* at the origin point, and 0 elsewhere,

$$\alpha_{31} = b\delta(x_1)\delta(x_2)$$

Then eq.(4.37) becomes

$$\sigma_{ij}(x) = C_{ijkl}\int \varepsilon_{\ln 3} C_{pq1n} G_{kp,q}(x - x_3')b dx_3' \tag{4.44}$$

Comparing eq.(4.44) with eq.(4.39), we find that this special case of dislocation density tensor exactly matches the discrete dislocation result.

For the general case, eq.(4.37) can be expressed as integration with 3 different dimensions as

$$\sigma_{ij}(x) = C_{ijkl}\iiint \varepsilon_{\ln h} C_{pqmn} G_{kp,q}(x - x')\alpha_{hm}(x')dx_1'dx_2'dx_3' \tag{4.45}$$

or

$$\sigma_{ij}(x) = C_{ijkl}\varepsilon_{\ln h} C_{pqmn}\iiint G_{kp,q}(x - x')\alpha_{hm}(x')dx_1'dx_2'dx_3' \tag{4.46}$$

4.3.3. Transformation from Domain Integral into Boundary Integral

To evaluate the triple integral in eq.(4.46), some special treatment is necessary to simplify the volume integral into a boundary integral.[14-17]

Since $G_{ij,k}(x_1, x_2) = \int_{-\infty}^{+\infty} G_{ij,k}(x - x_3')dx_3'$ and $\alpha_{31} = b$ for two-dimensional edge dislocation

$$\iiint G_{ij,k}(x - x')\alpha_{hm}(x')dx_1'dx_2'dx_3' = b\iint G_{ij,k}(x - x')dx_1'dx_2'.$$

To evaluate the double integral we introduce polar coordinates as

$$\iint G_{ij,k}(x-x')dx_1'dx_2' = \iint G_{ij,k}(r,\theta)rdrd\theta \tag{4.47}$$

Let $F(r,\theta) = \int G_{ij,k}(r,\theta)rdr$, then

$$\iint G_{ij,k}(x-x')dx_1'dx_2' = \int F(r,\theta)d\theta \tag{4.48}$$

Since $d\theta = d\Gamma\cos\varphi = d\Gamma\dfrac{r_i n_i}{r(Q)}$,

$$\iint G_{ij,k}(x-x')dx_1'dx_2' = \int_\Gamma \frac{r_i n_i}{r(Q)}F(Q)d\Gamma(Q) \tag{4.49}$$

where

$$F(Q) = \int_0^{r(Q)} G_{ij,k}(x)rdr \tag{4.50}$$

Because of the special structure of $G_{ij,k}$, $G_{ij,k}$ can be expressed as

$$G_{ij,k} = \Phi_{ijk}/r \tag{4.51}$$

where Φ_{ijk} is independent of *r*, then eq. (4.50) can be rewritten as

$$F(Q) = \int_0^{r(Q)} \Phi_{ijk}dr = \Phi_{ijk}r(Q) = r(Q)^2 G_{ij,k} \tag{4.52}$$

By substituting eq.(4.52) into (4.49), one can get

$$\iint G_{ij,k}(x-x')dx_1'dx_2' = \int_\Gamma \frac{r_i n_i}{r(Q)}r(Q)^2 G_{ij,k}(x)d\Gamma(Q) \tag{4.53}$$

or

$$\iint G_{ij,k}(x-x')dx_1'dx_2' = \int_\Gamma r_i n_i r G_{ij,k}d\Gamma \tag{4.54}$$

According to this derivation, the triple integral in the expression for stress in eq.(4.46) can be reduced to a boundary integral for edge dislocations in two-dimension.

4.3.4 Error Control and Time Saving with the Mixed Method

The discrete dislocation method treats dislocations one by one and gives an exact expression for the stress field. The dislocation density tensor method takes the dislocation distribution as a whole. The accuracy of the density tensor method depends on the accuracy of the description of the dislocation distribution.

With large number of dislocations in one zone, the stress field due to all the dislocations in the zone is computed by an integration of the dislocation density tensor along the boundary of the zone. This integration involves the Gauss points over all the boundary elements enclosing the zone. Hence, the computing time depends on the number of boundary elements and the number of Gauss points, but is independent of the number of dislocations within the zone.

The running time of the discrete dislocation method is directly proportional to the total number of dislocations. For large number of dislocations, this calculation can be expensive. The dislocation density tensor method is independent of the number of dislocations and computationally less expensive compared to the discrete dislocation method.

The discrete dislocation method is more accurate and dislocation density tensor method is faster. The error in the dislocation density tensor method can be controlled by reducing the zone size. The error in the dislocation density tensor method is also small when there are a very large number of dislocations in a zone.

In Figure 4.12, the stress field is required at the observation point. The distance between the observation point and a discrete dislocation is r. Also consider r to be the

distance between the observation point and the center of a zone with a dislocation distribution.

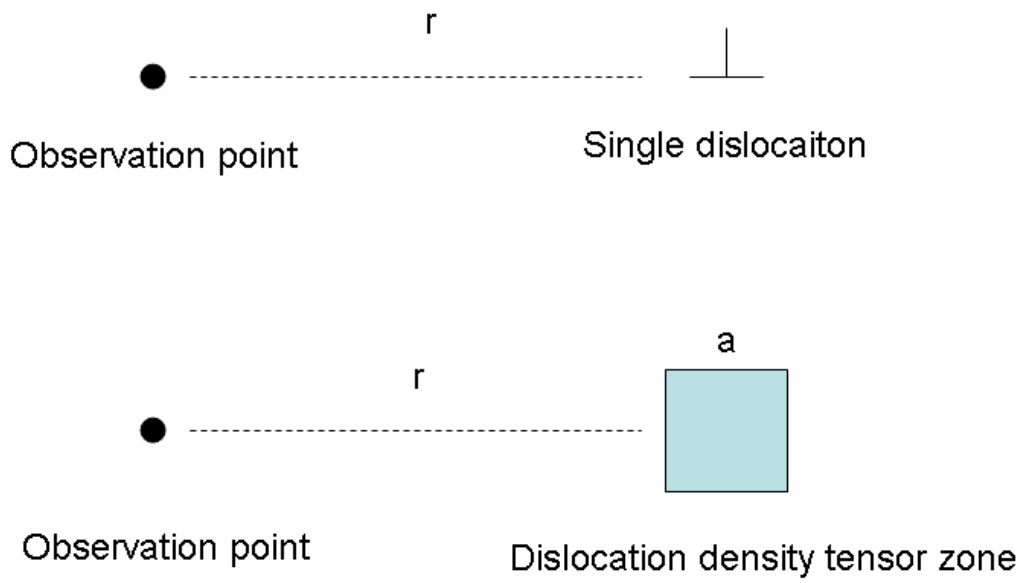

Figure 4.12 Discrete dislocation and dislocation density tensor method

To compare the accuracy of the discrete method and zone integration method for various values of *r* only, we keep a fixed zone size *a*. The observation point is moved from the left side of the zone, moved across the zone, and finally, moved to the right away from the zone.

In discrete dislocation calculation, single edge dislocation is considered. In dislocation density tensor method, $\alpha_{31} = b$ is applied over the zone to homogenously smear a single dislocation inside that zone. The result from the discrete dislocation is taken as the reference. The relative error in the dislocation density tensor calculation is computed by comparing it with the reference and the results are shown in Figure 4.13.

When $r/a > 2$, the relative error is lower than 3%. Hence, for $r/a > 2$, one can use the computationally efficient, dislocation density tensor method. When $r/a < 2$, the

cheaper, density tensor method does not yield sufficient accuracy, therefore, the discrete dislocation method is preferable.

The accuracy of the density tensor method depends on the number of dislocations within a zone. In Figure 4.14, the top row shows discrete locations and the bottom row shows the same number of dislocations smeared over a zone. We conduct the same numerical experiment by sweeping the observation point across a zone of size a. The results are shown in Figure 4.15. At the same *r/a* ratio the relative error in the stress value goes down when the total number of dislocations is increased. Also, for the same number of dislocations, the error decreases when the *r/a* ratio is increased.

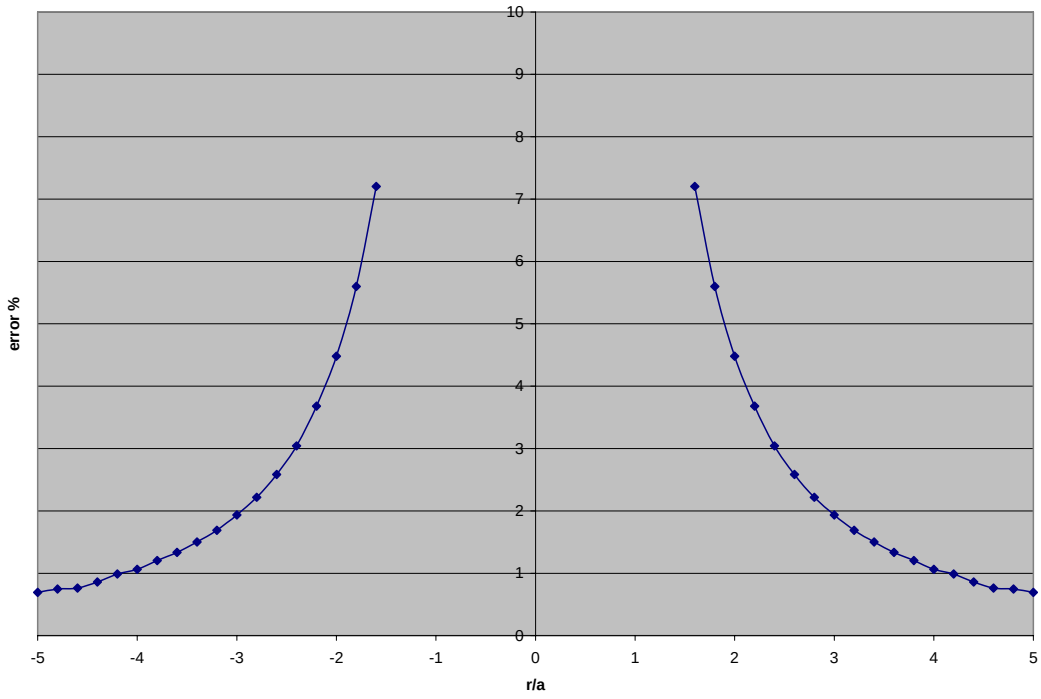

Figure 4.13 Comparison between stress calculation result from discrete dislocation and dislocation density tensor method

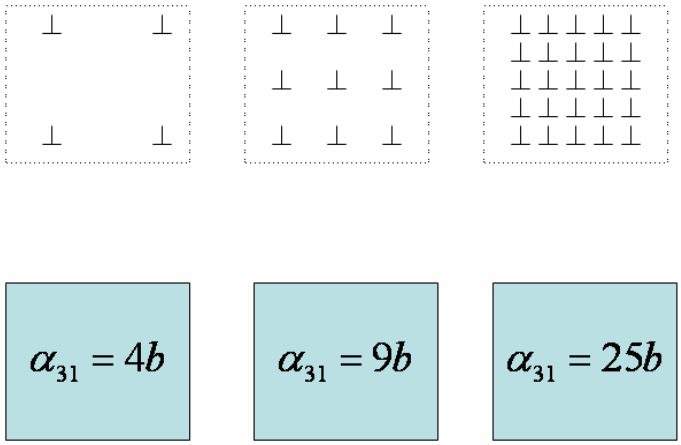

Figure 4.14 Comparison for multiple dislocations.

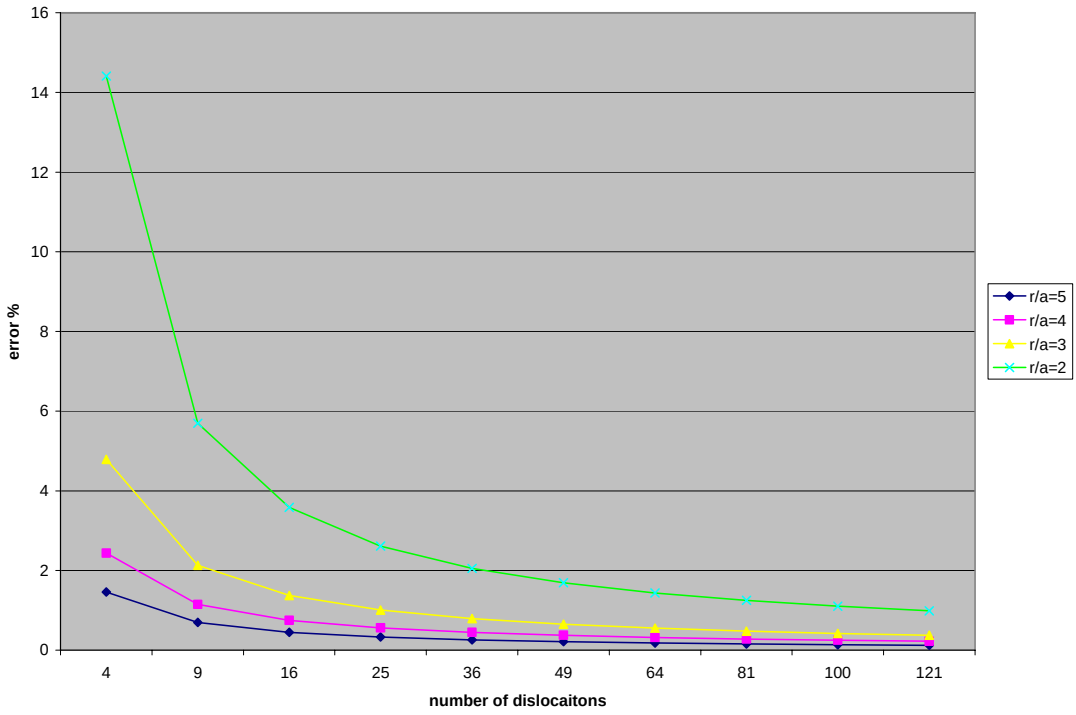

Figure 4.15 Comparison for multiple dislocations

In summary, the discrete dislocation method should be used for fewer dislocations and when the observation point is close to the dislocations. For large number of dislocations and for large distance between observation point and the dislocations, the dislocation density method should be used for fast runtime and relatively small errors.

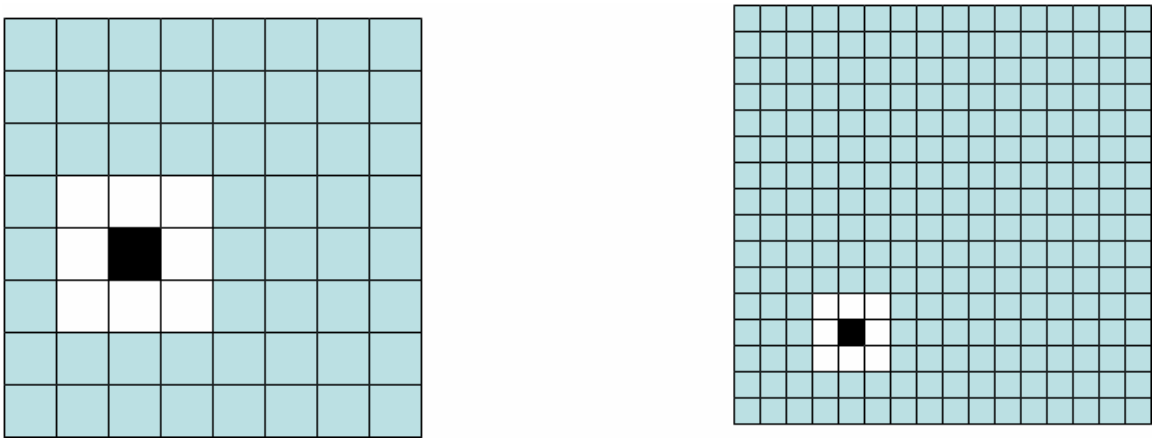

Figurer 4.16 Combined dislocation calculation scheme

To maintain good accuracy and also to reduce the computing time, a combined method is developed. This combined algorithm involves a three step process. First, as a preparation, after the position of the dislocations are known and the dimension of all the zones are given, a point in polygon calculation will decide which zone a dislocation belongs to, and how many dislocations are located inside every zone. Second, in Figure 4.16, the observer is located inside the black zone, for all the dislocations belonging to that black zone and the neighboring white zones which have a *r/a* ratio less than the threshold, discrete calculation will be performed. Finally, for all the dislocations belonging to the blue zones which have a *r/a* ratio bigger than the threshold, dislocation density tensor method are used to calculate the stress field zone by zone.

In Figure 4.16, when the size of the zone is decreased, a more accurate distribution of the dislocations is attained. When the size of the zones is made very small, the dislocation density tensor method reduces to the discrete dislocation method, with one zone containing one dislocation.

To further speed up the runtime, a tree like structure is generated for the zones to maximize the advantage of the dislocation density tensor method with the errors controlled within limits.

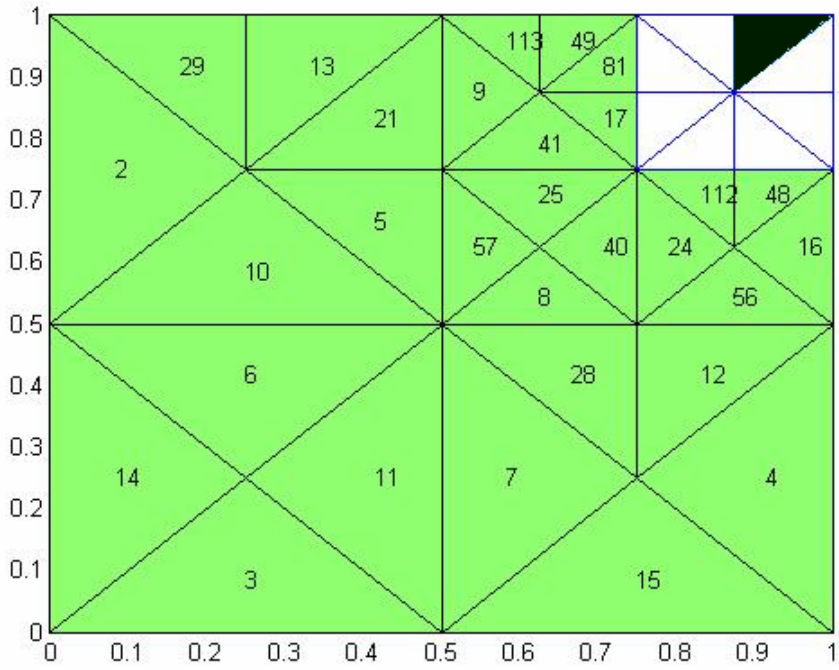

Figure 4.17 Tree like zone structure

In Figure 4.17, the distance of the observer (within the black zone) from the zones are different and the zone size changes. The zone size is controlled in such a fashion that the condition $r/a > 2$ is satisfied. In this zone structure, the number of zone integrations is reduced by making the zone size larger for zones that are farther away from the observer.

In Table 4.1, the execution times for 10,000 dislocations are given for the discrete dislocation method and the combined method with different zone numbers and different zone structures. The relative error of the combined method compared to the discrete method is also shown.

Method and zone structure	Total Runtime	Discrete Dislocation time	Density tensor zone time	Error %
Discrete only	101			
16 uniform zones	68	67.6	0.4	0.99
64 uniform zones	28	24	3.4	0.73
256 uniform zones	24	7.2	16.2	0.51
1024 uniform zones	65	1.95	61.8	0.49
32 tree structure zones	16	13	2.5	1.45
256 tree structure zones	11	1.86	8.07	1.27

Table 4.1 Runtime (in sec.) and error for different zone number and zone structure

The table shows that the run time is substantially lower for the combined method. The maximum runtime is 101sec for the discrete method. All cases of the combined methods have smaller execution time and with error less than 2%. Furthermore, the tree structures models have smaller runtime compared to the uniform structured models.

Dislocation numbers	100	1000	10000
Discrete method runtime	0.02	1.09	101

Dislocation numbers	1000	10000
Mixed method runtime	1.09 (2%)	11(1.27%)

Note: errors are shown in the parenthesis

Table 4.2 Runtime for different number of dislocations

In Table 4.2, the runtimes are shown for different number of dislocations. For discrete method, when the number of dislocations increases 10-fold, the calculation time increases roughly 100-fold. Therefore, the runtime is $O(n^2)$. In the combined method, all the errors are within the 2% limit, and the runtime is O(n).

4.4 Dislocation dynamics

A superposition technique is used to obtain the actual solution resulting from the dislocation microstructures and kinematics boundary conditions[18-24]. In the simulations, the dynamic behavior of dislocations is described by a set of constitutive rules incorporating the lattice resistance to dislocation motion, dislocation nucleation, and annihilation. This section describes the details of these constitutive rules.

The solution of the instantaneous state of a dislocated body can be obtained by decomposing the problem into two parts:

1) *An infinite body solution for n dislocations*: The stress fields can be obtained by summing over the infinite fields caused by individual dislocations. If the self

equilibrating stress field of a dislocation is denoted as σ_i in an infinite body, the total stress field caused by n dislocations can be expressed as

$$\widetilde{\sigma} = \sum_{i=1}^{n} \sigma_i \tag{4.55}$$

The summation can be calculated by the combined method with tree like zone structure which is derived in the previous section.

(b) In finite bodies, the dislocations also create tractions T and the displacements u on the boundary due to their stress field. Therefore, the boundary conditions of the finite body should be modified. The corresponding fields in the finite body can be expressed with the linear elasticity equations as

$$\nabla \cdot \hat{\sigma} = 0, \quad \hat{\varepsilon} = \nabla \hat{u}, \quad \hat{\sigma} = L : \hat{\varepsilon}, \qquad \text{in } V,$$

$$t = \hat{T} = t_0 - \widetilde{T} \qquad \text{on } S_{f,} \qquad u = \hat{U} = u_0 - \widetilde{U} \qquad \text{on } S_{u,} \tag{4.56}$$

where the fields with tilde are the ones associated with the dislocations in their current configuration and fields with hat are the corrected ones for the actual boundary conditions. ∇ is the vector 'del' operator, L is the tensor of elastic constants of the material, V is the volume of the body, t_0 and u_0 the tractions and the displacements on the boundary $S = S_u \cup S_f$. This standard boundary value problem can be solved by BEM.

The complete fields in the finite body are then obtained by superposition of the two decomposed solutions

$$u = \hat{u} + \widetilde{u}, \ \varepsilon = \hat{\varepsilon} + \widetilde{\varepsilon}, \ \sigma = \hat{\sigma} + \widetilde{\sigma} \tag{4.57}$$

The resolved shear stress acting in the slip plane at the dislocation line controls the dislocation motion and its value for the i_{th} dislocation can be expressed as

$$\tau_i = m_i \cdot \left(\hat{\sigma} + \sum_{j \neq i}^{n} \sigma_j \right) \cdot n_i \tag{4.58}$$

where m_i is the unit vector in the slip direction and n_i is the unit normal vector of the slip plane containing the i_{th} dislocation.

The velocity of a dislocation v_i in the direction of m_i can be related with the resolved shear stress through the linear drag relation

$$\tau_i b_i = B v_i \tag{4.59}$$

where B is the drag coefficient and b_i is the magnitude of the Burger's vector of the i_{th} dislocation. The dislocation motion is limited to the slip plane; in particular, climb processes are not included.

Dislocations are generated through the sources. For the nucleation of the dislocations, it is assumed that the sources are point sources at the slip plane, which generate a dislocation dipole when the magnitude of the shear stress at the source, $|\tau|$, exceeds a critical nucleation stress τ_{nuc} during a time interval t_{nuc} . The dipole comprises of two opposite dislocations with the Burger's vector $\pm b$, with the polarity being determined by the sign of the resolved shear stress. When a new dipole is generated, the total resolved shear stress τ_{nuc} balances the attractive forces that the two newly created dislocations exert on each other. The nucleation distance l_{nuc} is determined from

$$l_{nuc} = \frac{\mu}{2\pi(1-\nu)} \frac{b}{\tau_{nuc}} \tag{4.60}$$

where b is the magnitude of the Burger's vector, μ is the shear modulus and ν is the Poisson's ratio.

Two edge dislocations with the opposite Burger's vectors will annihilate each other when they come close to each other due to their self-stress field. In the simulation,

this event is assumed to occur when opposite signed dislocations comes within a critical annihilation distance l_a and they are removed from the model.

To study the grain boundary strengthening behavior, a shear deformation in plane strain is considered. The analysis is also confined to only edge dislocations and to a single slip system. The simulation unit cells in Figure 4.18 are chosen to be .86×1 μm in dimension with periodic boundary conditions. The grain size ranges from .54 to .06 μm.

The grain boundaries are marked with circles, and the boundary element nodes are marks with dots. It is interesting to notice that some boundary element nodes are not on the grain boundaries because of the periodic boundary conditions. The unit cells are cut in half at the boundary of the model, one half is in the model and the other half goes to the other side of the model. At these cut boundary, dislocations will go out and reenter from the other side, and these boundaries will not be treated as grain boundaries.

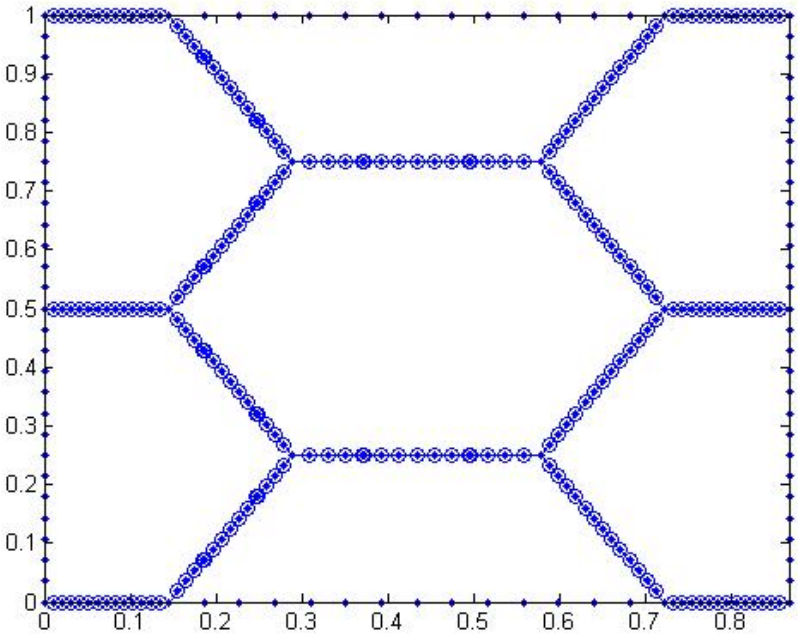

Figure 4.18 Simulation unit cell model

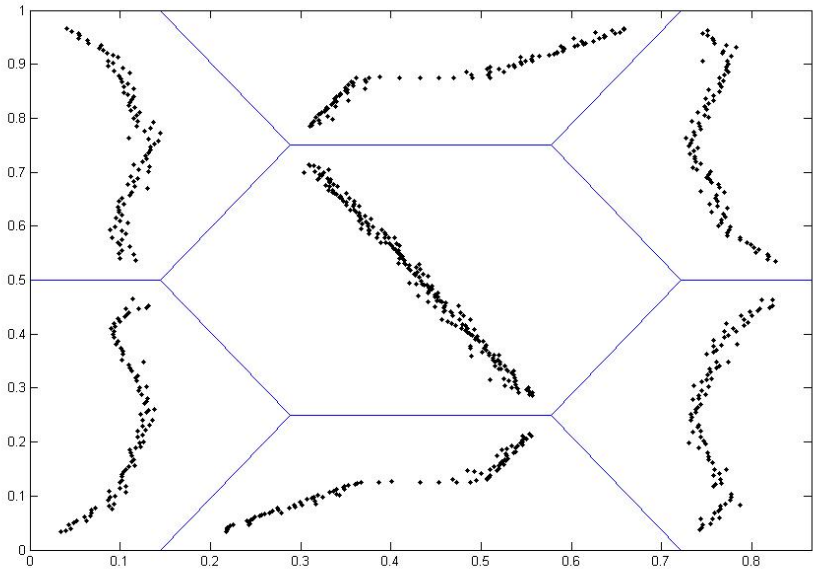

Figure 4.19 Source distributions inside unit cells

For each case, there are no initial dislocations at the beginning of the solution. The nucleation of the dislocation dipoles occurs from the randomly distributed dislocation sources at slip planes that are parallel to the x_1 axis and $10b$ apart from each other in the x_2 direction. However, the sources that are directly in contact with the boundary were taken out from the solution for smaller grain sizes in order to avoid the splitting of the dislocation dipoles into two different grains. Therefore, the absence of some sources in some grains may happen. The source distribution of the unit cell model is shown in Figure 4.19.

A critical nucleation stress, τ_{nuc}, for each source is randomly assigned from a Gaussian distribution with a mean value of τ_{nuc} = 70MPa and a standard deviation of $0.2\tau_{nuc}$. A constant nucleation time t_{nuc} = 0.00125 ms is assumed for all sources.

For all grain sizes, homogenous hexagonal grain morphology is assumed. For the elastic properties, the Young's modulus, E = 70 GPa and the Poisson ratio ν = 0.3 are chosen. No effort is made to simulate the grain boundaries in terms of the dislocation walls. The intersections of the grain boundaries with the slip planes are taken as obstacles to the dislocation motion; the dislocations are not allowed to cross the grain boundaries. When the distance between these obstacles and the approaching dislocations are less than $10b$, the approaching dislocations were pinned in their current position. This event only occurs for a few dislocations in the same slip plane, due to the repulsive forces generated between same sign dislocations. The annihilation of the opposite sign dislocations is assumed to occur when the distance between such dislocations is less than $6b$ and they are taken out of the simulation. Because of the assumed periodicity, dislocations leaving the cell reenter at the opposite side of the cell.

The magnitude of the Burgers vector is chosen to be that of copper, $b = 2.5\times10^{-10}$ m. The drag coefficient is taken as $B = 10^{-4}$ Pa.sec as a representative value, though this parameter is difficult to determine accurately for any material. A constant time-step of 5×10^{-10} sec is used in all simulations. Also a maximum cutoff velocity of $v_{max} = 20\text{ms}^{-1}$ is assigned to the dislocation velocities for numerical stability.

The analyses are carried out under pure shear and in plane strain condition with periodic boundary conditions. To achieve that, simple shearing displacements are prescribed to the top and bottom edges of the simulation unit cell through the kinematics boundary conditions that also enforce stress-free lateral sides and give a pure shear stress state where $\sigma11 = \sigma22 = 0$ for the periodic boundary conditions in the absence of the dislocations. These initial kinematics boundary conditions are updated with evolving

dislocation microstructures as given in eq. (4.56) during each displacement increment. The resulting shear stress needed to sustain the deformation is computed from the shear component of eq. (4.57) along the edges of the simulation cell using

$$\tau = \frac{1}{W}\int_0^W \sigma_{12} dx_1 \tag{4.58}$$

where W is the width of the simulation cell. The loading strain rate is 500% per second in all cases.

In Figure 4.20, the dislocation structure is shown for the cell size 0.86×1μm and grain size 0.58*0.5 μm. The dislocation pile up can be observed from this figure. Figure 4.21 shows the stress vs strain curve for the same model and yielding can be observed from this curve. Figure 4.22 shows the increase of the dislocation number and active sources number according to the time step.

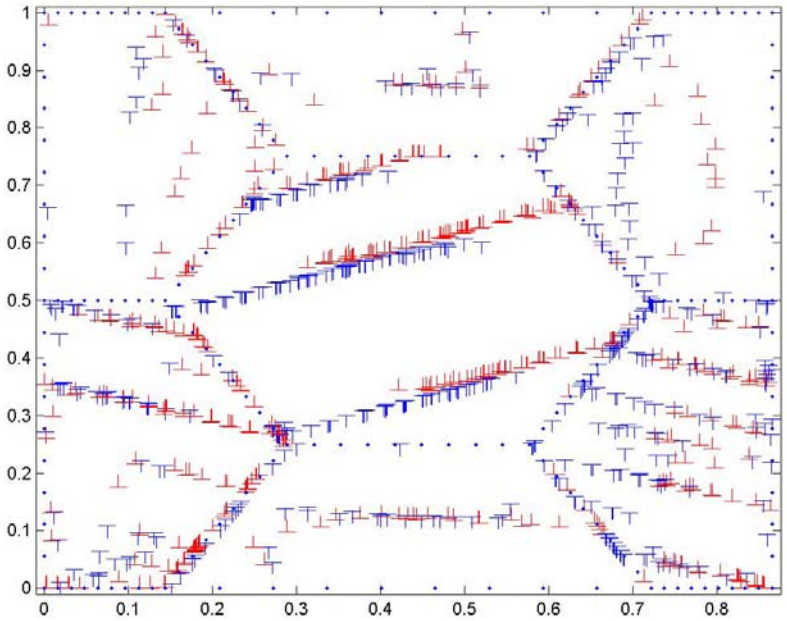

Figure 4.20 Dislocation structure at shear strain 0.3% for 0.86×1μm model

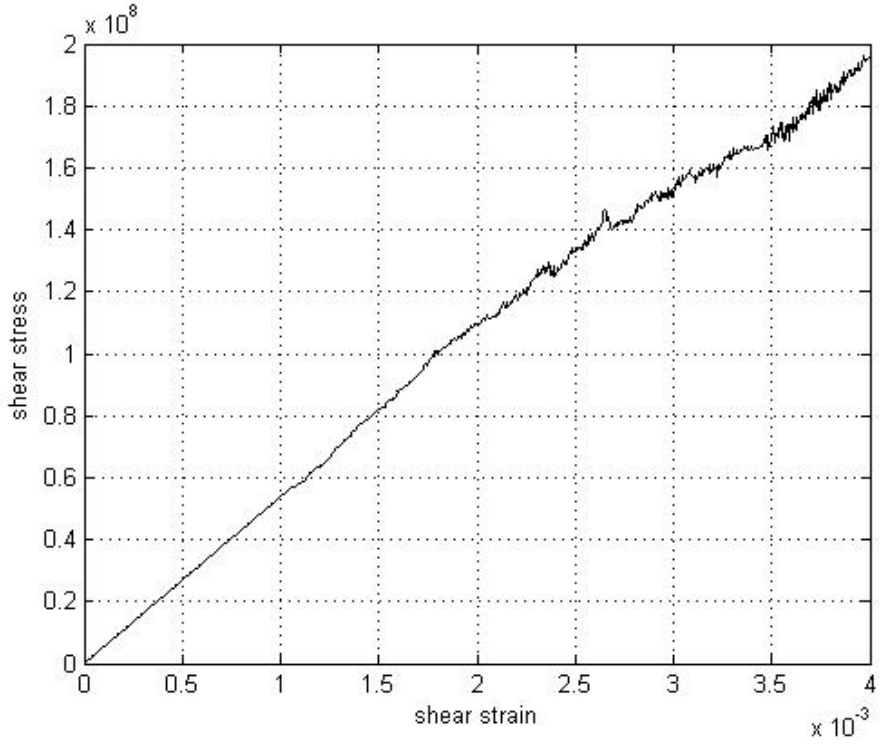

Figure 4.21 Strength curve for 0 .86×1μm model

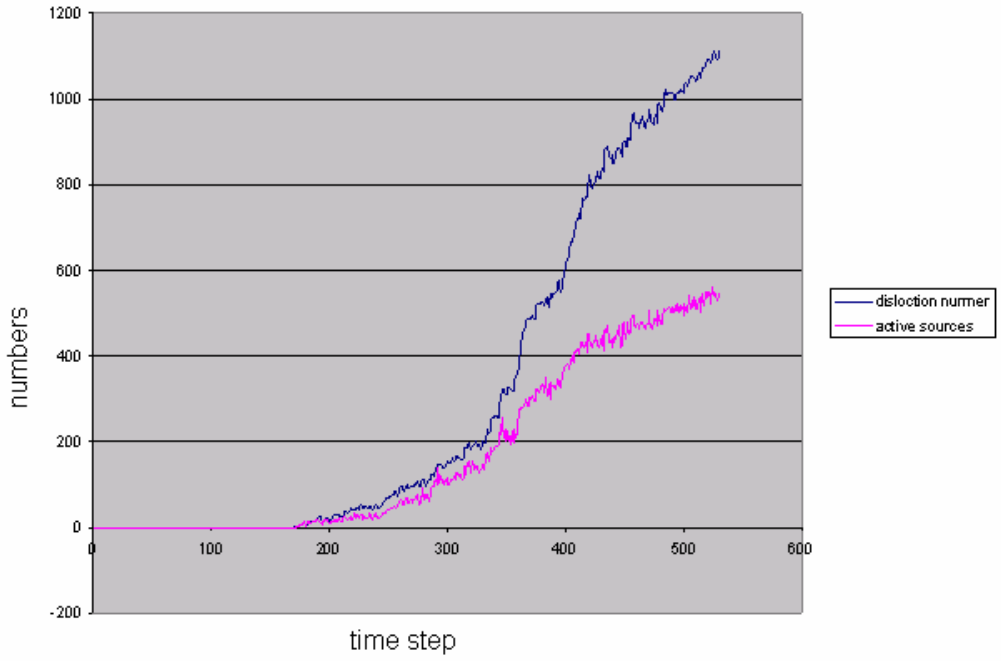

Figure 4.22 Dislocation number and active source number

To combine dislocation with sliding, the sliding effect is studied first without any dislocation to make sure that the sliding simulation works. The sliding only result is shown in Figure 4.23. The straight line stands for the elastic stress strain relationship; the lower curve is the sliding curve. After the model is totally relaxed by the sliding, the sliding curve turns into a straight line with a new slope. New equilibrium is formed in this stage. Figure 4.24 shows the convergence of the sliding model with the increasing number of boundary nodes.

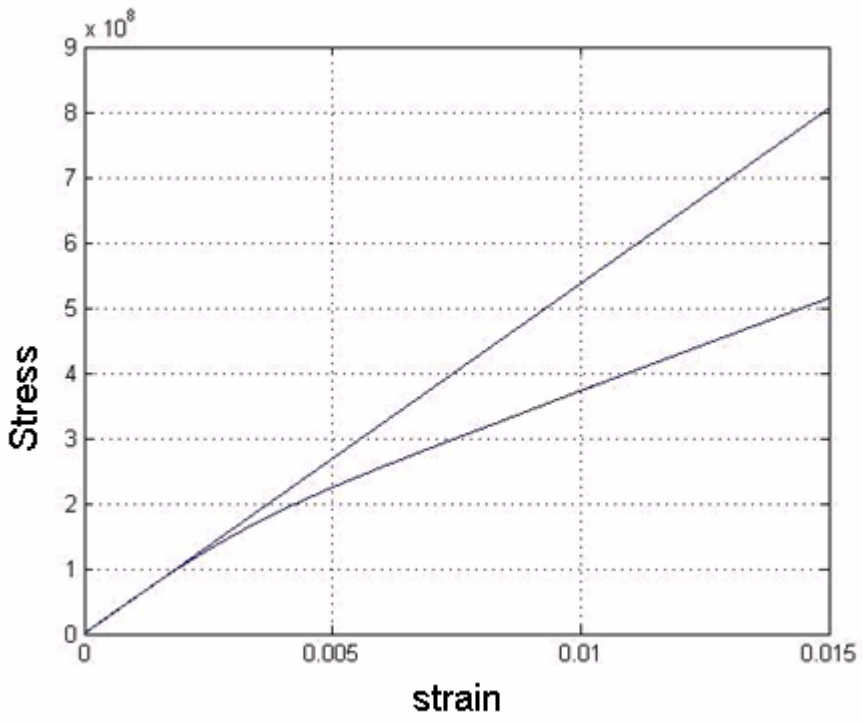

Figure 4.23 Sliding effect fro strain level up to 1.5%

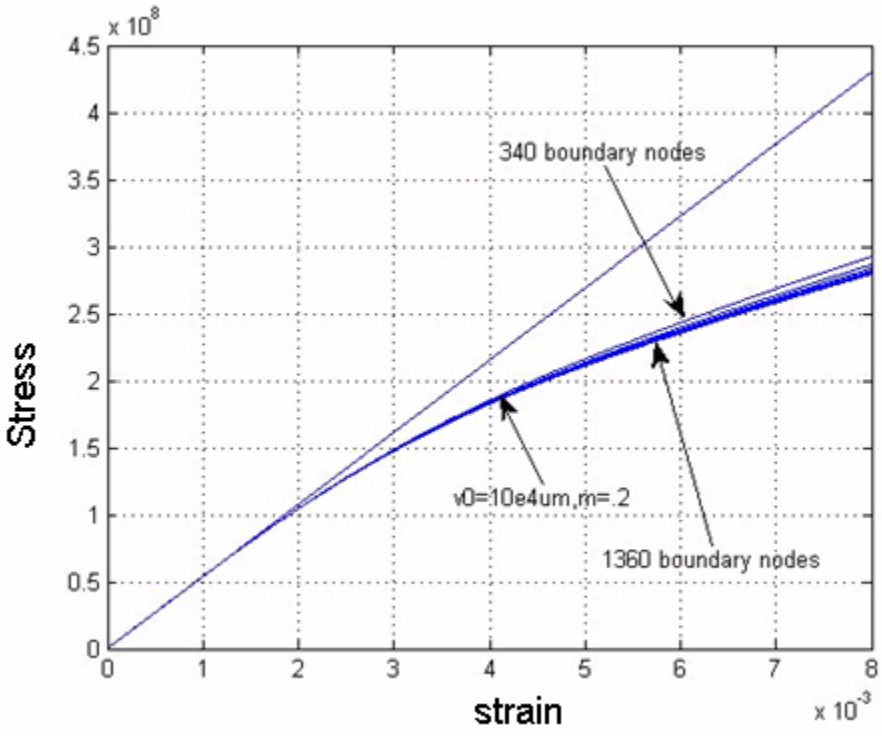

Figure 4.24 Sliding effect with different number of boundary nodes

To simulate the effect of sliding on the dislocation dynamics, different viscosities are chosen for the sliding simulation. The sliding parameter S_0 is set equal to shear modulus G, and m is set to 0.2. Those parameters are fixed for all sliding models. The combined sliding dislocation curves are shown in Figure 4.25 for 70nm grain size. The dislocation only curve is also shown as a reference. The special yielding point is where observable deviation appeared on the stress strain curves. The yielding point is lower when sliding is allowed and the drop depends on the sliding viscosity and also the grain size.

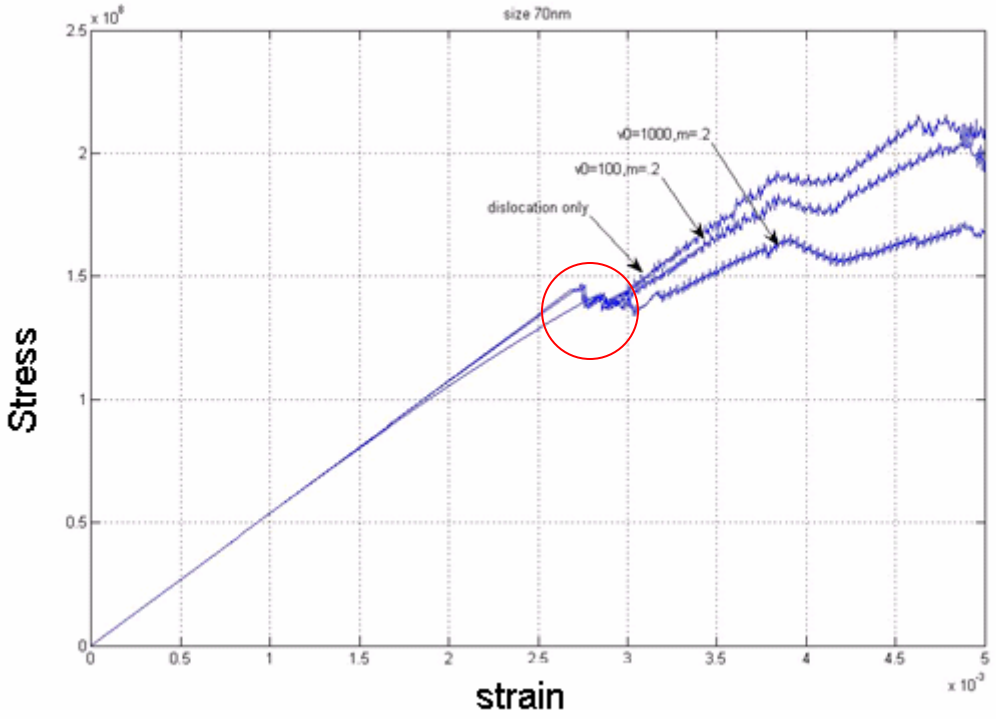

Figure 4.25 Dislocation and Sliding combined effects

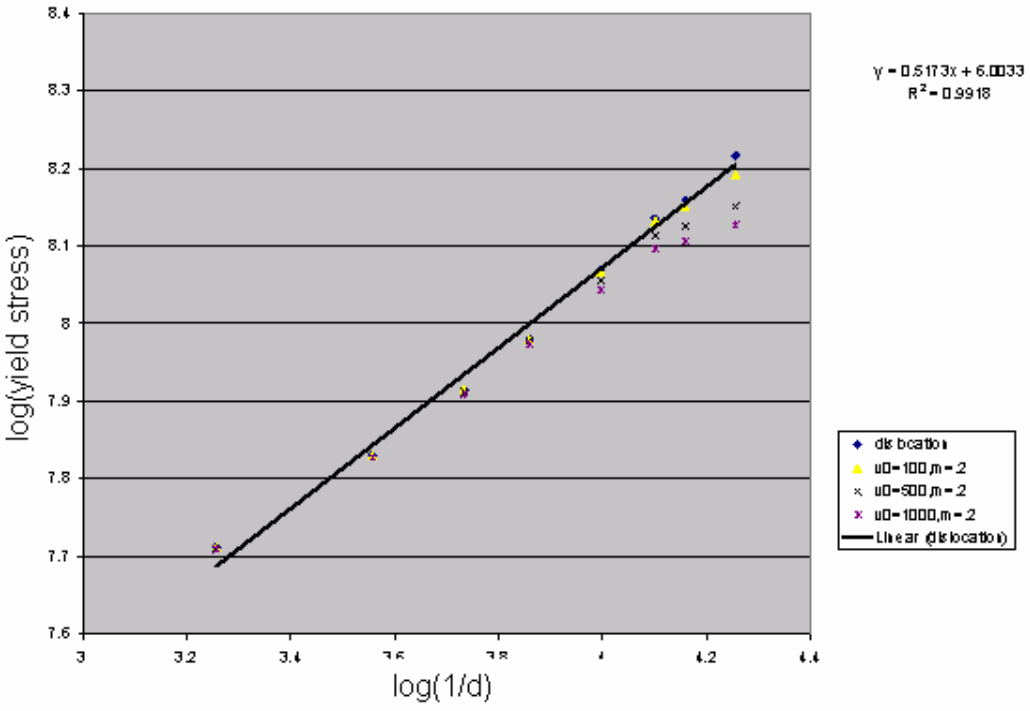

Figure 4.26 Grain size effects for sliding on yielding stress (log)

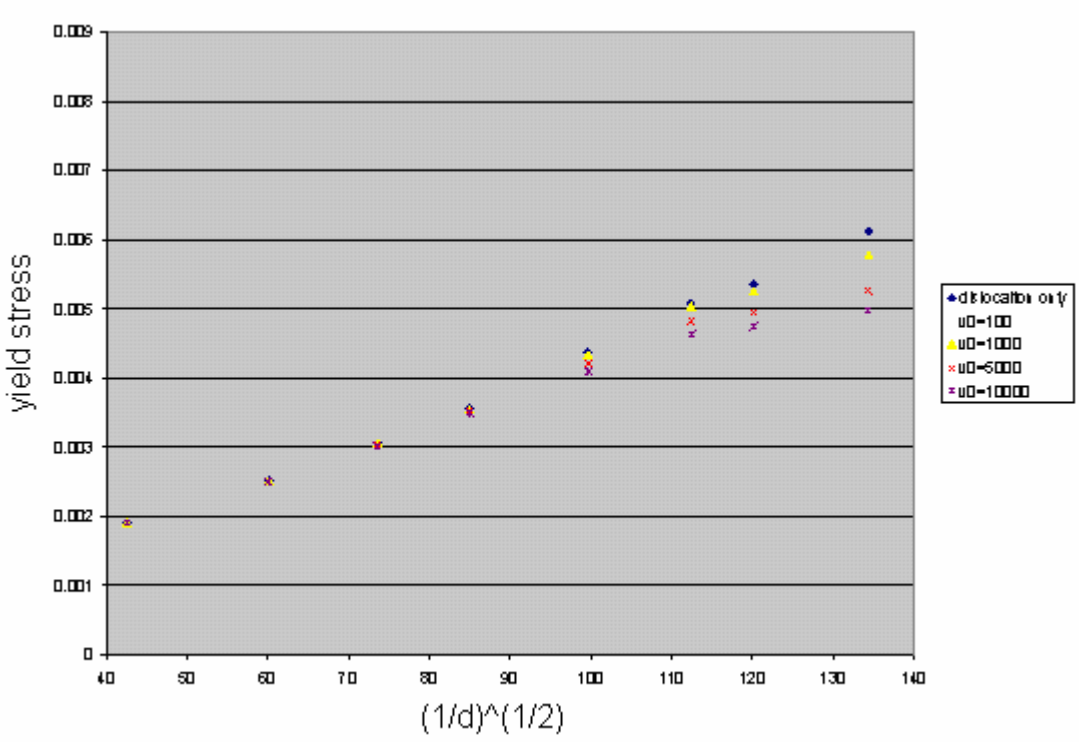

Figure 4.27 Grain size effect for sliding on yielding stress

The stress level for that yielding point has a specific relationship with the size of the grains. In isotropic dislocations, this relationship is the Hall-Petch Law[25, 26], which relates the yielding strength with the square root of the inverse grain size. In Figure 4.26 and 4.27, this variation is shown. From the log –log plot of Figure 4.26 we find the slope as 0.5173. This shows that the numerical solutions are consistent with the Hall-Petch Law.

The sliding effects are also shown in Figures 4.26 and 4.27. When the grain size is large, sliding has little influence on the yielding stress level. When the grain size is smaller, ((1/d)^1/2 >=100), sliding lowers the yielding level. The amount of drop in yielding stress depends on the value of sliding viscosity.

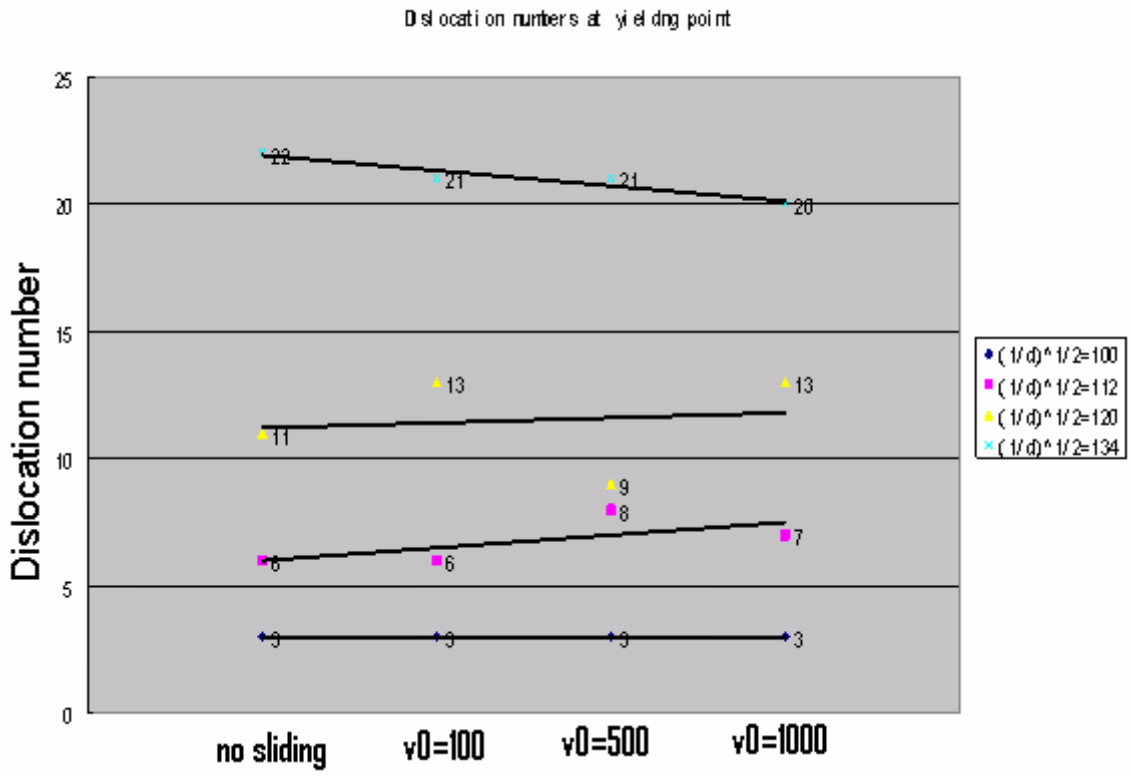

Figure 4.28 Dislocations numbers at yielding points

To study the reason for this drop in yielding stress, the dislocation numbers are recorded when yielding happened. Figure 4.28 shows the number of dislocations for different grain size and for different sliding parameter v0. Each line represents number of dislocations for a fixed grain size. The points on one single line shows the trend of number of dislocations for various sliding parameter, from no slide to v0=100, v0=500 and v0=1000.

When (1/d)^1/2 =100 or more sliding dragged down the dislocation strength. Figure 4.28 shows that at (1/d)^1/2 =100, the number of dislocations does not change with the sliding parameter. For other grain sizes, like (1/d)^1/2 = 112, 120 and 134, when sliding parameter changes, the number of dislocations do not any obvious trend. As

a conclusion, Figure 4.28 suggests that number of dislocations is not responsible for the change in yielding strength.

After ruling out the dislocation number as the cause for the drop in yielding strength, we can conclude that the sliding parameter is the root cause. At the same traction level, the bigger sliding parameter will introduce more displacements and more displacements will need less macro stresses to reach the same stress threshold at the source points to activate the dislocation yielding. The macro stress level is represented as the dislocation strength when yielding happens. As a summary, more sliding parameter v0 means more displacements and less macro stresses to activate yielding. When yielding happens, the reduced macro stress leads to the drop in yielding strength, as shown in Figure 4.27.

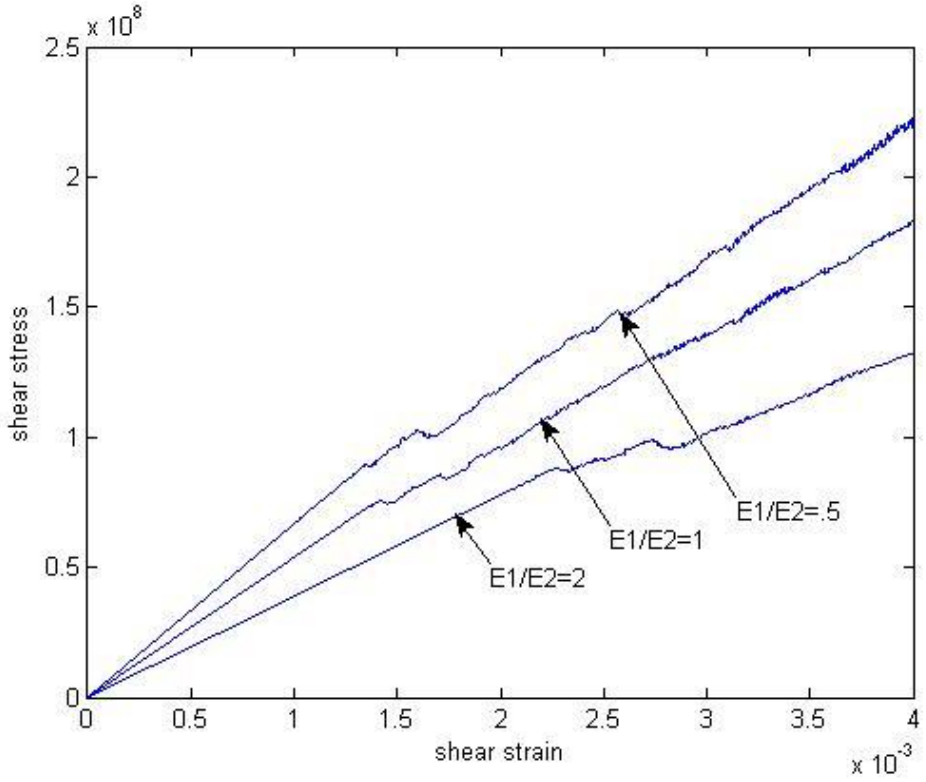

Figure 4.29 Anisotropy with dislocations

Next, the effect of anisotropy on dislocation dynamics is studied. For anisotropy, the ratio *E1/E2* is the controlling parameter. Figure 4.29 shows the effect of anisotropy on the stress strain curve. The variation of yield stress with grain size in the anisotropic case is shown is Figure 4.30 and 4.31.

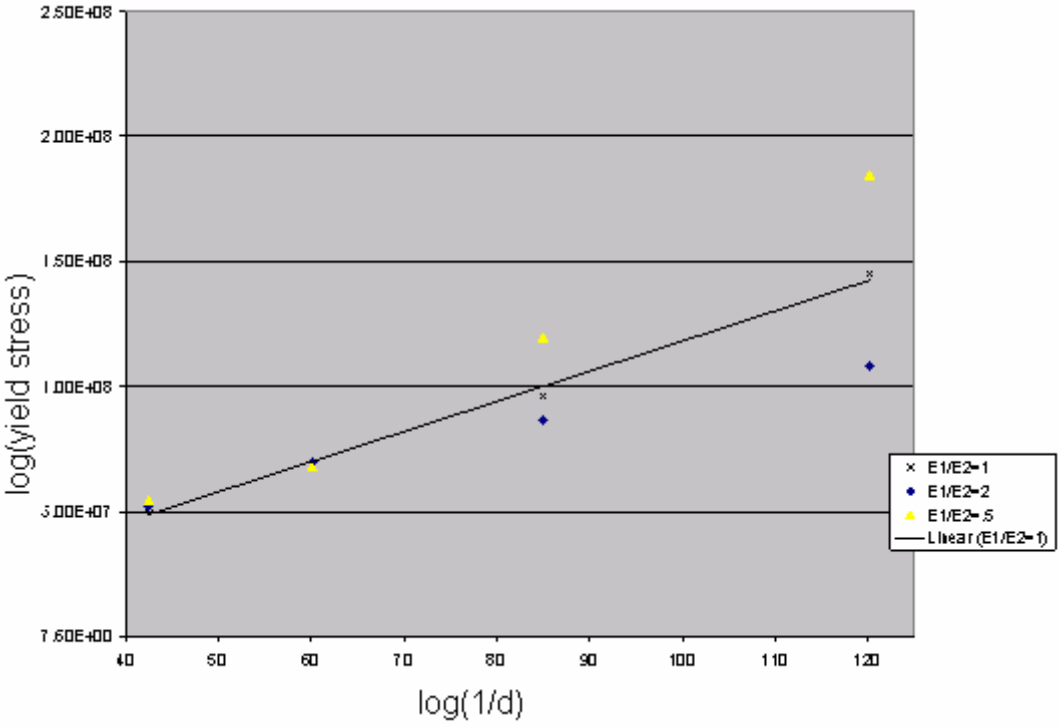

Figure 4.30 Grain size effect for anisotropy on yielding stress

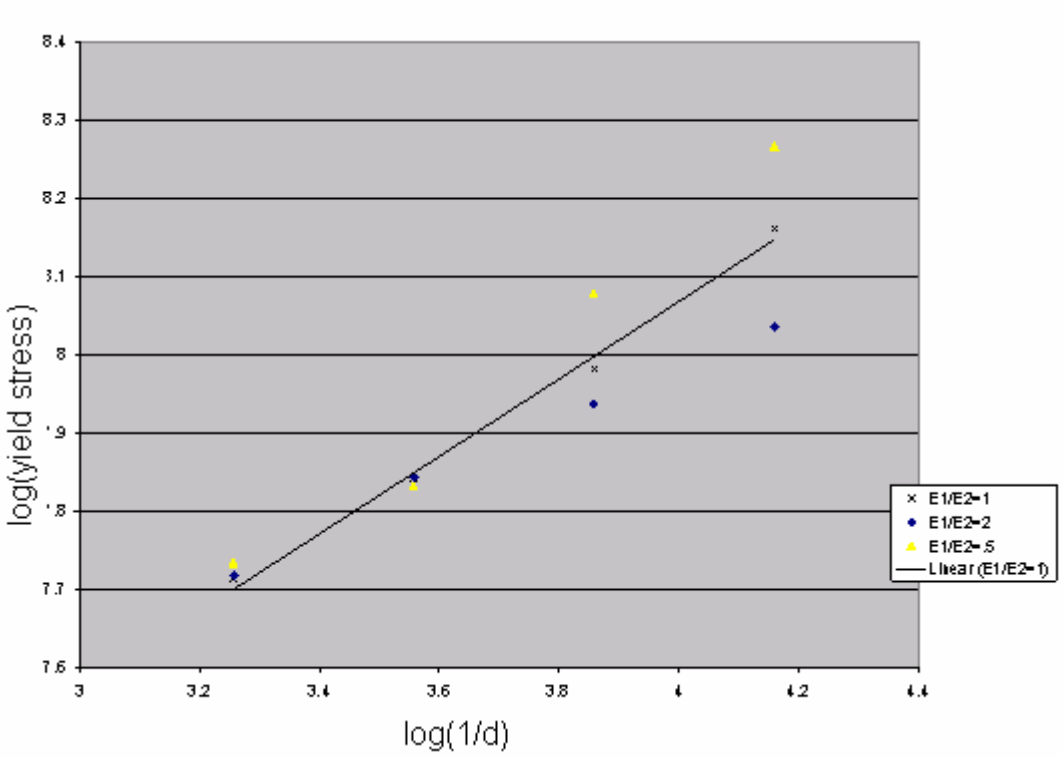

Figure 4.31 Grain size effect for anisotropy on yielding stress (log)

In the log-log plot of Figure 4.31, the isotropic curve has a slope of 0.5. This slope is larger than 0.5 when the anisotropy ratio is below one and the slope is less than 0.5 when the anisotropy ratio is above one.

References:

1. Amodeo, R.J. and N.M. Ghoniem, *Dislocation dynamics. I. A proposed methodology for deformation micromechanics.* Physical Review B, 1990. **41**(10): p. 6958-6967.
2. Amodeo, R.J. and N.M. Ghoniem, *Dislocation dynamics. II. Applications to the formation of persistent slip bands, planar arrays, and dislocation cells.* Physical Review B, 1990. **41**(10): p. 6968-6976.

3. Kubin, L.P., et al., *Dislocation microstructures and plastic flow: a 3D simulation.* Solid State Phenomena, 1992. **23**(24): p. 455–472.

4. Van der Giessen, E. and A. Needleman, *Discrete dislocation plasticity: a simple planar model.* Model. Simul. Mater. Sci. Eng, 1995. **3**: p. 689–735.

5. Schwarz, K.W., *Simulation of dislocations on the mesoscopic scale. I. Methods and examples.* Journal of Applied Physics, 1999. **85**(1): p. 108.

6. Zbib, H.M., M. Rhee, and J.P. Hirth, *On plastic deformation and the dynamics of 3D dislocations.* International Journal of Mechanical Sciences, 1998. **40**(2): p. 113-127.

7. Huang, H. and G.A. Kardomateus, *Dislocation-based boundary-element method for crack problems in anisotropic half-planes.* AIAA Journal, 2004. **42**(3): p. 650-657.

8. Acharya, A., *A model of crystal plasticity based on the theory of continuously distributed dislocations.* Journal of the Mechanics and Physics of Solids, 2001. **49**(4): p. 761-784.

9. Acharya, A., *Driving forces and boundary conditions in continuum dislocation mechanics.* Proceedings: Mathematical, Physical and Engineering Sciences, 2003. **459**(2034): p. 1343-1363.

10. Acharya, A., *Constitutive analysis of finite deformation field dislocation mechanics.* Journal of the Mechanics and Physics of Solids, 2004. **52**(2): p. 301-316.

11. Acharya, A. and A. Roy, *Size effects and idealized dislocation microstructure at small scales: Predictions of a Phenomenological model of Mesoscopic Field*

Dislocation Mechanics: Part I. Journal of the Mechanics and Physics of Solids, 2006. **54**(8): p. 1687-1710.

12. Roy, A. and A. Acharya, *Finite element approximation of field dislocation mechanics.* Journal of the Mechanics and Physics of Solids, 2005. **53**(1): p. 143-170.
13. Roy, A. and A. Acharya, *Size effects and idealized dislocation microstructure at small scales: Predictions of a Phenomenological model of Mesoscopic Field Dislocation Mechanics: Part II.* Journal of the Mechanics and Physics of Solids, 2006. **54**(8): p. 1711-1743.
14. Gao, X.W., *The radial integration method for evaluation of domain integrals with boundary-only discretization.* Engineering Analysis with Boundary Elements, 2002. **26**(10): p. 905-916.
15. Gao, X.W., *A Boundary Element Method Without Internal Cells for Two-Dimensional and Three-Dimensional Elastoplastic Problems.* Journal of Applied Mechanics, 2002. **69**: p. 154.
16. Gao, X.W., *Evaluation of regular and singular domain integrals with boundary-only discretization—theory and Fortran code.* Journal of Computational and Applied Mathematics, 2005. **175**(2): p. 265-290.
17. Gao, X.W. and T.G. Davies, *An effective boundary element algorithm for 2D and 3D elastoplastic problems.* International Journal of Solids and Structures, 2000. **37**(36): p. 4987-5008.
18. Eshelby, J.D., *Boundary Problems\ for Dislocations*, in *Dislocations in Solids*. 1979. p. 167-221.

19. Hirth, J.P. and J. Lothe, *Theory of Dislocations*. 1982. 857.

20. Hull, D. and D.J. Bacon, *Introduction to Dislocations. International Series on Materials Science and Technology, Vol. 37*. 1965, Oxford: Pergamon Press.

21. Jr, W.J.W., *Elementary Dislocation Theory*. 1964: The Macmillan Co., London, England.

22. Mura, T., *Continuous distribution of moving dislocations.* Phil. Mag, 1963. **8**: p. 843-857.

23. Mura, T., *Micromechanics of Defects in Solids*. 1987: Springer.

24. Nabarro, F.R.N., *Theory of Crystal Dislocations*. 1967: Clarendon Press.

25. Hall, E.O., *The Deformation and Ageing of Mild Steel: III Discussion of Results.* Proceedings of the Physical Society Section B, 1951. **64**(9): p. 747-753.

26. Petch, N.J., *The cleavage strength of polycrystals.* Iron and Steel Institution of London Journal, 1953. **174**: p. 25–28.